THE NORDIC CONCRETE FEDERATION 1/2015 PUBLICATION NO. 52

Nordic Concrete Research

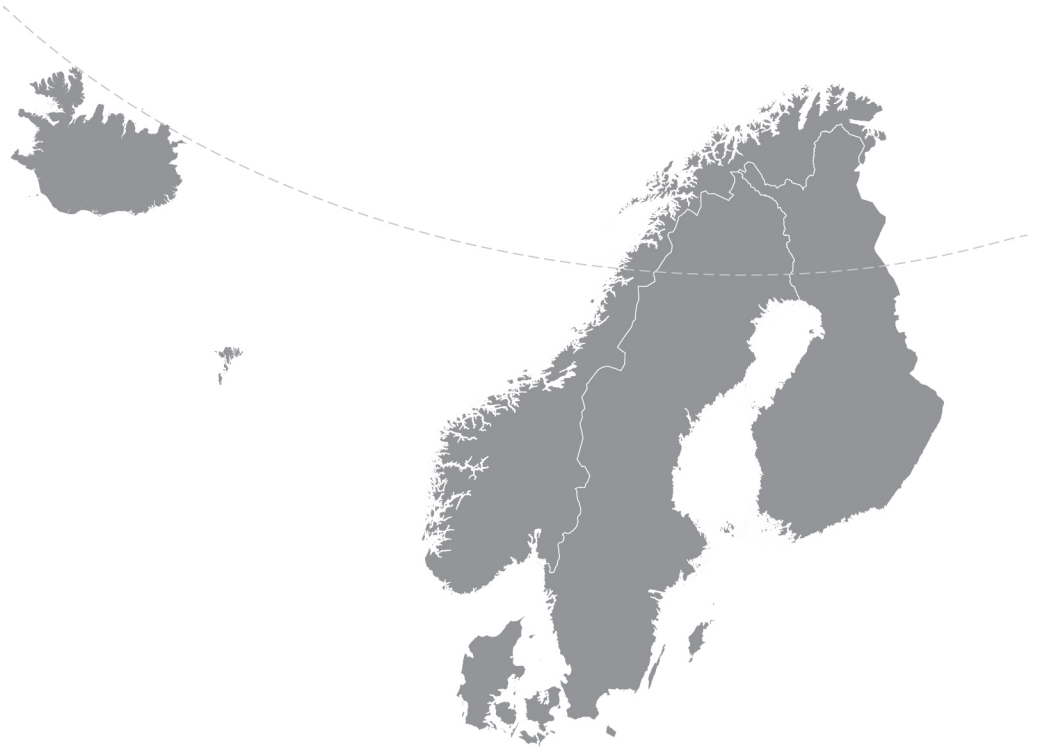

Nordic Concrete Federation

PUBLICATION NO. 52 1/2015

NORDIC CONCRETE RESEARCH

EDITED BY
THE NORDIC CONCRETE FEDERATION

CONCRETE ASSOCIATIONS OF: DENMARK
FINLAND
ICELAND
NORWAY
SWEDEN

PUBLISHER: NORSK BETONGFORENING
POSTBOKS 2312, SOLLI
N - 0201 OSLO
NORWAY

VODSKOV, JUNE 2015

Preface

Nordic Concrete Research is since 1982 the leading scientific journal concerning concrete research in the five Nordic countries, e.g., Denmark, Finland, Iceland, Norway and Sweden. The content of Nordic Concrete Research reflects the major trends in the concrete research.

Nordic Concrete Research is published by the Nordic Concrete Federation which also organizes the Nordic Concrete Research Symposia that have constituted a continuous series since 1953 in Stockholm. The XXII Symposium was held i August 2014 in Reykjavik. Most of the papers in this volume of NCR is full papers, where only 4 pages extended abstracts were presented in Reykjavik.

The next symposium, no. XXIII, will be held Aalborg, Denmark 21. - 23. of August 2017. We do look forward to welcome you there.

Since 1982, 428 papers have been published in the journal. Since 1994 the abstracts and from 1998 both the abstracts and the full papers can be found on the Nordic Concrete Federation's homepage: www.nordicconcrete.net. The journal thus contributes to dissemination of Nordic concrete research, both within the Nordic countries and internationally. The abstracts and papers can be downloaded for free. Proceedings from miniseminars and the proceedings from the Research Symposia are about to be published on the homepage as well.

The high quality of the papers in NCR are ensured by the group of reviewers presented on the last page. All papers are reviewed by three of these, chosen according to their expert knowledge.

Since 1975, 77 Nordic Miniseminars have been held – it is the experience of the Research Council of the Nordic Concrete Federation, that these Miniseminars have a marked influence on concrete research in the Nordic countries. In some cases, the information gathered during such Miniseminars has been used as Nordic input to CEN activities.

The latest Miniseminar " Residual capacity of deteriorated concrete structures" was held in Oslo, 21st of April.

Vodskov, June 2015

Dirch H. Bager
Editor, Nordic Concrete Research
Chairman, Research Council of the Nordic Concrete Federation

PUBLICATION NO. 52 1/2015

CONTENTS

1	Raul Fuentes, Mette Geiker & Henrik Stang **Characterisation of fibre content, distribution and orientation to predict Fibre Reinforced Concrete behaviour**	1
2	Abhay Bulsari, Klaus Juvas & Olli Skyttä **Optimising carbon dioxide emissions from concrete with two cements using nonlinear modelling**	23
3	Ali Mohammadi Mohaghegh, Johan Silfwerbrand & Vemund Årskog **Properties of Fresh Macro Basalt Fibre (MiniBar) Self-Compacting Concrete (SCC) and Conventional Slump Concrete (CSC) Aimed for Marine Applications**	43
4	Helén Jansson & Luping Tang **Parameters Influencing the Initial Setting Time of Alkali-Activated Ground Granulated Blastfurnace Slag Materials**	63
5	Shuping Wang, Xiaoqin Peng, Mei Li & Luping Tang **Pb^{2+} Adsorption by Calcium Silicate Hydrate Synthesized from Steel Slag**	77
	Research Council and Editorial Board of NCR	93
	Review Group for NCR	95

Characterisation of fibre content, distribution and orientation to predict Fibre Reinforced Concrete behaviour

Raul Fuentes
Lecturer
School of Civil Engineering
University of Leeds
LS2 9JT
Tel: (+44) 0113 343 2282
Email: r.fuentes@leeds.ac.uk

Mette Geiker
Professor
Department of Structural Engineering, Faculty of Engineering Science and Technology, Norwegian University of Science and Technology (NTNU),
NO-7491 Trondheim, Norway (formerly DTU).
Email: mette.geiker@ntnu.no

Henrik Stang
Professor
Department of Civil Engineering, Technical University of Denmark (BYG-DTU),
Brovej Building 118, DK-2800 Kgs. Lyngby, Denmark.
Email: hs@byg.dtu.dk

Keywords: Image Analysis, Fibres, Orientation, CT-scanning, Distribution, Mechanical properties

ABSTRACT

This paper calculates the flexural behaviour (load-displacement and stress-crack opening distributions) of "real" beams where the contribution of every single fibre is considered. It therefore, allows clarifying to what extent a link between single fibre pull-out models and post-cracking behaviour can be established when the uncertainty about the actual fibre content, distribution and orientation is eliminated by using a computed tomography (CT) - imagery algorithm. The results were compared to three point bending tests of the same beams. The CT algorithm also presents a solution to the difficult problem of separating clusters that occur when fibres pack together within the concrete matrix.

1. INTRODUCTION

It is well established that the content, distribution and orientation of fibres has a significant impact on the mechanical properties of Fibre Reinforced Concrete (FRC) [1-33]. This has prompted many researchers to develop non-destructive techniques such as electrical [34-39], ultrasounds [40], magnetic approaches [41-44], x-rays and CT scanning [4-5,8,12,45-51] and other numerical and analytical approaches [52-60] for its characterisation. A good initial reading on all the different techniques is provided in [61-63]. Most of them are however based on averaging methods and partial observations of the fibres. Only CT scanning is yet, in principle, capable of observing all individual fibres. However, none of the techniques presented has been capable of solving completely the problem of full reconstruction and characterisation of the fibres within the concrete matrix. The main reason is the FRC fibres' ability to form bundles or clusters, which makes their separation and tracking very challenging [64,65], even for image analysis specialists [66] and hence, tend to be ignored. This paper presents a novel and simple solution to this challenge.

Additionally, the link between fibre orientation and mechanical properties – in particular the fracture properties in tension – has been intensively studied by many researchers in the past in a variety of different FRC-materials. This has resulted in models for the post-crack behaviour based on single fibre pull-out behaviour – direct and inclined – and information about the fibre orientation, typically in the form of a fibre orientation distribution function in analytical or semi-analytical approaches, e.g. [10-12]. Alternatively others used information about the position and orientation of each fibre using numerical approaches e.g. [13,21,31,58,60]. However, it is presently unclear to what extent models for single fibre pull-out can adequately form the basis for predictions of the (average) post-cracking behaviour observed in FRC materials. This is partly due to the variation in fibre content, distribution and orientation observed in real test specimens making it difficult to distinguish between model uncertainty and inherent material variation. For example, authors have shown that for similar beams, the peak loads vary between 20% [33] and 30% [16] and both authors have attributed this to fibre distribution and orientation variability.

The aim of this study is to clarify to what extent removing the uncertainty about the actual fibre content and orientation helps in establishing a clearer link between single fibre pull-out models and post-cracking behaviour.

Thus, this paper presents two distinct novel contributions:
(1) a simple algorithm to use CT imagery to reconstruct complete information about the distribution of fibres in FRC in the crack plane in a set of test beams that solves the problem of clustering
(2) the first application of the calculation of the average post-cracking behaviour of fibre reinforced concrete beams in bending using that uses the actual information of every single fibre within it.

The validation of the results was carried out by comparing the results with those obtained from three point bending tests undertaken in the lab on the same beams. The data used in the present study was established by the first author and is described in [45].

2. CONCRETE SAMPLES AND CHARACTERISATION

The concrete properties were characterized with two types of test specimens: beams for three point bending and 100mm diameter and 200mm long cylinders for compressive testing. Beams with three different heights were cast: 40mm (*Shallow)*, 60mm (*Medium*) and 150mm (*Standard*). All beams had a width of 150 mm and length of 600 mm. The term *Standard* refers to the dimensions given in RILEM [66].

The casting of the beams was carried out in two batches: Two *Standard*, three *Shallow* beams and five concrete cylinders were cast from Batch 1, and two *Standard*, three *Medium* beams and five concrete cylinders were cast from Batch 2. Casting was undertaken following the directions in RILEM [66]. The individual beams are referred to by $Standard_{ij}$, where 'i' represents the number of the batch in which they were cast, and 'j' the number within each batch. *Shallow and Medium* beams are referred to using only one number (e.g. *Medium* 1). A 1% volume content of steel hooked-end fibres was used. The design water-cement ratio, density and air content were respectively 0.447, 2.350kg/m³ and 4.6% for both batches. Table 1 shows the material densities and the concrete design mix.

Table 1.Concrete materials and mix recipe

Material	Density (kg/m³)	Mix quantities (kg/m^3)
Rapid cement	3160	245
Fly ash	2300	94.5
Microsilica	2290	10.5
Water	1000	140
Air entraining agent.	1001	0.4
Plasticizer	1010	4.2
0-4 (mm) Sand	2618	743.9
4-8 (mm) Stone	2642	452.9
8-16 (mm) Stone	2637	570.3
Steel fibres	7500	78

Average compressive strengths of 52.3 ± 0.67 MPa (mean ± standard deviation) for Batch 1 and 57.3 ± 0.83 MPa for Batch 2 were found from the cylinders. The tensile strength, f_t, and the Young's modulus, E_c, of the concrete were calculated using the recommendations of Neville [67] and the ACI Building Code [68] respectively as shown below:

$$f_t = 0.3(f_c)^{2/3} \quad (1)$$

$$E_c = 4734\sqrt{f_c} \quad (2)$$

where f_c is the compressive strength as measured from the cylinders. The average compressive strength of both batches was used for the calculations. Calculated values were 4.3MPa and 35GPa for the tensile strength, f_t, and the Young's modulus, E_c, respectively.

3. THREE POINT BENDING TESTS (TPBT)

The Three Point Bending Tests (TPBT) were conducted according to the RILEM recommendations [67] as was current in 2001 when the tests were carried out. The current standard is BS EN 14651:2005+A1:2007.

Accordingly, notches were sawed at mid span of each beam. The recommendation establishes that notches must be cut to a depth of 1/6 of the total beam height at the bottom of the beam. However, for the *Shallow* beams a ratio of 1/4 was used (i.e. 10mm notch) to facilitate obtaining cracking at the centre span.

A clip gauge was installed to measure the crack mouth opening displacement (CMOD). It had a gauge length of 10 mm and a travelling distance of 4 mm and it was mounted at the underside of the beam clipped to two steel blocks with an initial opening equal to the gauge length (i.e.10 mm).The two additional vertical rod gauges allowed measuring the vertical displacement in two different points symmetrically placed at either side of the wedge through which the load (P) was applied. They were mounted on a frame that was purposely designed in the lab for tests on similar beams to arrest any rotational effects.

An INSTRON closed loop machine was utilized to undertake the tests under deformation control conditions. Two channels controlled the test performance; the clip gauge (CMOD) and the vertical gauges (vertical displacement). The test was divided in two phases: The first phase was controlled by the clip gauge until its maximum travelling was reached, and the second phase was controlled by the mid-span deformation. The linear relationship between the CMOD and the vertical displacement (shown as Extension), shortly after the peak load (P_{peak}) had been reached, was obtained for each beam; all beams showed this linear relationship as also observed by other authors [21,69]. A summary of the results from the TPBT can be seen in Table 2.

Table 2. Summary results.

Beam	Peak load (kN)	CMOD (mm) at peak load	Fibres bridging the crack	Fibres / mm^2 in the section	Fibres volume (%)	NNA	QA
	TPBT results		CT Scanning analysis results			Fibre distribution	
*Standard*11	15.73	0.060	1017	0.045	0.961	0.965	1.216
*Standard*12	27.63	0.037	1137	0.050	0.958	1.047	1.078
*Shallow*1	1.53	0.027	754	0.125	2.536	1.057	1.298
*Shallow*2	1.47	0.059	298	0.049	1,345	1.058	1.192
*Standard*21	29.14	0.062	949	0.042	1.033	0.973	1.369
*Standard*22	38.40	0.066	889	0.039	1.095	0.984	1.357
*Medium*2	5.19	0.057	762	0.085	2.084	1.343	0.923
*Medium*3	5.28	0.045	345	0.038	1.070	1.304	0.520

4. CT SCANNING

A Siemens Somotom Plus CT Scanner, shown in Figure 1a, at the Department of Chemical and Biochemical Engineering at DTU was used for the image acquisition. The scanner uses Computed Tomography which is based on the x-ray principle (see Figure 1b). When x-rays emitted from source pass through the beam, they are absorbed or attenuated creating a profile of x-ray beams of different strength that are captured by the detector at the other end. When both the x-ray source and the detector have completed a full lap rotation (360^0), a two dimensional image is obtained. The image is the two dimensional projection of a thin slice over which the scanner has made the detection. This slice can have typically thicknesses between 1 mm and 10 mm depending on the applications.

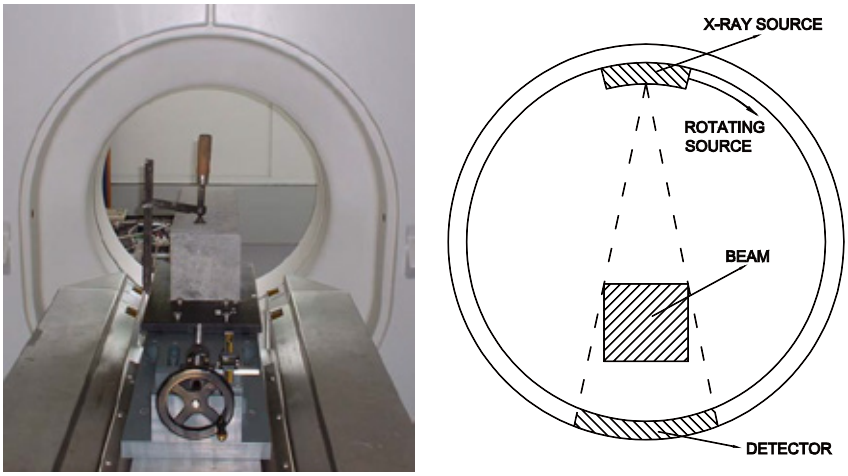

Figure 1. Somoton CT Scanner. (a) Photograph (b) Working principles diagram

The scans were taken over a length of 100 mm in each of the beams, 50 mm at either side of the mid span of the beams, where the notch was cut. This distance was enough to include all fibres that bridged the mid-span section (the fibres were 36 mm long). 2 mm thick scan slices were used, as 1 mm was proven unacceptable due to the high levels of noise observed in trial scans; the same observation was highlighted by Hunt et al [70]. The images obtained were 512x512 pixels, for all the beam sizes.

The CT Scanner parameters used were: a tube potential of 137 kV, tube current of 510 mAs for the *Standard* and *Medium* size beams and 120kV and 330 mAs for the *Shallow* size beams.

5. IMAGE ANALYSIS – RECONSTRUCTION OF FIBRES WITHIN THE CONCRETE BEAMS

Image processing

Each image represents a 2mm slice of the object. As mentioned above, the steel fibres absorb much of the x-rays and therefore show as white, and brighter, spots; these are called elements hereafter. In order to be able to isolate the steel fibres from the rest of the features in the images, the following image processing steps were followed (see Figure 2):

- Apply a high threshold (250 for Batch 1 and 230 for Batch 2 – the different thresholds were selected by inspection ??) to the original image (Figure 2a) and convert it to binary (i.e. all pixels above the threshold are plotted in white and all those below are plotted in black) – Figure 2b.
- The high threshold image was eroded in order to eliminate noise – Figure 2c.
- A low threshold (220 for Batch 1 and 200 for Batch 2) was applied to the original image and convert to binary – Figure 2d.
- The eroded image was used to identify the position of fibres within the matrix, which were then reconstructed using the shapes of the low threshold image. – Figure 2e.

The image analysis was conducted using the functions of the Image Analysis library of the computer program MATLAB.

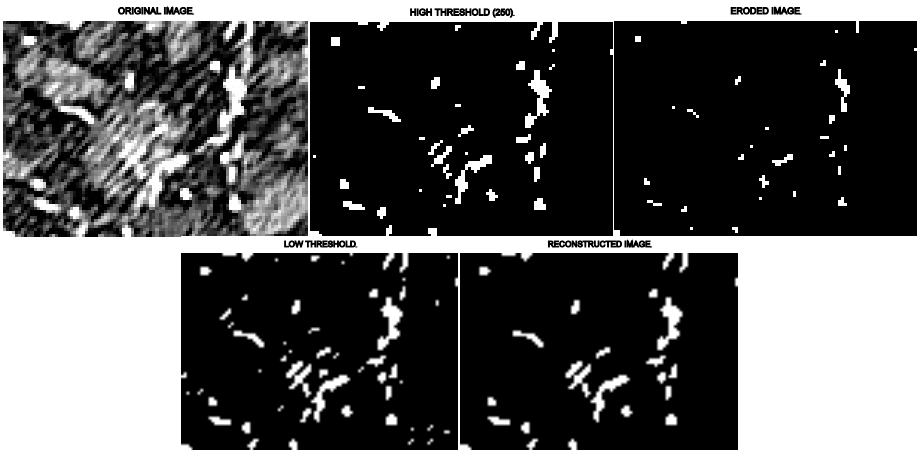

Figure 2. Image processing. Left-to-right from the top: (a) Original image (b) High threshold image (c) Eroded image (d) Low threshold image (e) Reconstructed image

Reconstruction and clusters rationalisation

The tracking of fibres within the scanned domain was based on the principle shown in Figure 3: if a single fibre crosses two consecutive slices, its projection of two superimposed consecutive slices will have pixels in common. Another assumption was that a fibre projects with the same area in all different slices (see Figure 3).

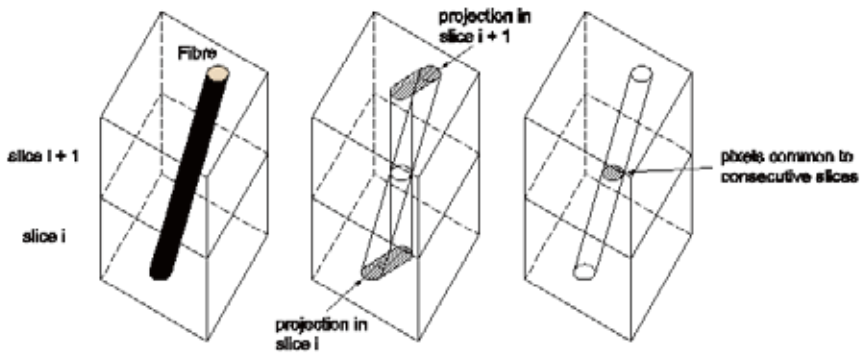

Figure 3. Common pixels principle between slices.

Due to the volumetric nature of the slices (i.e. they have a thickness), two different fibres could project in the same slice within the same pixels. This could lead to clusters of fibres in each single slice which could potentially introduce erroneous common pixels and tracking paths. This is what we have referred here to as clusters of bundles.

Examples of clustering can be appreciated in Figure 2a, which show as irregular shapes of elements, and are the result of the projection of different fibres superimposing. In order to rationalise these from the fibres' selection, the clusters were eliminated from potential fibres using the area as elimination criteria, and recovered once a full fibre had been found. For simplification purposes, clusters were defined as those elements whose area was equal or higher than the average area of the elements in the list plus a standard deviation. The above process is exemplified in Figure 4.

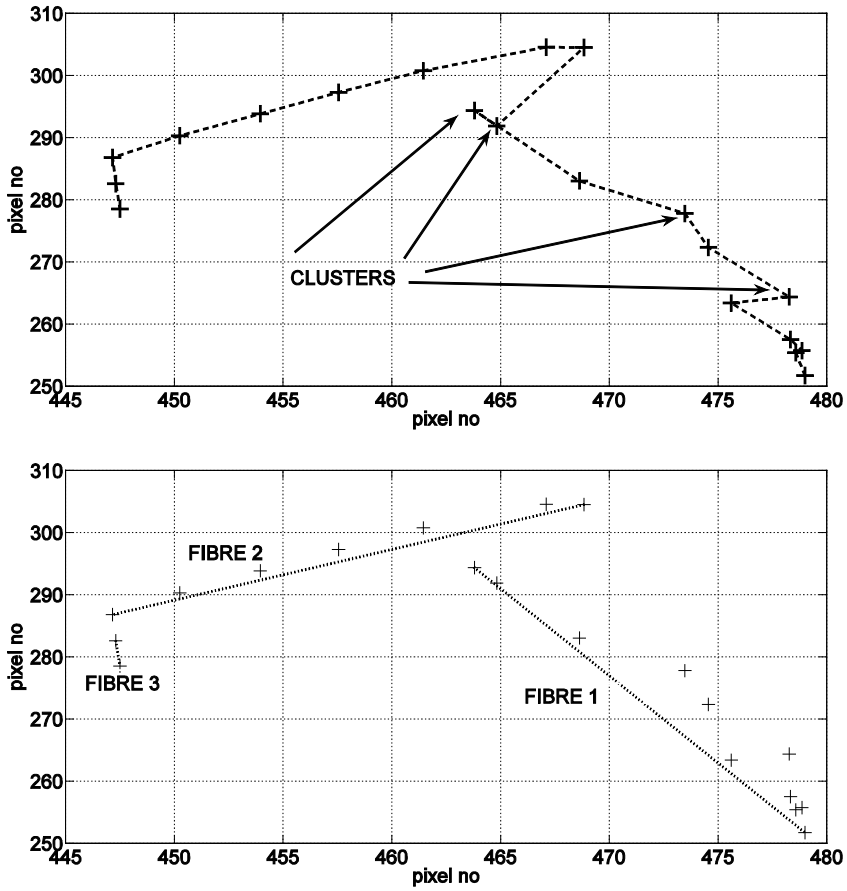

Figure 4. Example of fibre selection (a) Centre of mass of elements (b) Result of fibre selection after filtering

Figure 4a shows the centre of gravity of multiple elements from consecutives slices and superimposed in the image plane. Figure 4b shows the selected fibres and how this selection was successful in ignoring the potential deviations that clusters included in the tracking. Two observations are noted: (1) the distance between elements within a fibre in the image plane is approximately equidistant and (2) the elements within a selected fibre are aligned (i.e. the fibre projection is a straight line) as it was expected. In future work, these characteristics will also be used for the tracking algorithms.

A fibre was selected when the tracked sequence of elements provided a length between 27 to 36mm (the former length is the straight part of the fibres excluding the hook ends, and the latter is the total length including the hooks – see Figure 5a).

Once a fibre had been selected, the following characteristics were recorded (see Figure 5b): (1) Φ: the angle that the fibre forms with the normal to the cross section of the beam (2) θ: the angle that the fibre forms with a horizontal plane that is also perpendicular to the cross section of the

beam. (3) Position within the volume given by the coordinates of the starting and ending point. (4) Length.

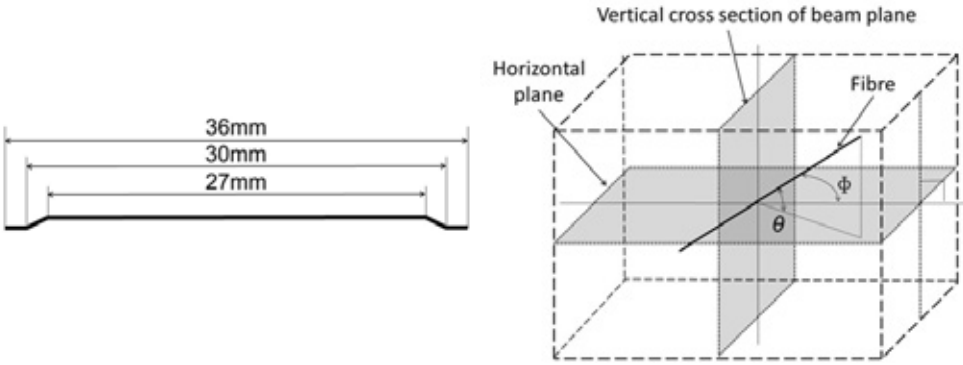

Figure 5. (a) Hook-end fibres geometry. (b) Fibre orientation angles

The first two provide the orientation of the fibres, the third was indicative of whether a fibre was bridging the centrally induced crack or not, and the fourth allows calculating the embedment of the fibre at either side of the cracked section.

Results and discussion of fibre reconstruction

Table 2 shows the numbers of calculated fibres that bridge the crack section and volume percentage of fibres for each beam. The latter is particularly interesting to note as, with the exception of *Shallow* 1 and *Medium* 2, they all show values close to the 1% volume of the mix. This provides increased confidence in the reconstruction process.

Further verification of the results can be carried out by comparing the calculated number of crack bridging fibres to theoretical and observed values in the literature. Lofgren [69] showed that the number of bridging fibres in a beam responds to Equation 3:

$$N_B = \frac{V_f}{A_f}\eta_B \tag{3}$$

where V_f and A_f represent the volume and cross sectional area of fibres respectively, and η_B is a number that varies with the spatial distribution of the fibres, and that some authors call the orientation factor. Lofgren [69] shows that this value equals 0.5 for a completely random 3D distribution. Equation 3 hence shows that the theoretical number of bridging fibres for a random distribution is 572, 229 and 153 for the *Standard*, *Medium* and *Shallow* beams respectively. Dupont & Vandewalle [53] calculated 516 fibres for *Standard* beams with similar mixes and the same beam and fibre geometry using their own method. These values do not compare positively with those calculated and shown in Table 2. However, the Lofgren method assumes that there is the same probability in a 3D random distribution for fibres to be placed at any angle to the normal of the cracked section [69]. Figure 6 shows that the probability density functions (*pdf*) of the angle Φ for all beams follow a normal distribution, which average normal distribution has a mean of 47.55 and standard deviation 18.17. This average value is similar to the results presented by Robins et al of 36.9 and 18.20 for a similar mix [47]. Similar normal distributions have been also presented by Abrishambaf et al for very similar concrete mix, fibre geometry and casting conditions [8] and Laranjeira et al [54].

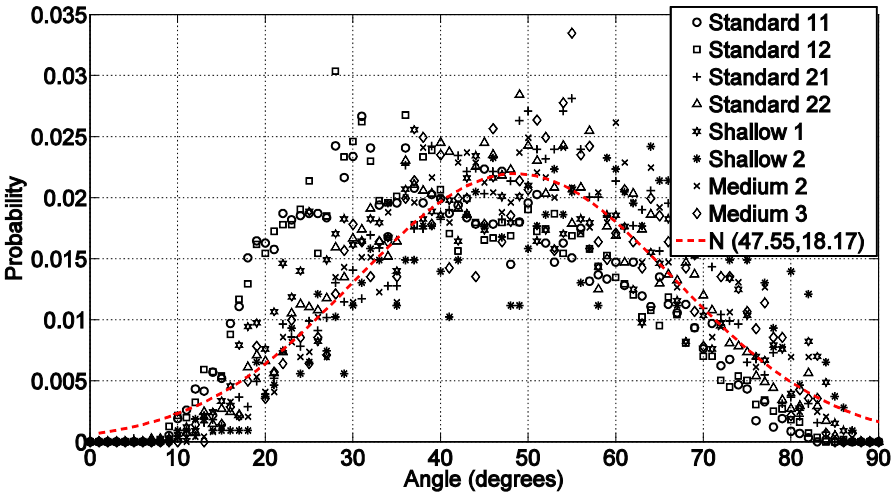

Figure 6. Probability Density Functions of angle Φ.

The figure also shows that the number of fibres that form a 90 degree angle is insignificant and therefore, suggests that all the fibres present in a beam cross section would be crossing a crack that developed in that section; this corresponds to a 1D, rather than 3D, random distribution (i.e. no fibres were found to be parallel to the beam cross sections) using Löfgren nomenclature. This is also supported by the numerical model created by Kang & Kim [17]. Hence, using Equation 3 and a value of η_B equal to 1, as indicated by Lofgren [69], the number of fibres results in values of 1142, 458 and 306 for the *Standard*, *Medium* and *Shallow* beams respectively. These values are a much better match to those observed and shown in Table 2. Using the average of the values shown in the table and the theoretical calculated values above, the actual values of η_B can be calculated and are, 0.87, 0.75 and 0.97 for each of the beam sizes respectively; however, the *Medium* and *Shallow* values must be treated with caution as only one beam was available of each size as *Shallow 1* and *Medium 2* were discarded from these calculations.

Figures 7a to 7h show the probability density function (*pdf)* of the angle θ for all beams. It is clear that the *Standard* beams present a more random distribution of θ. However, there are more fibres included in the horizontal plane (i.e. θ=0); this observation is similar to that presented by Ozyurt et al using AC impedance spectroscopy [37]. Conversely, the *Medium* and *Shallow* beams presented a more uniform distribution of angles. A potential explanation could be wall effects as the width to depth ratio is much smaller than in the *Standard* beams. However, Soroushian and Lee [52] showed that samples where one or more dimensions are less than 5 times the fibre length, the fibres will tend to orientate in horizontal planes, or planes parallel to the walls. The element height to fibre to length ratio was approx 5.0, 1.67 and 1.1 for *Standard*, *Medium* and *Shallow* beams and therefore, according to this, it would be expected orientations different to those observed. On the other hand, Martinie & Roussel [56] showed that shear induced orientation dominates orientation profiles at the centre of samples, leaving the fibres orientated in more random angles; a fact shown also by Zerbino et al [7]. The prevalence of this second effect therefore may explain why the *Medium* and *Shallow* beams present these angle distributions although this was not proven.

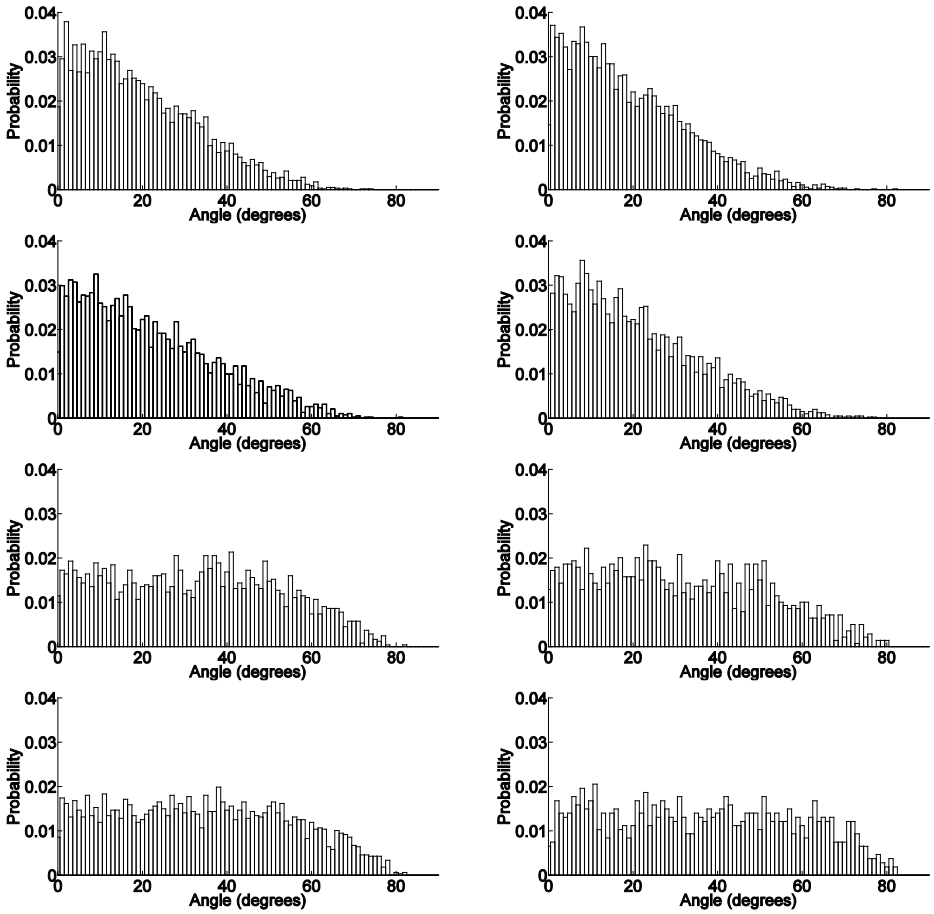

Figure 7. Probability density functions of all the beams. Left-to-right from the top: (a) Standard 11(b) Standard 12 (c) Standard 21 (d) Standard 22 (e) Medium 2 (f) Medium 3 (g) Shallow 1 (h) Shallow 2.

The observed fibre distribution and number of fibres in cross sections was compared against values in the literature. Stahli et al [4] showed that the number of fibres (with very similar geometry to that used in this work) in a given cross section was 0.06122 fibres/mm^2 in a 70 mm x 70 mm section for a volume of fraction of fibres equal to 3.0%; if extrapolated to the *Standard* beams used here and divided by 3.0 to match the 1% volume fraction of the test, the total number of fibres should be 459; which does not match the values presented in Table 2. Hence, there seems to be a discrepancy. The apparent discrepancy could well be due to the significant differences in wall effects in Stahli et al's [71] experiments and Laranjeira et al [55] and shear induced orientation [9,56]. The wider variability shown in the literature justifies the differences. For instance, Zerbino et al [7] showed values of approximately 0.02 fibres/mm^2 (i.e. 3 times lower than Stahli et al [4]) for a volume of fraction of 0.45% and Robins et al [47] values of 0.01 to 0.02 for a 1% fibres volume fraction. The values in Table 2, which average 0.04, when excluding *Medium*2 and *Shallow* 1, seem to fall within the limits presented by Zerbino et al [7] and are slightly higher than those presented by Robins et al [47].

The fibre reconstruction also allowed calculating the fibre distribution statistically within a cross section. For this purpose, two statistical methods for point pattern analysis were used: Nearest Neighbour Analysis (NNA) [72] and the Quadrant Analysis (QA) [73]. Both methods provide indicators of the randomness of the distributions by classifying the pattern into three different spatial arrangements:

- Random: Points are equally likely to occur at any location and the position of any point is not affected by the position of any other point – Limiting values: NNI (1.0) and QA (1.0)
- Uniform: All points present the greatest possible distance from the nearest points. – Limiting values: NNI (2.15) and QA (<1.0)
- Clustered: Points concentrate around each other at one area, with other areas containing almost no points. – Limiting values: NNI (0.0) and QA (>1.0)

Table 2 shows the results for the crack section of each beam (i.e. where the notch was cut). These calculations can be used as an indication of whether segregation is present in a specimen. It can be seen that, in this case, the distribution of fibres is reasonably close to a random distribution in all cases and hence, can be concluded that no segregation occurred. These results have been more recently confirmed by Akkaya et al [57] and Ozyurt et al [34]. It also suggests that there is the same probability of number of fibres at different depths within the cross section when fibre segregation is not present; a result similar to that presented by Martinie & Roussel [56]. Some authors have shown, however, that clustering in certain areas can occur, mainly due to shear induced orientation and wall effects [7,9,60], although this was not observed in this work.

6. POST-CRACKING BEAM MECHANICAL BEHAVIOUR

In order to assess the mechanical performance using the results obtained from the reconstruction of the beams, fracture mechanics theory was used. This included obtaining and applying two fundamental relationships: the load – crack opening (P-CMOD) relationship and the stress - crack opening (σ_w – CMOD) relationship in a crack. The latter relates to the local behaviour of the crack, whilst the former characterises the overall behaviour of the beam and could be compared to the TPBT results [66].

This work involved the following the steps:

- Calculation of the bilinear relationship that matches the results of P-CMOD obtained in the TPBT using the Hinge model.
- Comparison of the σ_w – CMOD relationship between the inversely calculated bilinear relationship above, and the calculated relationship using the model presented by Li et al [11] and the individual information of all the fibres.

P – CMOD (Hinge model)

Olesen [74] described a nonlinear crack hinge model to predict the bending fracture of concrete beams. His method was based on the concept of Fictitious Crack Model using a bilinear approximation to the σ_w – CMOD relationship.

The method relies on the division of the beam in the vicinity of the crack into layers of independent spring elements. These springs are attached to rigid boundaries at both ends, so that they elongate or contract as the beam deflects. This assumption was confirmed by observing the linear relationship between crack opening and displacement that developed in all tests. For

compatibility, adjacent spring elements move so that the rigid boundaries remain straight. These can then be connected to the rest of the uncracked beam using traditional beam theory. A detailed explanation of the model is shown by Olesen [74].

It has to be noted that the solution is only valid for after the onset of cracking, when the load is the first crack load, P_{crack}. The equation used to calculate P_{crack} was taken from traditional beam theory as

$$P_{crack} = \frac{4I_{section} f_t}{L\,h/2} \tag{4}$$

where $I_{section}$ represents the second moment of inertia of the cross section excluding the notch, f_t is the tensile strength and h is the ligament height. The values of P_{crack} were found to be 19.350, 3.906 and 1.376 kN for the *Standard*, *Medium* and *Shallow* beams respectively.

Also using simple beam theory for a simply supported beam when a load is applied at mid-span, the load P was calculated from the moment M that was obtained through the hinge model

$$P = \frac{4M}{L} \tag{5}$$

where L is the distance between supports, which in this case was 500 mm.

Results are shown in Figure 8. *Standard* and *Medium* beams showed the better agreement with the predictions of the peak load, whereas the *Shallow* beams showed an overestimate at the peak load, but reasonable thereafter.

A unique bilinear approach for all the beams was back-calculated to produce these results, with the following parameters: $a_1 = 20$ mm^{-1}, $a_2 = 0.8$ mm^{-1} and $b_2 = 0.45$ – See Figure 9.These parameters correspond to a specific fracture energy of 0.42 N/mm, which agrees with the values presented by Walter [14] for the same concrete and fibre mixes. Equation 6 shows the formulation of the bilinear relationship; note that w has been used meaning *CMOD* in order to simplify the equations.

$$\sigma_w = \begin{cases} 1 - a_1 w \;\; for \;\; 0 \le w \le w_1 \\ b_2 - a_2 w \;\; for \;\; w_1 < w \le w_2 \end{cases} \tag{6}$$

Stress – CMOD relationship (σw – CMOD)

In order to calculate the σ_w – CMOD relationship using the reconstructed information of the fibres within the beams a model shown by Li et al [10,12] was used.

This model divides the σ_w – CMOD relationship into three contributions: aggregate bridging(σ_a), fibre bridging (σ_f) and fibre pre-stressing. The latter has been ignored in this work following the recommendation of the model authors [11]. Hence, only two contributions are calculated and compounded as shown below.

$$\sigma_w(w) = \sigma_a(w) + \sigma_f(w) \tag{7}$$

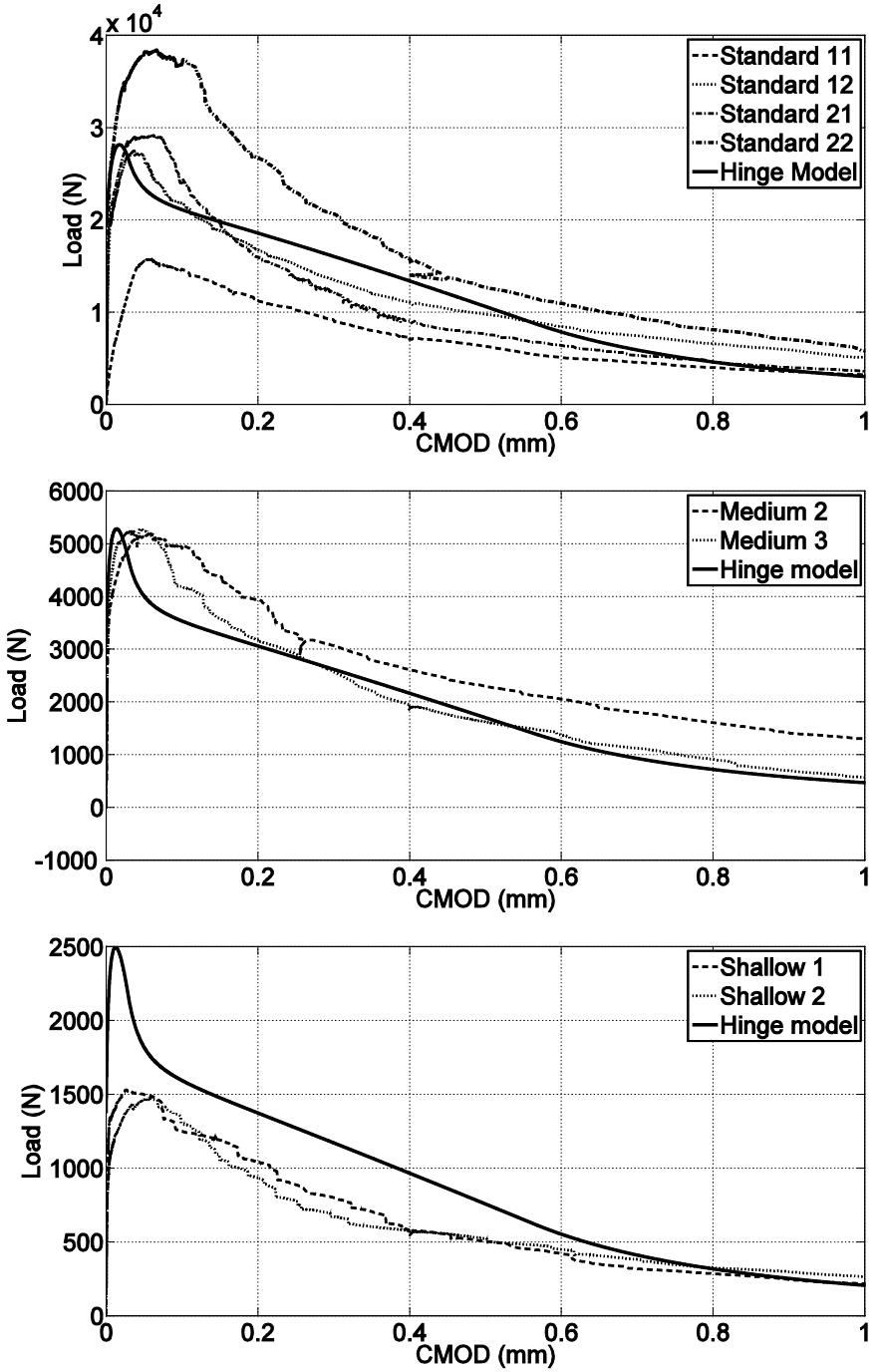

Figure 8. Hinge model back-analysis for all the beams. Left-to-right from the top: (a) Standard beams (b) Medium beams (c) Shallow beams

Aggregate bridging is characterised in [2].

$$\sigma_a(w) = \frac{\sigma_m^u}{1 + \left(\frac{w}{w_0}\right)^p} \tag{8}$$

Where:

- σ_m^u is the maximum bridging stress due to aggregate action at w = 0.
- p is a factor that describes the shape of the softening process with increasing opening and has been taken as 1.5 [2].
- w_0 is the crack opening when the stress has fallen to half of σ_m^u and was taken as 0.015 [2].

The value of $\sigma_m{}^u$ should be slightly smaller than the tensile strength of the concrete as recommended by the author [2]. However, since fibre pre-stress and the chemical bond were neglected, the value was taken as equal to the tensile strength; this guarantees that Equation 8 holds as when the two contributions to the softening behaviour, namely fibres and aggregates, are added, for $w = 0$, it follows that σ_f equals 0 and σ_a equals $\sigma_u{}^m$.

Fibre bridging was calculated under the assumption that it occurs in two stages; debonding and pull-out. Fibres rupture and chemical bonding have also been disregarded. The former assumption was verified by visual inspection after failure of the beams which did not show fibre rupture.

Using the above assumptions, the equations presented by Lin et al [75] for a fibre, perpendicular to the crack face, can be used for the debonding stage, pull-out and for when the fibre has been pulled completely (see Eq. 9 to 11). The parameters δ, δ_0 and L_e represent the crack opening, initial crack opening and embedded length of fibre respectively.

Li et al [11] extended this to non-perpendicular fibres via the concept of snubbing factor, f, multiplying by $e^{f\Phi}$, to cater for fibres which are inclined at an angle Φ using the analogy of a rope pulling against a frictional pulley. The value of f was 0.75 [10].

$$P(\delta) = \frac{\pi}{2}\left[(1+\eta)E_f d_f^3 \tau \delta\right]^{1/2} e^{f\phi} \; for \;\; \delta \le \delta_0 \tag{9}$$

$$P(\delta) = \pi \tau L_e d_f \left(1 - \frac{\delta - \delta_0}{L_e}\right) e^{f\phi} \; for \;\; \delta_0 \le \delta \le \delta_0 + L_e \tag{10}$$

$$P(\delta) = 0 \;\; for \;\; \delta_0 + L_e \le \delta \tag{11}$$

Where

$$\delta_0 = \frac{4\tau_0 L_e^2 (1+\eta)}{E_f d_f} \tag{12}$$

And

$$\eta = \frac{V_f E_f}{V_c E_c} \tag{13}$$

The terms E_f and E_c represent the Young's Modulus of the fibres and the concrete matrix respectively. Values of 210 MPa and the calculated value of 35 MPa were respectively taken for the analysis.

The bond between fibre and matrix is controlled by the shear stresses τ_0 and τ, and represent the friction between the two as shown in the equations below

$$\tau = \tau_0 for\ 0 < \delta \le \delta_0 \tag{14}$$

$$\tau = \tau_0\left(1 + \beta_1(\delta - \delta_0)/d_f + \beta_2(\delta - \delta_0)^2/d_f^2\right) \quad for\ \delta_0 < \delta < \delta_0 + L_e \tag{15}$$

The value of τ_0 was found to be 4.0 MPa for optimal fitting of the bilinear approach. The β-coefficients, β_1 and β_2 in Equation 15 were -2.0 and 0.5 respectively as presented by Stang et al [15]. They were obtained by multiplying Stang et al's values of -4.0 and 1.0, by the fibre diameter, d_f, due to the slightly different formulation.

The same authors also report that it must be noted that in the above equations, δ represents the crack mouth opening associated only with debonding and pull-out of the fibres and hence, does not represent the total crack mouth opening, w. The total crack mouth opening has an additional contribution [76], which was first found by Cook & Gordon [77] due to debonding ahead of a crack and coalescence, and has since received its name. The authors show that w responds to.

$$w = \delta + \delta_{cg} \tag{16}$$

where δ_{cg} represents the Cook-Gordon contribution. The value of δ_{cg} can be calculated using [47].

$$\delta_{cg} = \frac{4\alpha_{cg}P}{\pi d_f^2 E_f} \tag{17}$$

A value of $\alpha_{cg} = 20d_f$ was taken, which is similar to the value provided by Li et al [10].

Since, the location of all the bridging fibres had been calculated along with their orientation, the total contribution due to fibre bridging could be calculated by prescribing values of δ using Equations 18 and 19.

$$P_f(w) = \sum_{i=bridgingfibres} P_i(w) \tag{18}$$

$$\sigma_f(w) = \frac{P_f(w)}{A} \tag{19}$$

where A represents the uncracked cross sectional area of the beam.

The construction of the relationship followed the following steps for each crack opening value, δ:

- Calculation of τ for each fibre using Equations 14 and 15.
- Determination of which phase is each single fibre at, and application of the Equations 9 to 11 accordingly.
- Summation of all the contributions from all fibres for a single prescribed crack opening using Equation 18 and calculation of the stress using Equation 19.

Results are presented in Figure 9. This figure shows good agreement for all the beams with the exception of *Shallow* 1 and *Medium* 2 which are not shown since their unusual number of calculated crack bridging fibres provided unrealistic results. Löfgren [69] highlights that the fitting interval has to be carefully chosen since using a bi-linear approximation could make fitting over the whole curve impossible. In this case, the end part of the curve was chosen presents a better fit. This interval was more adequate since because the effects of aggregate bridging, and fibre pre-stress were not considered and therefore, the accuracy was lower for smaller values of w.

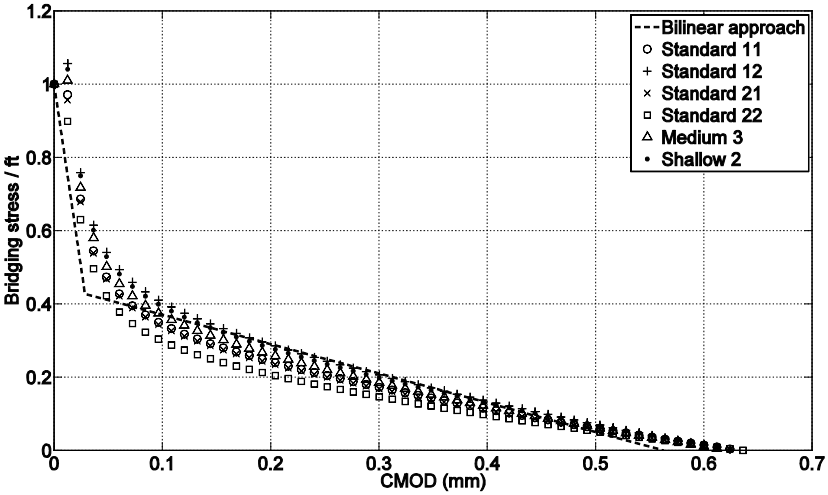

Figure 9. Bilinear back-calculated relationship from Hinge Model and prediction for all beams using micromechanical model

The results show that the stress-crack opening relationship can be accurately modelled using simple micromechanical models when the information of all the individual contributing fibres is known.

This presents a unique tool for single fibre pull-out model validation and, consequentially provide a more accurate estimate of post-cracking behaviour in FRC.

7. CONCLUSIONS

CT imagery was successfully used for the reconstruction of the position of the fibres within beams of different thicknesses and presented a solution to deal with the unsolved problem of clusters present in all FRC elements. The results were used to calculate their orientations and allowed the derivation of a *pdf* for the 3D orientation of all beams. It showed that, in the direction perpendicular to the beam vertical cross section, this followed a Gaussian distribution of mean 47.55 and standard deviation 18.17. Fibres in laboratory beams, cast using RILEM indications [67] and sizes (*Standard* in this paper), tend to orientate in planes close to horizontal. On the other hand, shallower beams present a more uniform distribution which could be due to shear induced effects overcoming wall effects. No fibres were found to be parallel to the beam cross section.

The statistical analysis carried out on the spatial distribution of the fibres within cross sections showed random distributions; this means that segregation was not present in the various specimens.

The beam behaviour at a micro-mechanical level was calculated. Using the Hinge model, a unique bilinear relationship to the σ_w – CMOD with a specific fracture energy of 0.42 N/mm was calculated using the results of the TPBT as comparison. This bilinear relationship was then

compared to the calculated ones obtained by adding the contributions of each single fibre within the beams. The results compared to the bilinear relationship satisfactorily; this confirms the potential of this technique for the accurate validation of micro-mechanical models to model the (average) post-cracking behaviour of fibre reinforced concrete when removing the uncertainty of content, distribution and orientation of the fibres within a concrete matrix.

However, more mixes, fibres volume fractions and element sizes will be needed in order for the technique to be fully validated widely.

ACKNOWLEDGEMENTS

The authors would like to thank the Department of Chemical and Biochemical Engineering of DTU for allowing us to use the CT Scanner, and particularly to Dr. Alexander Shapiro for his help with the use of the CT-Scanner.

REFERENCES

[1] C. K. Y. Leung and V. C. Li Effect of fiber inclination on crack bridging stress in brittle fiber reinforced matrix composites. *J. of the Mechanics and Physics and Solids*, 40:6 (1992) 1333-1362.

[2] H. Stang. Evaluation of properties of cementitious fiber composite materials, in H.W. Reinhardt & A. E. Naaman (eds), High Performance Fiber Reinforced Cement Composites, 1992, Vol. 1, E & FN Spon, London, 388–406.

[3] G. Li, D. Maricherla, K. Singh, S-S. Pang, and M. John,. Effect of fiber orientation on the structural behaviour of FRP wrapped concrete cylinders. *Composite Structures* 74 (2006) 475–483.

[4] P. Stahli, R. Custer, and J.G. van Mier. On flow properties, fibre distribution, fibre orientation and flexural behaviour of FRC. *Materials and Structures* 41 (2008) 189-196.

[5] P. Stroeven. Stereological principles of spatial modelling applied to steel fibre-reinforced concrete in tension. *ACI Materials J.*, 106:3 (2009) 213-222.

[6] S. J. Barnett, J-F. Lataste, T. Parry and S. G. Millard, Soutsos, M.N. Assessment of fibre orientation in ultra high performance reinforced concrete and its effect on flexural strength. *Materials and Structures*, 43 (2010) 1009–1023.

[7] R. Zerbino, J. M. Tobes, M. E. Bossio and G. Giaccio. On the orientation of fibres in structural members fabricated with self compacting fibre reinforced concrete. *Cement & Concrete Composites* 34 (2012)191–200.

[8] A. Abrishambaf, J. A. O. Barros and V. M. C. F. Cunha. Relation between fibre distribution and post-cracking behaviour in self-compacting concrete panels. *Cem. Concr. Res.* 51 (2013) 57–66.

[9] Švec, O., Žirgulis, G., Bolander, J.E., Stang, H. Influence of formwork surface on the orientation of steel fibres within self-compacting concrete and on the mechanical properties of cast structural elements (2014) *Cem. Concr. Compos*, 50, 60-72.

[10] V. C. Li, H. Stang, and H. Krenchel, Micromechanics of Crack Bridging in Fibre-Reinforced Concrete. *Materials and Structures* 26 (1993) 486-494.

[11] V. C. Li, Y. Wang and S. Backer. Effect of inclining angle, bundling and surface treatment on synthetic fiber pull-out from cement matrix, *Composites* 21:2 (1990) 132–140.

[12] V. C. Li Post-Crack scaling relations for fiber reinforced cementitious composites. *ASCE J. Mat. Civil Eng.* 4:1 (1992) 41-57.

[13] J.E. Bolander, S.Choi, and S.R.Duddukuri. Fracture of fiber-reinforced cement composites: effects of fiber dispersion. *Int. J. Frac*., 154:1-2, (2008) 73-86.

[14] R. Walter. Cement-Based Overlay for Orthotropic Steel Bridge Decks A Multi-Scale Modeling Approach. Ph.D. Thesis. Department of Civil Eng.. Technical University of Denmark. 2005.

[15] Stang, H., Li, V. C. and Krenchel, H. (1995). Design and structural applications of stress-crack width relations in fibre reinforced concrete. *Materials and Structures*, 28(178), pp. 210-219.

[16] Barragán, B.E., Gettu, R., Martín, M.A., Zerbino, R.L. Uniaxial tension test for steel fibre reinforced concrete - A parametric study. (2003) *Cem. Concr. Compos*, 25 (7), 767-777

[17] Kang, S.-T., Kim, J.-K. The relation between fiber orientation and tensile behavior in an ultra high performance fiber reinforced cementitious composites (UHPFRCC). (2011) *Cem. Concr. Res.*, 41 (10), 1001-1014

[18] Kang, S.T., Lee, B.Y., Kim, J.-K., Kim, Y.Y. The effect of fibre distribution characteristics on the flexural strength of steel fibre-reinforced ultra high strength concrete. (2011) *Construction and Building Materials*, 25 (5) 2450-2457

[19] Li, G., Maricherla, D., Singh, K., Pang, S.-S., John, M. Effect of fiber orientation on the structural behavior of FRP wrapped concrete cylinders. (2006) *Comp. Struct.*, 74 (4), pp. 475-483

[20] Au, C., Buyukozturk, O. Effect of fiber orientation and ply mix on fiber reinforced polymer-confined concrete (2005) *J. of Composites for Construction*, 9 (5), 397-407

[21] Giaccio, G., Tobes, J.M., Zerbino, R. Use of small beams to obtain design parameters of fibre reinforced concrete (2008) *Cem. Concr. Compos*, 30 (4), 297-306
Linear relationship between displacement – CMOD.

[22] Vincent, T., Ozbakkaloglu, T. Influence of fiber orientation and specimen end condition on axial compressive behavior of FRP-confined concrete (2013) *Construction and Building Materials*, 47, 814-826

[23] Edgington, J., Hannant, D.J. Steel fibre reinforced concrete. The effect on fibre orientation of compaction by vibration (1972) *Matériaux et Constructions*, 5 (1), 41-44

[24] Sadeghian, P., Rahai, A.R., Ehsani, M.R. Effect of fiber orientation on compressive behavior of CFRP-confined concrete columns (2010) *J. of Reinforced Plastics and Comp.*, 29 (9), 1335-1346

[25] Wille, K., Tue, N.V., Parra-Montesinos, G.J. Fiber distribution and orientation in UHP-FRC beams and their effect on backward analysis (2013) *Materials and Structures*, 1-14

[26] Sanal, I., Özyurt Zihnioglu, N. To what extent does the fiber orientation affect mechanical performance? (2013) *Construction and Building Materials*, 44, 671-681

[27] Sarmiento, E.V., Hendriks, M.A.N., Kanstad, T. Accounting for the fibre orientation on the structural performance of flowable fibre reinforced concrete (2014) Computational Modelling of Concrete Structures - Proceedings of EURO-C 2014, 2, 609-618

[28] Rosenbusch, J. Einfluß der Faserorientierung auf die Beanspruchbarkeit von Bauteilen aus Stahlfaserbeton (2004) *Beton- und Stahlbetonbau*, 99 (5), 372-377

[29] Lee, S.-C., Cho, J.-Y., Vecchio, F.J. Diverse embedment model for steel fiber-reinforced concrete in tension: Model development (2011) *ACI Materials J.*, 108 (5), 516-525

[30] Lee, S.-C., Cho, J.-Y., Vecchio, F.J. Diverse embedment model for steel fiber-reinforced concrete in tension: Model verification (2011) *ACI Materials J.*, 108 (5), 526-535.

[31] Pujadas, P., Blanco, A., Cavalaro, S.H.P., De La Fuente, A., Aguado, A. Multidirectional double punch test to assess the post-cracking behaviour and fibre orientation of FRC (2014) *Construction and Building Materials*, 58, 214-224.

[32] Torrijos, M.C., Barragán, B.E., Zerbino, R.L. Placing conditions, mesostructural characteristics and post-cracking response of fibre reinforced self-compacting concretes.(2010) *Construction and Building Materials*, 24 (6), pp. 1078-1085.

[33] Zhou, B., Uchida, Y. Fiber orientation in ultra high performance fiber reinforced concrete and its visualization (2013) Proceedings of the 8th International Conference on Fracture Mechanics of Concrete and Concrete Structures, FraMCoS 2013, 228-235

[34] N. Ozyurt, Y. W. Leta, T. O. Mason and S. P. Shah. Monitoring fibre dispersion in fibre-reinforced cementitious materials: comparison of AC-Impedance spectroscopy and image analysis. *ACI Materials J.* 103:5 (2006) 340-347

[35] T.O Mason, M.A Campo, A.D Hixson, L.Y Woo.Impedance spectroscopy of fiber-reinforced cement composites. *Cem. Concr. Compos* 24:5 (2002) 457-465

[36] L.Y. Woo, S. Wansom, N. Ozyurt, B. Mu, S.P. Shah, T.O. Mason. Characterizing fiber dispersion in cement composites using AC-Impedance Spectroscopy. *Cem. Concr. Compos,* 27:6 (2005) 627-636.

[37] N.Ozyurt, T.O. Mason and S.P. Shah. Non-destructive monitoring ofiber orientation using AC-IS: an industrial-scale application. *Cem. Concr. Res.* 36 (2006) 1653–1660.

[38] Lataste, J.F., Behloul, M., Breysse, D. Characterisation of fibres distribution in a steel fibre reinforced concrete with electrical resistivity measurements. (2008) *NDT E Int.*, 41 (8), 638-647.

[39] Eik, M., Lõhmus, K., Tigasson, M., Listak, M., Puttonen, J., Herrmann, H. DC-conductivity testing combined with photometry for measuring fibre orientations in SFRC (2013) *J. of Materials Science*, 48 (10), 3745-3759.

[40] H.W. Reinhardt, C.U. Grosse, B. Weiler, Material Characterization of Steel Fibre Reinforced Concrete Using Neutron CT, Ultrasound and Quantitative Acoustic Emission Techniques, 6, *NDT International*, 2001,(No.5).

[41] Faifer, M., Ferrara, L., Ottoboni, R., Toscani, S. Low frequency electrical and magnetic methods for non-destructive analysis of fiber dispersion in fiber reinforced cementitious composites: An overview (2013) *Sensors (*Switzerland), 13 (1), pp. 1300-1318.

[42] Ferrara, L., Faifer, M., Muhaxheri, M., Toscani, S. A magnetic method for non destructive monitoring of fiber dispersion and orientation in steel fiber reinforced cementitious composites. Part 2: Correlation to tensile fracture toughness (2012) *Materials and Structures/Materiaux et Constructions*, 45:4 591-598.

[43] Ferrara, L., Faifer, M., Muhaxheri, M., Toscani, S., Ottoboni, R. Non destructive monitoring of fiber dispersion and flow-induced orientation in self-compacting SFRC: A method based on magnetic properties (2012) RILEM Bookseries, 6, 117-123.

[44] Ferrara, L., Faifer, M., Toscani, S. A magnetic method for non destructive monitoring of fiber dispersion and orientation in steel fiber reinforced cementitious composites-part 1: Method calibration *Materials and Structures/Materiaux et Constructions* (2012), 45:4 575-589.

[45] R. Fuentes. Influence of Fibre Orientation on the Mechanical Properties of Fibre Reinforced Concrete. Assessment based on images acquired from CT-Scans. MSc. Thesis. Department of Civil Eng.. Technical University of Denmark. 2003.

[46] K. A. Heiskanen, H. C. Rhim and J.M. Monteiro. Computer simulations of limited angle tomography of reinforced concrete. *Cem. Concr. Res.*. 21:4 (1991) 625-634.

[47] P. J. Robins, S. A. Austin and P. A. Jones. Spatial distribution of steel fibres in sprayed concrete and cast concrete. *Magazine of Concrete Research* 55:3 (2003) 225–235.

[48] R. C. K. Wong and K. T. Chau. Estimation of air void and aggregate spatial distributions in concrete under axial compression using computer tomography scanning. *Cem. Concr. Res.* 35 (2005) 1566–1576.

[49] Vicente, M.A., González, D.C., Mínguez, J. Determination of dominant fibre orientations in fibre-reinforced high-strength concrete elements based on computed tomography scans (2014) *Nondestructive Testing and Evaluation*, . Article in Press.

[50] Schnell, J., Schladitz, K., Schuler, F. Direction Analysis of Fibres in Concrete on Basis of Computed Tomography [Richtungsanalyse von Fasern in Betonen auf Basis der Computer-Tomographie] (2010) *Beton- und Stahlbetonbau*, 105 (2), 72-77.

[51] Kaufmann, J., Frech, K., Schuetz, P., Münch, B. Rebound and orientation of fibers in wet sprayed concrete applications (2013) *Construction and Building Materials*, 49, 15-22.

[52] P. Soroushian and C-D. Lee. Distribution and Orientation of Fibers in Steel Fiber Reinforced Concrete, *ACI Materials J.*, 87:5 (2010) 433-439.

[53] D. Dupont and L. Vandewalle. Distribution of steel fibres in rectangular sections. *Cement & Concrete Composites* 27 (2005) 391–398.

[54] Laranjeira, F., Grünewald, S., Walraven, J., Blom, C., Molins, C., Aguado, A. Characterization of the orientation profile of steel fiber reinforced concrete. *Materials and Structures/Materiaux et Constructions* (2011) 44:6 1093 – 1111.

[55] Laranjeira, F., Aguado, A., Molins, C., Grünewald, S., Walraven, J., Cavalaro, S. Framework to predict the orientation of fibers in FRC: A novel philosophy. *Cem. Concr. Res.* 42:6 (2012) 752 – 768

[56] L. Martinie and N. Roussel. Simple tools for fiber orientation prediction in industrial practice. *Cem. Concr. Res.* 41:10 (2011) 993-1000.

[57] Y.Akkaya, J. Picka, and S. P. Shah. Spatial Distribution of Aligned Short Fibers in Cement Composites. *J. of Materials in Civil Eng.* 12:3 (2000) 272-279.

[58] Kang, S.-T., Kim, J.-K. Numerical simulation of the variation of fiber orientation distribution during flow molding of ultra high performance cementitious composites (UHPCC) (2012) *Cem. Concr. Compos*, 34 (2), 208-217.

[59] Krour, B., Bernard, F., Tounsi, A. Fibers orientation optimization for concrete beam strengthened with a CFRP bonded plate: A coupled analytical-numerical investigation (2013) *Eng. Structures*, 56, 218-227.

[60] Deeb, R., Karihaloo, B.L., Kulasegaram, S. Reorientation of short steel fibres during the flow of self-compacting concrete mix and determination of the fibre orientation factor (2014) *Cem. Concr. Res.*, 56, 112-120.

[61] Ferrara, L., Tregger, N., Shah, S.P. Flow-induced fiber orientation in SCSFRC: Monitoring and prediction (2010) RILEM Bookseries, 1, 417-428.

[62] Barr, B.I.G., Lee, M.K., De Place Hansen, E.J., Dupont, D., Erdem, E., Schaerlaekens, S., Schnütgen, B., Stang, H., Vandewalle, L. Round-robin analysis of the RILEM TC 162-TDF beam-bending test: Part 3 - Fibre distribution (2003) *Materials and Structures/Materiaux et Constructions*, 36 (263), 631-635.

[63] J.L. Chermant, L. Chermant, M. Coster, A.S. Dequiedt, C. Redon, F. Soare, Some applications of automatic image analysis in civil Eng., *Cem. Concr. Compos*. 23 (2001) 157–169.

[64] C. Redon, L. Chermant, J.L. Chermant, M. Coster. Assessment of fibre orientation in reinforced concrete, using Fourier image transform. *J Microscopy*, 191 (3) (1998), 258–265

[65] C. Redon, L. Chermant, J.-L. Chermant, M. Coster. Automatic image analysis and morphology of fibre reinforced concrete. *Cem. Concr. Compos*, 21:5–6 (1999) 403-412.

[66] M.J. Baker, P.G. Young, G.R. Tabor. Image based meshing of packed beds of cylinders atlow aspect ratios using 3d MRI coupled with computationalfluid dynamics. *Computers and Chemical Eng.* 35 (2011) 1969–1977.

[67] RILEM TC 162-TDF. Test and design methods for steel fibre reinforced concrete. Recommendations – Bending Test. In Materials and Structures 33 (2000) 3-5.

[68] A. M. Neville. Properties of Concrete. Prentice Hall. Fourth Edition. 1995

[69] ACI 318-95. Building code requirements for structural concrete, ACI Manual of Concrete Practice Part 3: Use of Concrete in Buildings – Design, Specifications, and Related Top., 345 1996.

[70] I. Löfgen. Fibre-reinforced concrete for industrial construction – a fracture mechanics approach to material and structural analysis. PhD Thesis. Department of Civil and Environmental Eng.. Chalmers University of Technology. Sweden, 2005.

[71] P. Hunt, P. Engler, C. Bajsarowicz. Computed Tomography as a Core Analysis Tool: Applications, Instrument Evaluation, and Image Improvement Techniques. *J. of Petroleum Technology* 40 (9), 1203-1210.

[71] P. Stahli, and J. G. van Mier. Manufacturing, fibre anisotropy and fracture of hybrid fibre concrete. *Eng. Fracture Mechanics* 74 (2007) 223–242.

[72] P. J. Clark and F. C. Evans, Distance to nearest neighbour as a measure of spatial relationships in populations. *Ecology* 35 (1954) 445-453.

[73] H. A. Gleason. Some applications of the quadrat method, *Bulletin of Torrey Bothanical Club*, 47:1 (1920) 21-33.

[74] J. F. Olesen. Fictitious Crack Propagation in Fibre-Reinforced Concrete Beams. *J. of Eng. Mechanics*, 2001, 127:3 (2001) 272-280.

[75] Z. Lin, T. Kandaa and V.C. Li. On Interface Property Characterization and Performance of Fiber Reinforced Cem. Composites, *J. Concrete Science and Eng.*, RILEM, 1 (1999) 73-184.

[76] Y. S. Jenq and S. P. Shah. A Fracture Toughness Criterion for Concrete. *Eng. Fract. Mech.* 21:5 (1985) 1055-1069.

[77] J. Cook and J. E. Gordon. A mechanism for the control of crack propagation in all brittle systems, *Proc. Roy. Soc*. 282A (1964) 508–520.

Optimising carbon dioxide emissions from concrete with two cements using nonlinear modelling

Dr. Abhay Bulsari
Nonlinear Solutions Oy
Kaivokatu 10 A 21, Fin-20520 Turku
E-mail: abulsari@abo.fi

R&D Director
Lic.Sc.Tech. Klaus Juvas
Consolis Technology Oy Ab
Box 72, Fin-21291 Rusko
E-mail: klaus.juvas@consolis.com

Project Manager
Olli Skyttä
Consolis Technology Oy Ab
Box 72, Fin-21291 Rusko
E-mail: olli.skytta@consolis.com

ABSTRACT

Environmental issues are becoming more important in concrete industries, and there is a concern for carbon dioxide emissions. This work focussed on determining the minimum carbon dioxide emissions in one case of no slump concrete with two cements. Without any constraints on strength or workability, the optimal recipe would not use any cement at all. With a lower limit on early strength, cement becomes necessary in the optimal recipe, which necessitates water, and then the upper limit on workability in terms of cycles makes this a more complicated issue.

To be able to calculate the minimum carbon dioxide emissions with constraints on workability and early strength, models are needed for workability and early strength besides carbon dioxide emissions. The relations between workability and the composition variables of concrete are not simple. Nonlinear models were therefore developed for workability and early strength from experimental data. The nonlinear models, in the form of feed-forward neural networks, show a very high degree of correlation. They were then implemented in suitable software which made it easy to calculate the minimum carbon dioxide emissions. The minimum usually requires smaller amounts of CEM II for different limits on workability and strength.

Key words: carbon dioxide emissions, nonlinear modelling, feed-forward neural networks, optimisation

1. INTRODUCTION

In future, environmental issues could sometimes dictate the recipes for concretes, and there is a tendency towards reducing carbon dioxide emissions. About 5 to 7% [1 - 4] of the global carbon dioxide emissions come from the concrete industry. There is a good amount of literature on the sources of carbon dioxide emissions in cement manufacture [1, 3], life cycle analysis of concrete [5], and carbon capture and storage from cement production [3], but there is very little literature on minimizing the emissions by developing better recipes [2, 6].

Carbon dioxide emissions are reduced primarily by reducing the use of cements, since most of the carbon dioxide emissions in concrete industry come from cements. This can be achieved by better packing of aggregates or better paste composition. Cement industry also tries to offer cements with added fly ash or slag, which in certain proportions is called CEM II. CEM II may not harden as fast, depending on its composition. Thus increasing the proportion of CEM II is not a good solution if a certain early strength is needed. Early strength can be achieved by reducing water, but that could adversely affect the workability. Therefore the whole picture, as shown in Figure 1, has to be kept in mind while trying to minimize carbon dioxide emissions.

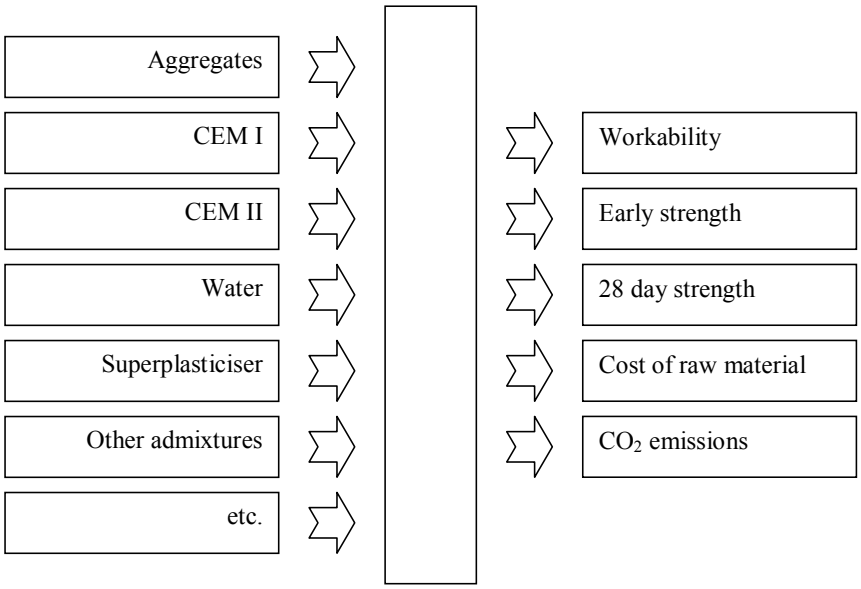

Figure 1 – Concrete properties and carbon dioxide emissions depend on the composition of concrete

2. NONLINEAR MODELLING

Mathematical models represent knowledge of quantitative effects of relevant variables in a concise and precise form. They can be used instead of experimentation if they are reliable enough. Mathematical models also permit the user to carry out various kinds of calculations, like optimisation, which can be used to improve quality or increase production rate.

Mathematical modelling can be performed in various ways, and different ways are suitable in different situations.

It is not possible to use physical modelling in many situations. Even if it is possible, physical models tend to compute the output more slowly than empirical or semi-empirical models. Development of physical models is time consuming. Nonlinear modelling tends to be expensive, but physical modelling usually costs even more. Physical models involve assumptions and simplifications, and thus are less accurate than empirical or semi-empirical models, which reflect reality better. Thus empirical or semi-empirical modelling is often a better alternative.

Traditional empirical modelling is based on linear statistical techniques. Nothing in nature is absolutely linear. So it helps to take nonlinearities into account rather than ignore them. If the range of variables is small, linear techniques are sometimes sufficient. New techniques of nonlinear modelling based on artificial neural networks allow us to approximate nonlinearities without specifying in detail the nonlinearties to be accounted for. They allow for free form nonlinearities, unlike linear and nonlinear regression methods.

Since the last twenty years or so, nonlinear modelling has been successfully utilised by various industrial sectors for a variety of purposes from quality control, product development and process guidance to software sensors and fault detection.

Nonlinear modelling can be roughly defined as empirical modelling which takes at least some nonlinearities into account. Nonlinear modelling can be performed in many ways. The simpler ways include polynomial regression and linear regression with nonlinear terms. One can also use basis functions and splines, and in cases where the form of the nonlinearities is known, nonlinear regression can also be used. New techniques of nonlinear modelling are based on free-form nonlinearities and does not require the knowledge of the form of nonlinearities in advance. Artificial neural networks are a set of efficient tools for nonlinear modelling, for reasons mentioned earlier, and particularly the universal approximation capability of feed-forward neural networks [7].

There are many different types of neural networks, and some of them have practical uses in process industries [8, 9]. Feed-forward neural networks have been in use in process industries for about twenty years [9]. Most neural network applications in industries [10-18] ranging from medical materials [10] to optical fibre cables [17] are based on them.

Artificial neural networks usually consist of neurons in layers directionally connected to others in the adjacent layers. The multilayer perceptron (Figure 2) is a kind of a feed-forward neural network.

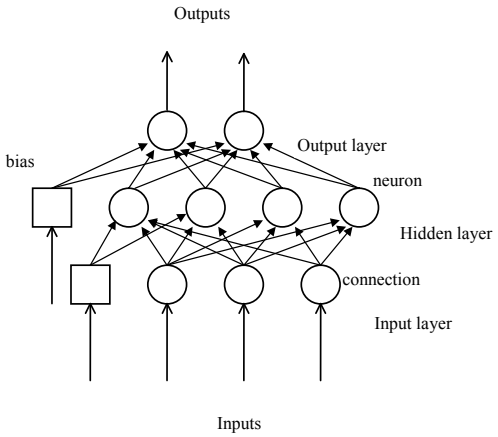

Figure 2 - A typical feed-forward neural network has an input layer, an output layer and one or two hidden layers.

The output of each neuron i in a feed-forward neural network is given by

$$z_i = \sigma\left(\sum_{j=0}^{N} w_{ij} x_j\right) \tag{1}$$

where the activation function is often the logistic sigmoid, given by

$$\sigma(a) = \frac{1}{1+e^{-a}} \tag{2}$$

The incoming signals to the neuron are x_j, and w_{ij} are the weights for each connection from the incoming signals to the i^{th} neuron. The w_{i0} terms are called biases. This results in a set of algebraic equations which relate the input variables to the output variables. Thus, for each observation (a set of input and output variables), the outputs can be predicted from these equations based on a given set of weights. The training procedure (Figure 3) aims at determining the weights which result in the smallest sum of squares of prediction errors. There are a variety of training methods in use today. It is also possible to combine neural networks with physical models or other empirical models, which often lead to better solutions.

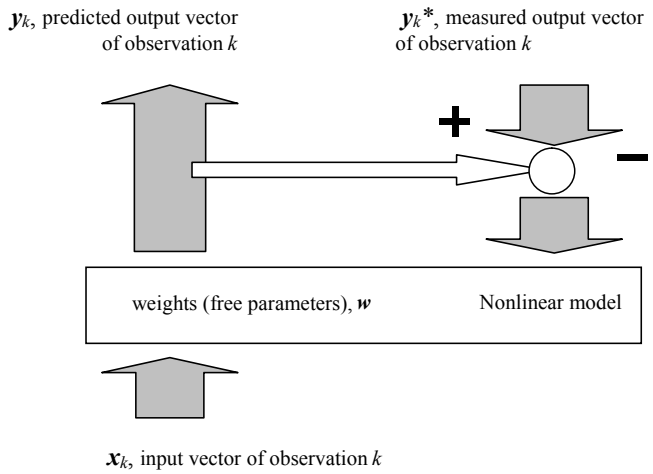

Figure 3 - Training is the process of determining the weights, the free parameters of the model.

3. EXPERIMENTAL DATA

The aggregates and their fractions were fixed first, and 21 experiments were planned with different amounts of CEM I, CEM II, water and superplasticiser. The total amount of cements varied between 285 and 340 kg/m^3 of concrete, while the water to cement ratio varied between 0.438 and 0.531. Table 1 shows the ranges of the variables. There was a good amount of variation in the workability as well as early strength (measured at 16 hours and 20 hours).

Table 1 - Variables and their ranges

Variable	minimum	maximum	average
Input variable	minimum	maximum	average
CEM I, kg	0	340	166.875
CEM II, kg	0	340	152.0833
Water, litres	140	170	152.9167
Superplasticiser, kg	0	3	1.291667
Output variable	minimum	maximum	average
Workabilility, cycles	6	42	17.83333
16 h strength, MPa	16.5	39	30.0375
20 h strength, MPa	20.7	40	33.24583

The data from the 21 experiments was pre-processed and analysed before model development was attempted. Before model development is attempted, usually the data is analysed and pre-

processed. It is more important for production data, but experimental data should also be analysed and pre-processed.

The experimental data were pre-processed and analysed by a pre-processing software, which has several facilities, including simpler things like calculating the basic statistics of the data set, filtering observations with missing measurements or variables beyond the range of interest, calculation of correlation matrices, showing the plots of every variable against every other, etc. It also has more advanced features like clustering, calculating sets of observations with maximum or minimum similarity, and dividing the data into training, test and validation sets required for nonlinear modelling, with desired forms of imbalance in the division.

The plots often reveal some relevant things, like variables which are binary or variable pairs which show a high correlation. Correlation matrices also reveal pairs of variables with high correlations. High correlations between input variables cause inconvenience during modelling, and sometimes one of them has to be excluded. No such problems were found in this data set. High correlations between two output variables, on the hand, is usually very welcome, since such variables can sometimes be treated together as two outputs in the same model.

Figure 4 shows that workability and strength cannot be determined entirely from water to cement ratio. Similarly, the amount of paste also does not determine the workability and strength as seen from Figure 5. This is true even if the superplasticiser amount is constant, since CEM I and CEM II behave somewhat differently. Workability correlates with water to cement ratio as well as with the amount of paste to some extent as can be seen from Figures 4 and 5.

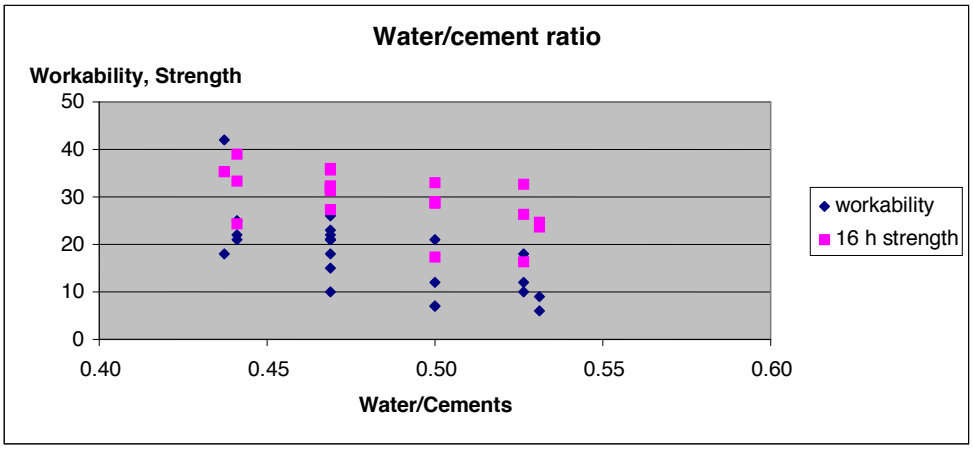

Figure 4 - Workability in cycles and 16 hour early strength in MPa against water to cement ratio

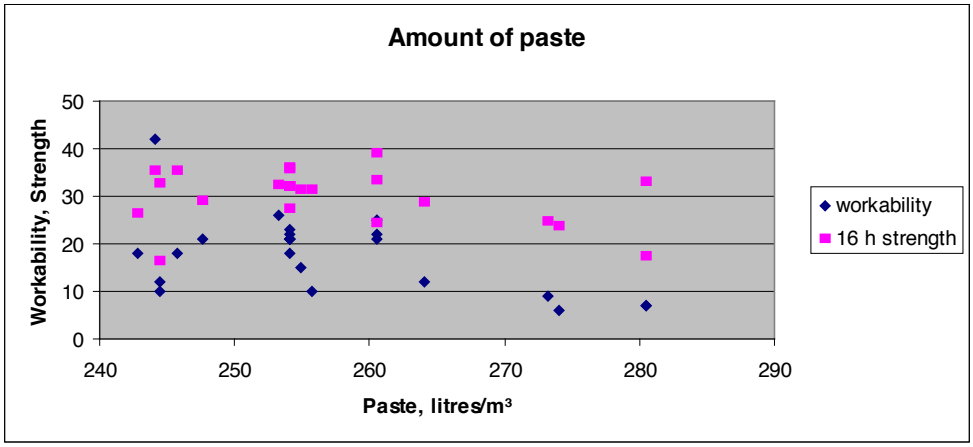

Figure 5 - Workability in cycles and 16 hour early strength in MPa against the amount of paste

Figure 6 shows the effect of CEM I on early strength while keeping the total amount of cements, water and superplasticiser constant. Figure 7 shows the effect of CEM II on early strength while keeping CEM I, water and superplasticiser constant. The effect at 16 hours is stronger than that at 20 hours in both these cases.

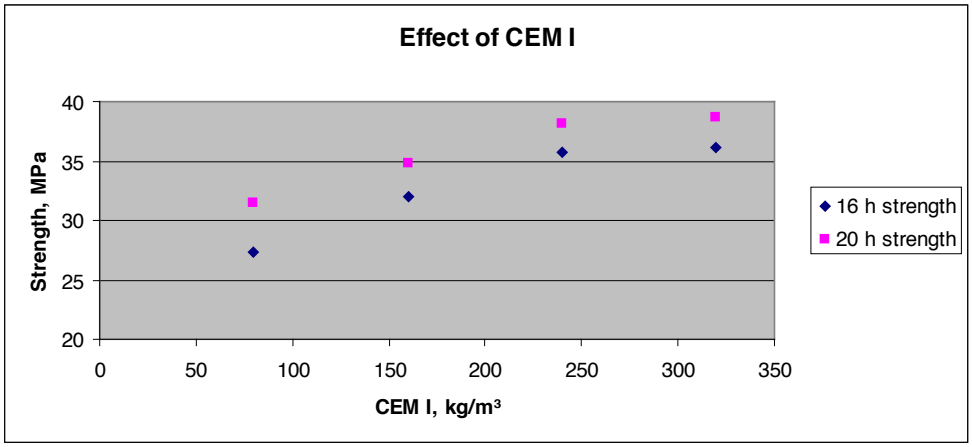

Figure 6 - Effect of CEM I on early strengths at 16 hours and 20 hours in MPa (total amount of cements is constant)

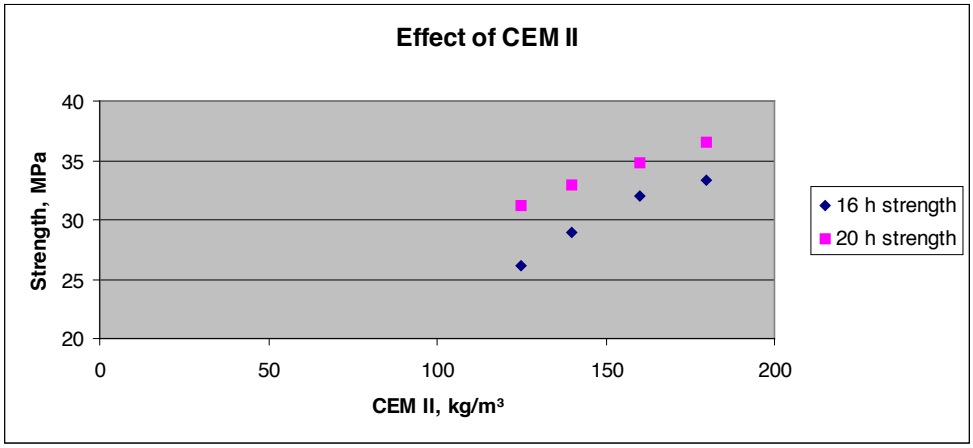

Figure 7 - Effect of CEM II on early strengths at 16 hours and 20 hours in MPa (CEM I is constant; total amount of cements is not constant)

Figure 8 shows the effect of water on early strengths at 16 hours and 20 hours while keeping CEM I, CEM II and superplasticiser constant. The effect is stronger at 16 hours. Similarly, Figure 9 shows the effect of superplasticiser on early strengths at 16 hours and 20 hours while keeping CEM I, CEM II and water constant. The effect at 20 hours is negligible, but there is a small but a visible negative effect at 16 hours.

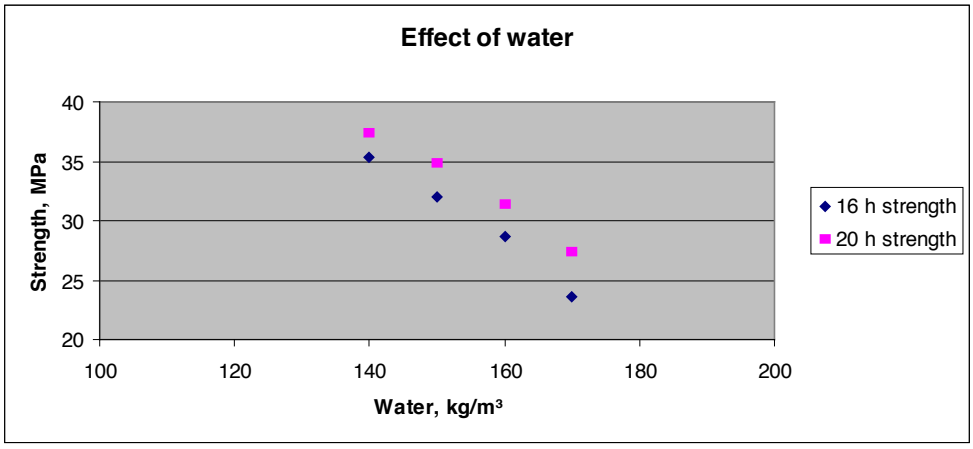

Figure 8 - Effect of water on early strengths at 16 hours and 20 hours in MPa (CEM I, CEM II and superplasticiser are constant)

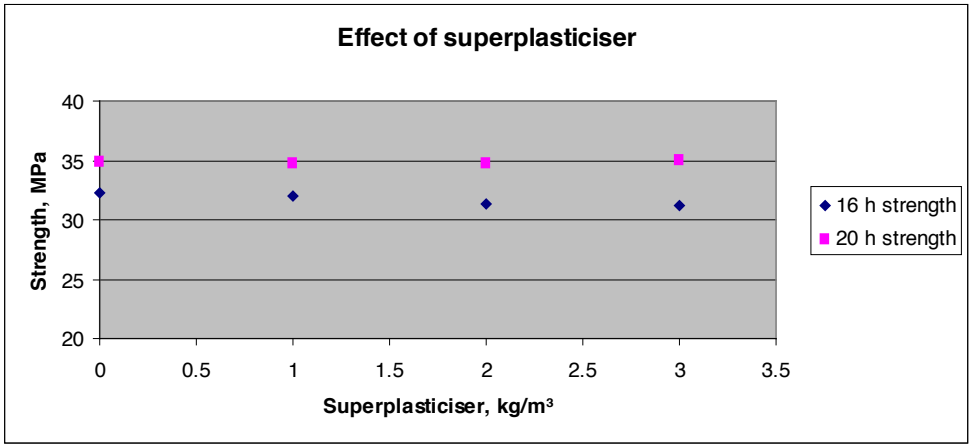

Figure 9 - Effect of superplasticiser on early strengths at 16 hours and 20 hours in MPa (CEM I, CEM II and water are constant)

Figure 10 shows the effect of water on workability with CEM I, CEM II and superplasticiser constant. The variation is about 35 cycles for 30 litres of water. Figure 11 shows the effect of superplasticiser on workability with CEM I, CEM II and water constant. The variation is about 16 cycles for 3% of superplasticiser.

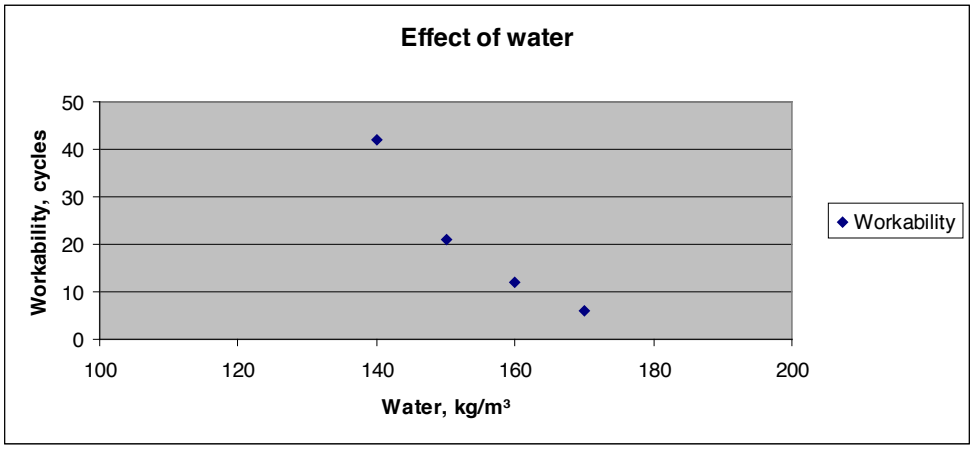

Figure 10 - Effect of water on workability (CEM I, CEM II and superplasticiser are constant)

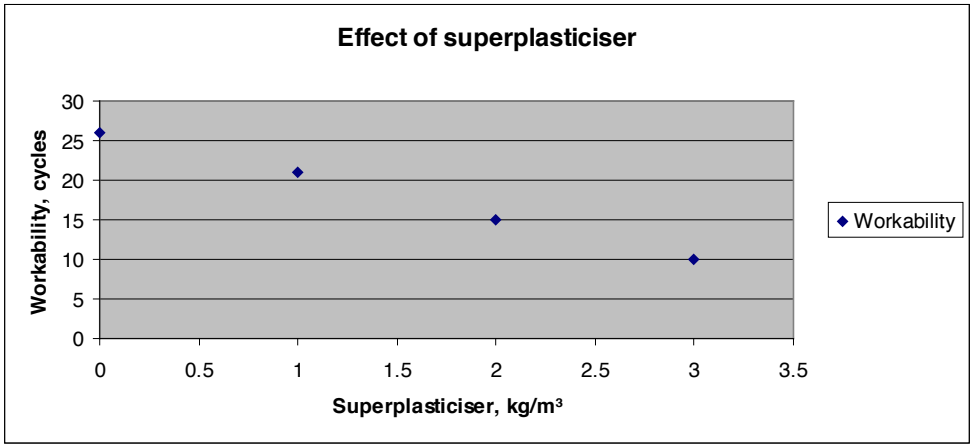

Figure 11 - Effect of superplasticiser on workability (CEM I, CEM II and water are constant)

4. RESULTS

Nonlinear models in the form of feed-forward neural networks were developed separately for workability, early strengths at 16 hours and 20 hours from the experimental data. Carbon dioxide emissions were estimated as a simple linear function of the amounts of CEM I and CEM II. Nonlinear model development and their characteristics are described in the sequel. The behaviour of the models and calculations based on the models are in section 4.4.

4.1. Workability

A large number of feed-forward neural network models were attempted using NLS 020 software. One or more weights in those neural networks were restricted. Most of the better models showed a high degree of correlation of about 98%, with a rms error of the order of 1. The nonlinear model selected for use had the following characteristics.

```
Output variable 1: Workability [cycles]

Training set: 24 observations

rms err     of output variable 1: 1.1523
mean |err|  of output variable 1: 0.8624
rms % err   of output variable 1: 6.1973
max |err|   of output variable 1: 3.4142
Correlation of output variable 1: 0.9784
```

Figure 12 shows a comparison of the measured values on the horizontal axis with the values predicted by the nonlinear model of workability. The lines parallel to the diagonal are at a horizontal distance of 1.1523 cycles, the rms error of prediction.

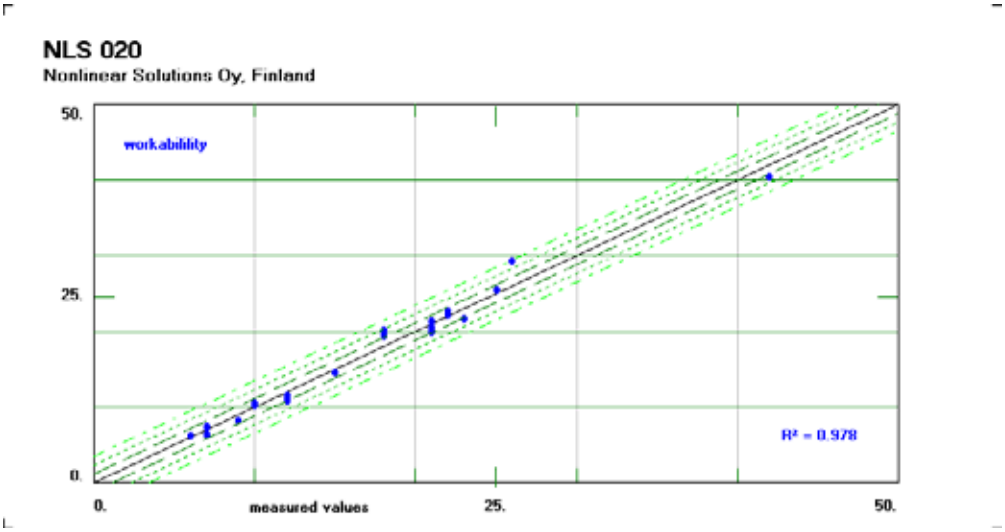

Figure 12 - A comparison of the measured values with the values predicted by the nonlinear model of workability in cycles

4.2. Early strength at 16 hours

A large number of feed-forward neural network models were attempted using NLS 020 software. One or more weights in those neural networks were restricted. Most of the better models showed a high degree of correlation of about 99%, with a rms error of the order of 0.4 MPa. The nonlinear model selected for use had the following characteristics.

```
Output variable 2: 16 hour strength [MPa]

Training set: 24 observations

rms err      of output variable 2: 0.4060
mean |err|   of output variable 2: 0.3203
rms % err    of output variable 2: 1.3495
max |err|    of output variable 2: 1.1654
Correlation of output variable 2: 0.9946
```

Figure 13 shows a comparison of the measured values on the horizontal axis with the values predicted by the nonlinear model of 16 hour strength.

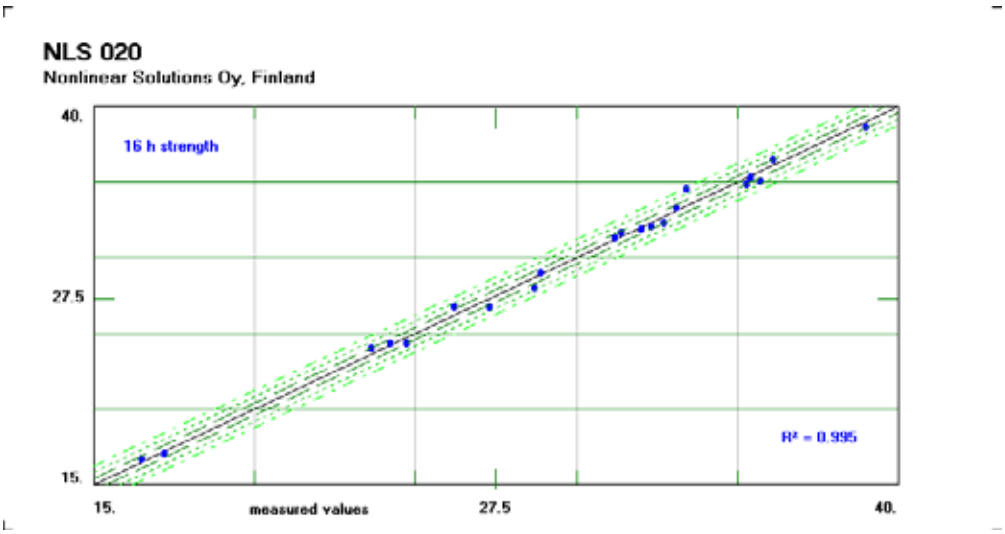

Figure 13 - A comparison of the measured values with the values predicted by the nonlinear model of 16 hour strength in MPa

4.2. Early strength at 20 hours

A large number of feed-forward neural network models were attempted using NLS 020 software. One or more weights in those neural networks were restricted. Most of the better models showed a high degree of correlation of well above 99%, with a rms error of the order of 0.25 MPa. The nonlinear model selected for use had the following characteristics.

```
Output variable 3: 20 hour strength [MPa]

Training set: 24 observations

rms err     of output variable 3: 0.2525
mean |err|  of output variable 3: 0.1931
rms % err   of output variable 3: 0.7668
max |err|   of output variable 3: 0.7072
Correlation of output variable 3: 0.9974
```

Figure 14 shows a comparison of the measured values on the horizontal axis with the values predicted by the nonlinear model of 20 hour strength.

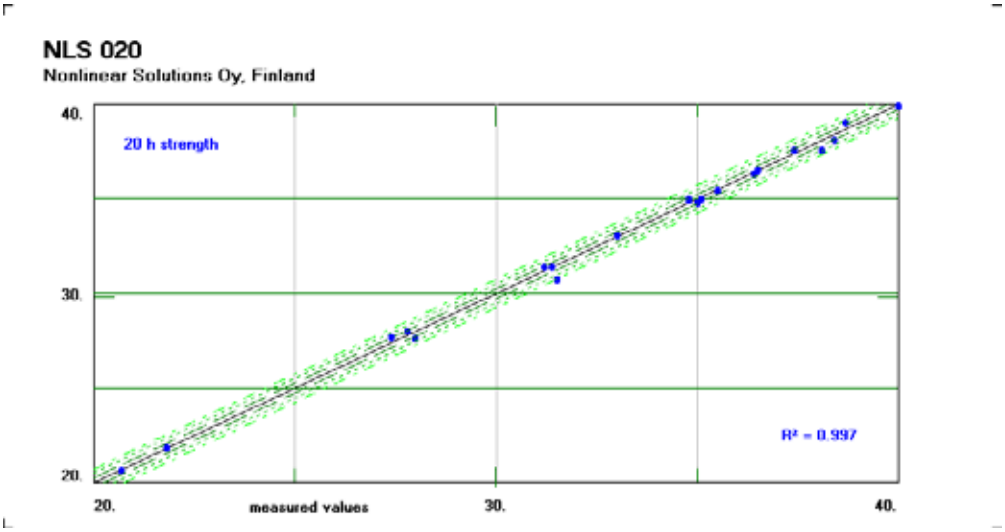

Figure 14 - A comparison of the measured values with the values predicted by the nonlinear model of 20 hour strength in MPa

4.4. Implementation of the models

In order to be able to determine good recipes which minimise carbon dioxide emissions while keeping workability and early strengths in desired limits, the nonlinear models for workability and early strengths need to be combined with the model for predicting carbon dioxide emissions. The models were therefore implemented in a software system which allows the user to predict the strengths, workability and carbon dioxide emissions. One equation for calculating the raw material cost of cements and superplasticiser was also included. Figure 15 shows a typical calculation where the user has fed in amounts of CEM I, CEM II, water and superplasticiser, and the models were used to calculate the numbers on the right.

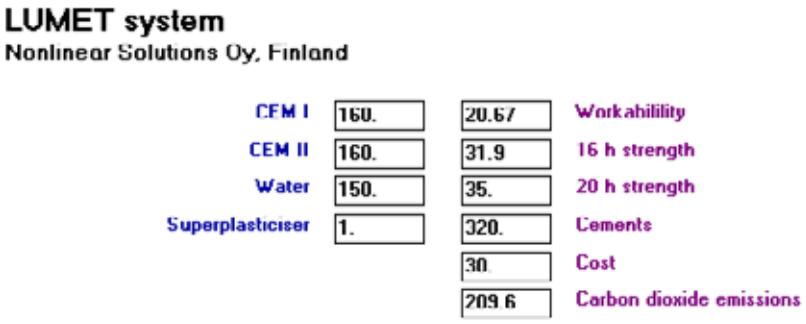

Figure 15 – A typical calculation using the nonlinear models

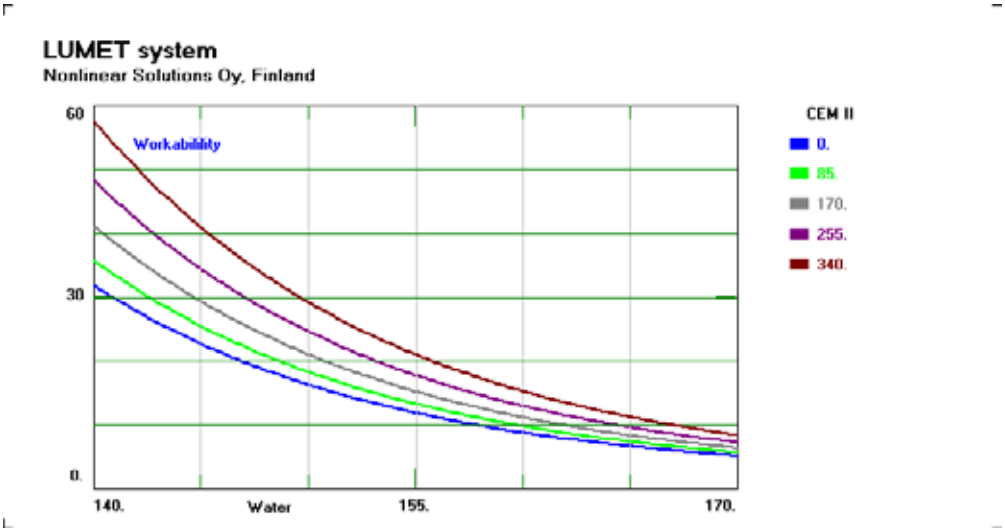

Figure 16 – Effect of water on workability for different amounts of CEM II, while keeping the amounts of CEM I and superplasticiser constant

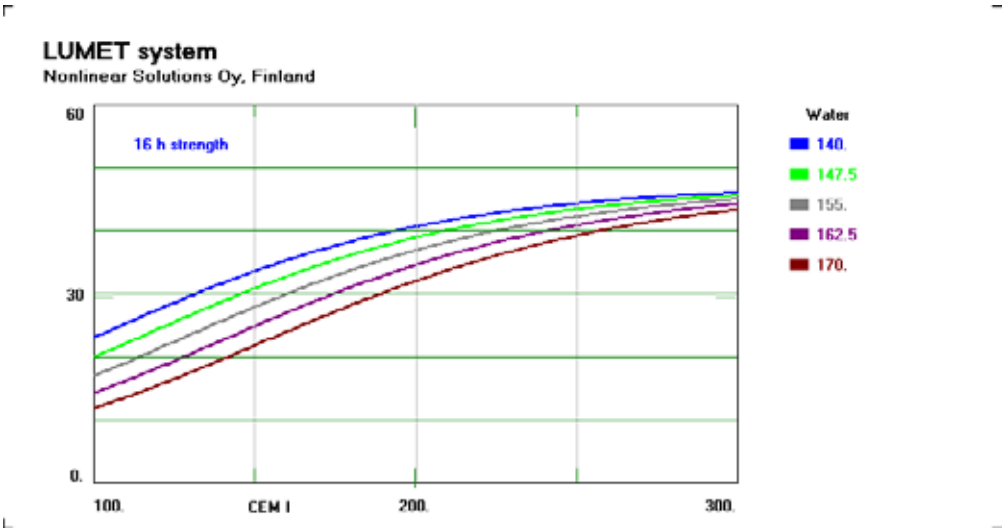

Figure 17 – Effect of CEM I on 16 hour strength for different amounts of water, while keeping the amounts of CEM II and superplasticiser constant

Figure 16 shows the effect of water on workability for different amounts of CEM II, while keeping the amounts of CEM I and superplasticiser constant. The effects are obvious. Increasing water or reducing the amount of cement improves the workability. Figure 17 shows the effect of CEM I on 16 hour strength for different amounts of water, while keeping the amounts of CEM II and superplasticiser constant. The strength curves increase faster in the beginning and then tend to flatten out. The nonlinear model, however, is not expected to be reliable when the total

amount of cements is much higher than 340 kg or much lower than 285 kg. Similarly, Figure 18 shows the effect of CEM I on 20 hour strength for different amounts of water, while keeping the amounts of CEM II and superplasticiser constant. The effects are qualitatively similar, but the total variation in 20 hour strength is smaller than the variation for 16 hour strength.

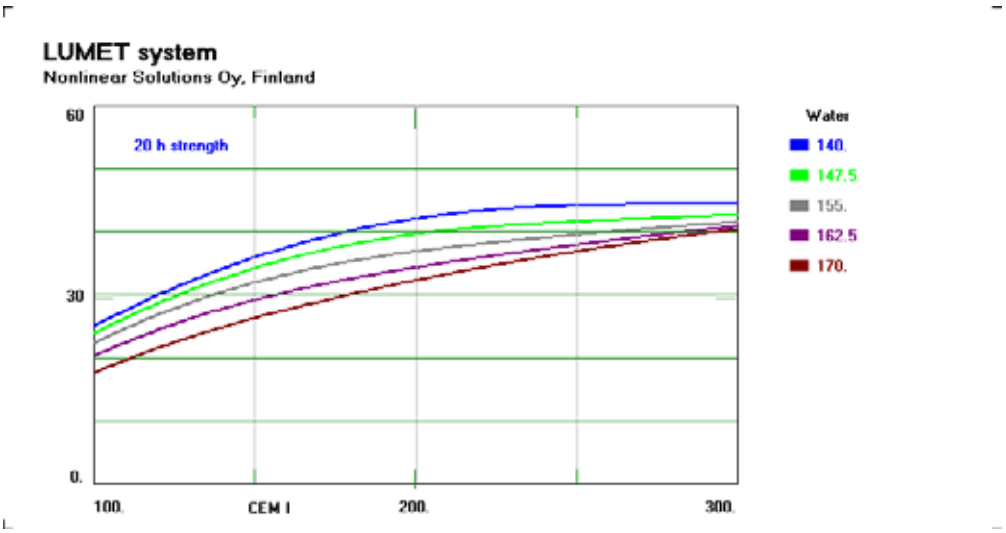

Figure 18 – Effect of CEM I on 20 hour strength for different amounts of water, while keeping the amounts of CEM II and superplasticiser constant

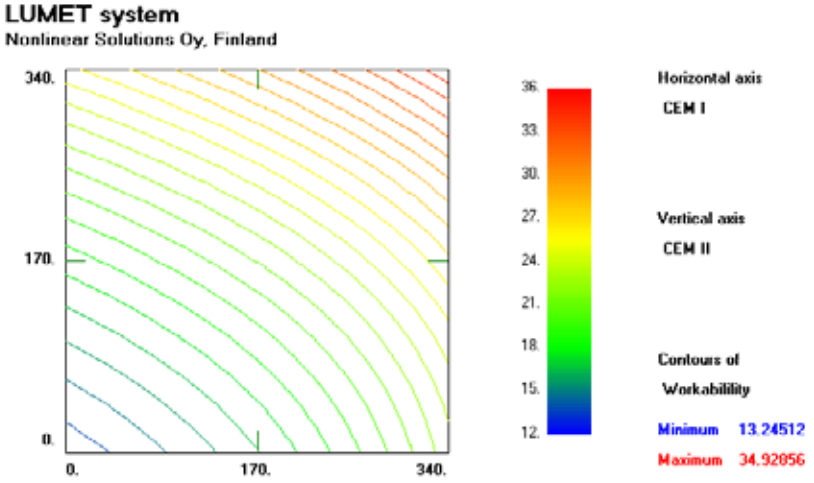

Figure 19 – Effect of CEM I and CEM II on workability in the form of contours, while keeping the amounts of water and superplasticiser constant

Figure 19 shows the effect of CEM I and CEM II on workability in the form of contours, while keeping the amounts of water and superplasticiser constant. Figure 20 shows the effect of CEM I and water on 16 hour strength in the form of contours, while keeping the amounts of CEM II and superplasticiser constant.

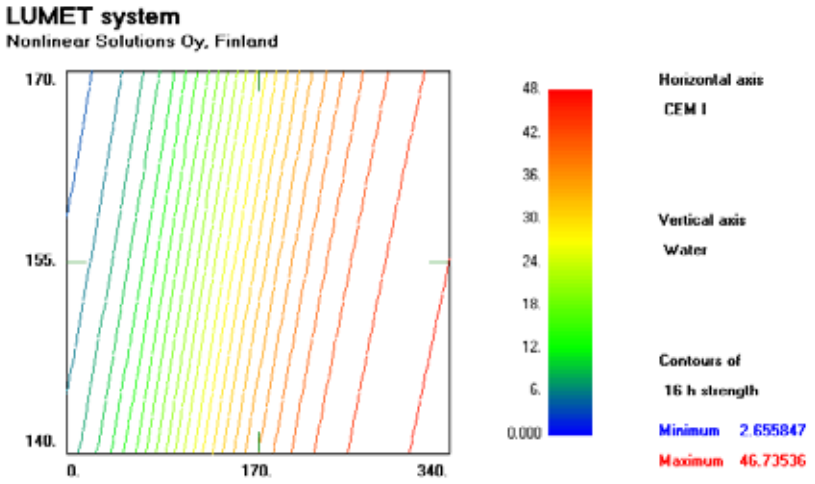

Figure 20 – Effect of CEM I and water on 16 hour strength in the form of contours, while keeping the amounts of CEM II and superplasticiser constant

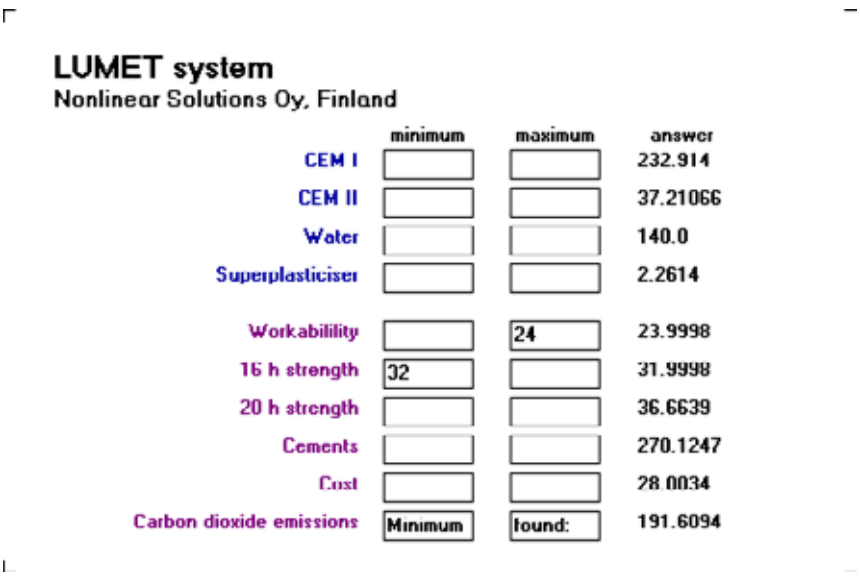

Figure 21 – A carbon dioxide emission minimisation calculation in presence of constraints on workability and early strength

The main objective of this work was to be able to determine recipes with minimum carbon dioxide emissions. Without any constraints on strength or workability, the optimal composition would not use any cement at all. With a lower limit on early strength, cement becomes necessary, which necessitates water, and then the upper and lower limits on workability makes this a more complicated issue. Figure 21 shows a calculation for minimising carbon dioxide emissions with a minimum 16 hour strength of 32 MPa and a maximum of 24 cycles for workability. The calculated solution uses a large amount of CEM I and a small amount of CEM II. The cost per cubic metre of concrete is also lower than the one calculated in Figure 15. Different limits on early strength and workability result in different optimal recipes.

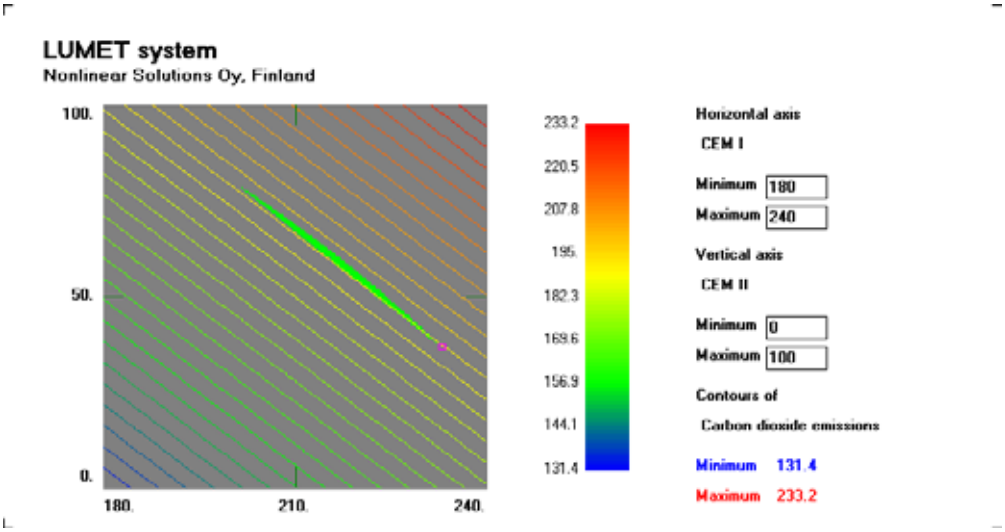

Figure 22 – Determination of a range of compositions with given limits on one or more variables

The green region in Figure 22 shows the range of solutions to the problem of getting a workability below 24 cycles and a 16 hour strength above 32 MPa, for fixed values of water (140 litres) and superplasticiser (2.2614 kg). The contours shown in the figure are for carbon dioxide emissions which are straight lines ranging from 131.4 kg to 233.2 kg. The little square at the lower end of the green region shows the solution for minimum carbon dioxide emissions.

This example once again demonstrated how nonlinear modelling is a powerful way of determining optimal recipes with constraints on workability and early strength. The objective in this case was to minimise carbon dioxide emissions. The nonlinear modelling approach is generally applicable to practically all kinds of materials. Different materials will have different composition variables, and the desired properties will have different constraints and objectives. The same approach, however, can be used and has been successfully used for materials including plastics, elastomers, metals, ceramics, semiconductors, paper, etc. This approach is far more reliable than physical models which require plenty of assumptions and simplifications. In most cases, it is not possible to predict material properties using physical models, which tend to be particularly suitable for academic consumption. Empirical and semi-empirical modelling is based on observations and simply describes the reality as observed. The limitation of the

approach is that the models so developed will not be applicable in general, and for each set of raw materials, a moderately small series of experiments will be required.

This example also demonstrated how CEM II may not be as environment friendly as is usually expected. Under some constraints, the optimal recipes will not use CEM II at all. In other words, if carbon dioxide emissions are to be minimised, the solution might be to use more CEM I than what common sense would suggest.

5. CONCLUSIONS

Environmental issues are becoming more important in concrete industries, and there is a concern for carbon dioxide emissions. This work focussed on determining the minimum carbon dioxide emissions in one case of no slump concrete with two cements. CEM II may not harden as fast, depending on its composition. Thus increasing the proportion of CEM II is not a solution if a certain early strength is needed. Early strength can be achieved by reducing water, but that could adversely affect the workability. Therefore the whole picture has to be kept in mind while trying to minimise carbon dioxide emissions. Without any constraints, the result would not use any cement at all. With a lower limit on early strength, cement becomes necessary, which necessitates water, and then the upper limit on workability in terms of cycles makes this a more complicated issue.

To be able to calculate the minimum carbon dioxide emissions with constraints on workability and early strength, models are needed for workability and early strength besides carbon dioxide emissions. The model for carbon dioxide emissions is a simple linear equation involving the two cements, but the relations between workability and the composition variables of concrete are not simple. Nonlinear models were therefore developed for workability and early strength from a modest amount of experimental data. The models showed a very high degree of correlation. They were then implemented in suitable software which made it easy to calculate the minimum carbon dioxide emissions. The minimum usually requires smaller amounts of CEM II for different limits on workability and strength.

REFERENCES

1. Ali Hasanbeigi, Lynn Price, Elina Lin, “Emerging energy-efficiency and CO2 emission-reduction technologies for cement and concrete production: A technical review”, Renewable and Sustainable Energy Reviews, Volume 16, Issue 8, October 2012, 6220-6238
2. Mukesh Limbachiya, Sevket Can Bostanci, Hsein Kew, “Suitability of BS EN 197-1 CEM II and CEM V cement for production of low carbon concrete”, Construction and Building Materials, Volume 71, 30 November 2014, 397-405
3. M. B. Ali, R. Saidur, M. S. Hossain, “A review on emission analysis in cement industries”, Renewable and Sustainable Energy Reviews, Volume 15, Issue 5, June 2011, 2252-2261
4. Wikipedia, http://en.wikipedia.org/wiki/Environmental_impact_of_concrete
5. A. Petek Gursel, Eric Masanet, Arpad Horvath, Alex Stadel, “Life-cycle inventory analysis of concrete production: A critical review”, Cement and Concrete Composites, Volume 51, August 2014, 38-48
6. Phil Purnell and Leon Black, “Embodied carbon dioxide in concrete: Variation with common mix design parameters”, Cement and Concrete Research, Volume 42, Issue 6, June 2012, Pages 874-877

7. K. Hornik, M. Stinchcombe, and H. White, “Multilayer feed forward networks are universal approximators,” Neural Networks, Vol. 2, (1989) 359-366.
8. A. Bulsari (ed.), Neural Networks for Chemical Engineers, Elsevier, Amsterdam, Netherlands, 1995.
9. A. Bulsari, “Quality of nonlinear models in process industries”, Internal Report NLS/1998/2.
10. Abhay Bulsari, Kimmo Lähteenkorva, Esa Suokas and Mikko Huttunen, “Models add efficiency to bioabsorbable implant development”, Medical Design Technology, Vol. 19, No. 2 (March 2015) 26-28
11. A. Bulsari et al., ”Nonlinear modelling paves the way to bespoke polymers”, British Plastics and Rubber, December 2002, 4-5.
12. A. Bulsari, J. Fredriksson and T. Lehtinen, “Neural networks for quality control in the wire rod industry”, Wire Industry, Vol. 67 (March 2000) 253-258.
13. Abhay Bulsari, Harri Kylmämetsä and Klaus Juvas, ”Nonlinear models of workability and compressive strength help minimise costs”, Concrete Plant International, No. 6 (December 2009) 36-42
14. A. Bulsari, H. Keife and J. Geluk, “Nonlinear models provide better control of annealed brass strip microstructure”, Advanced Materials and Processes, Vol. 170, No. 7 (July 2012) 18-20
15. A. Bulsari and M. Lahti, “How nonlinear models help improve the production economics of extrusion processes”, British Plastics and Rubber (September 2008) 30-32
16. Abhay Bulsari, Esa Lindell, Rauno Luoma and Tuomo Laukkanen, ”How nonlinear modelling improved understanding of a hydrometallurgical leaching process”, Engineering and Mining Journal (September 2012) 84-90
17. A. Bulsari and M. Lahti, “Nonlinear models guide secondary coating of OFCs”, Wire and Cable Technology International, Vol. 29, No. 5 (September 2001) 40-43
18. A. Bulsari and P. Hooli, “More accurate alloying with neural networks”, Stainless Steel World, Vol. 12 (November 2000) 54-57.

Properties of Fresh Macro Basalt Fibre (MiniBar) Self-Compacting Concrete (SCC) and Conventional Slump Concrete (CSC) Aimed for Marine Applications

Ali Mohammadi Mohaghegh
PhD Candidate
Ålesund University Collage
P. O. Box 1517, N-6025 Ålesund
Corresponding author: almo@hials.no
ali.mohaghegh@byv.kth.se

Johan Silfwerbrand
Professor
Department of Civil and Architectural Engineering
KTH Royal Institute of Technology,
SE 100 44 Stockholm

Vemund Årskog
Associate Professor
Ålesund University College
P. O. Box 1517,
N-6025 Ålesund

ABSTRACT

Macro basalt fibres (MiniBar) with high corrosion resistance could be a suitable material in fibre concrete for marine applications. Due to the lack of knowledge about macro basalt fibre concretes (BFCs), the main objective of this paper is to assess the fresh state properties of macro basalt fibre conventional slump concrete and self-compacting concrete as the first step of developing BFC for concrete barges for fish farming on the west coast of Norway. To satisfy the requirements for marine applications, DNV and NS-EN standard rules are employed as the basis for the durability performance design. The concrete mix is designed to achieve densely compacted matrix by using the modified Andreasen & Andersen model as the particle size distribution target. In this paper, slump, flow-ability, passing-ability, fibre dynamic segregation and also flow rate as an indication for viscosity of different BFCs are measured and analysed. The result shows that there is a possibility to produce BF-SCCs with a fibre content of 1.15%. The fibres have an aspect ratio of 65.15. In addition, the mixture composed of a maximum gravel size of 16 mm shows a higher flowability in comparison with the maximum gravel size of 12 mm.

Keywords: Macro Basalt Fibre, Self-Compacting Concrete, Marine Application, Particle Packing Model

1. INTRODUCTION

Reinforcement corrosion in the harsh environment of the Norwegian west coast is one of the main challenges in design and construction of concrete marine structures [1]. To solve this problem, using a corrosion resistance material could lead to more durable and environmental friendly structures [1]. Macro basalt fibres (MiniBars) in combination with basalt fibre reinforced polymer (BFRP) rebars with high strength, high corrosion resistance and low density as a hybrid system could be a suitable alternative to the steel reinforcement [1].

By using fibres in concrete, depending on different parameters such as maximum aggregate size, fibre volume fraction, fibre type, fibre geometry and fibre aspect ratio, workability of the concrete is reduced [2]. Reduction of workability in the fibre concrete is a serious challenge in construction sites [2]. The major advantage of the synergy between self-compacting concrete and fibres is the achievement of a more uniform dispersion of the fibres by elimination of vibration and compaction [2, 3]. Improper compaction, may cause a random dispersion of fibres and produce regions with lower fibre dosage or even no fibres at all. This could lead to unpredictable mechanisms that negatively affect the load-bearing capacity and other mechanical properties of the whole structure [3]. Improvement of economic efficiency in the construction process by increasing the construction speed, reduction of the labour cost and energy consumption and also a better working environment by reduced noise and health hazards are some of the advantages of using SCC [4]. Also, substituting the conventional reinforcement with fibres could lead to an automated construction system with higher reliability in quality control [4].

Durability of concrete and reinforcement is one of the key parameters in the design of marine concrete structures. Durability of concrete can be quantified by using permeation properties including oxygen permeability, chloride diffusivity, capillarity absorption etc. [5].

Zhu et al. [5] showed that the permeation properties of different SCCs are very dependent on the composition of the mixture. As an example, using viscosity modifier agent as a substitution for filler will considerably increase the oxygen permeability and chloride migration coefficient of the concrete [5]. Also in their studies, significant lower oxygen permeability and capillarity water absorption were observed for the SCC mixes in comparison with CSC [5]. Limited microstructural studies showed that the SCC has a denser interfacial zone around larger aggregates and reinforcements with more homogeneous properties than vibrated CSC [5]. It means less porous interfacial zone that might be a possible proof for the better permeation properties of SCC [5].

Kaasgaard et al. [6] performed an investigation pertaining to durability parameters of SCC in comparison with CSC for three different compositions. These concretes were exposed to marine condition, and showed that the strength development, chloride migration coefficients and frost resistance of SCC were similar to the ones of CSC with corresponding binder.

To satisfy the required properties for durability of concrete structures in marine environment, available standards shall be applied during the design and construction process. In this study the relevant requirements of offshore concrete structures-DNV-OS-C502 [7] and the standard for concrete specification, performance, production and conformity NS-EN 206-1 [8] are chosen as the basis for concrete mixture design. The exposure classes, maximum $\left(\frac{Water}{Binder}\right)$ ratio etc. is summarised in Figure 1. For concrete barges, depending on the position of structural elements, the exposure class of XS2 or XS3 shall be used. The limitation for the fibre volume content (2%) probably is related to the fibre distribution properties, but in the case of using macro basalt

fibres thanks to its closer density to fresh concrete, there is a possibility to use higher fibre volume fraction.

Patnaik [9] tested CSCs with a volume fraction of macro basalt fibres up to 4%. The maximum aggregate size was 20 mm. The average cylindrical compressive strength was 68.3 MPa and the flexural tensile strength 15.74 MPa [9]. In this study, we limited the maximum fibre content to 2% for both SCC and CSC.

Based on Matrix-Particle (MP) model, both SCC and CSC could be defined as dual phase materials [10]. The matrix phase is defined as a fluid material consisting of water, chemical additives, cement, silica, fly ash and other fine materials with a particle size smaller or equal to 125 µm [11]. The particle phase defined as aggregates with the size of more than 125 µm and also fibres in the case of fibre concrete, see Figure 2 [11]. High performance concrete and self-compacting concrete have a higher volume content of matrix and lower $\left(\frac{Water}{Binder}\right)$, therefore they can be assumed as matrix dominated materials [11]. In a matrix dominated concrete selecting of a dense particle distribution, reduces the contact and friction between particles by a layer of matrix surrounding the aggregates [11]. Additionally, a densely compacted cementations matrix is a key for a high performance and durable concrete [12].

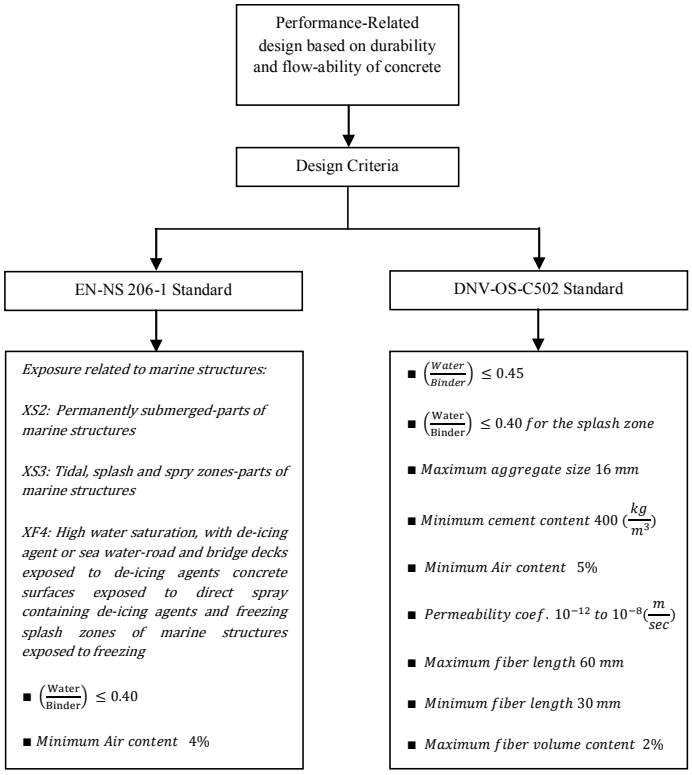

Figure 1 - Criteria for mixture design of marine self-compacting fibre concrete according to the DNV-OS-C502 and NS-EN 206-1. After [7, 8].

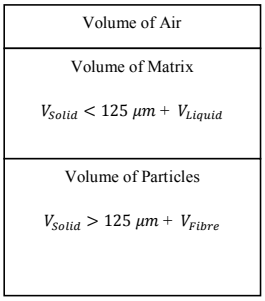

Figure 2 - Scheme of fibre concrete based on Matrix-Particle model.

By using the particle packing optimization, it is possible to select the right size and volume fraction of solid ingredients in the concrete [13]. There are three different approaches for particle optimization; optimization curve, particle packing models and discrete element models [13].

Based on Fuller-Thompson and Andreasen & Andersen studies, a dense concrete composition can theoretically be achieved by an optimal particle size distribution (PSD) of all concrete solid ingredients in the mix [12, 14]. Equation (1) shows the optimal PSD, where *P (D)* is a fraction of particles smaller than size *D* (μm), $D_{\max}$ is the maximum particle size (μm) and q is the distribution modulus [12].

$$P(D) = \left(\frac{D}{D_{\max}}\right)^q \quad (1)$$

Funk and Dinger modified Equation (1) to consider the effect of the smallest particle size in the equation. Equation (2) shows the modified Andreasen & Andersen (A&A) packing model [12, 14].

$$P(D) = \frac{D^q - D_{\min}^q}{D_{\max}^q - D_{\min}^q} \quad (2)$$

where $D_{\min}$ is the minimum particle size (μm)

Brouwers findings showed that an optimal particle packing theoretically can be achieved by applying a q value of 0-0.28, and Brouwers and Radix showed that q=0.25 is the most relevant value to achieve the actual distribution for the solids including cement and silica in SCC composition where $D_{\min}$= *0.5* μm [12, 4]. According to the Huger recommendation, using a q value in the range of 0.22-0.25 would result in an optimal PSD for SCC [12]. Lower q values give a better performance for fine and ultra-fine particle sizes by providing their proper size distribution [4]. Figure 3 (a & b) shows the modified A&A curves for two different maximum particle sizes of 12 mm and 16 mm, respectively. The presented graphs have a q value of 0.25 with different assumption for minimum particle sizes. 0.5 μm, 63 μm and 125 μm are selected based on the size of finest cement particles, smallest sieve size in PSD experiment and the maximum particle size of matrix in the MP model.

In the literature different methods for incorporating the effect of fibers in the packing models are presented, but to our knowledge no results that have been experimentally verified, pertaining to Basalt Marco Fibres have been published. Therefore, the effect of fibers in the packing model have not been considered in this study.

The focus of this study is the assessment of the fresh state behaviour of macro basalt fibre concrete, designed based on the absolute volume method and the modified A&A particle packing model. Based on the results of durability studies on three powder concretes, fly ash cement and silica are used as the main ingredients for the cementitious matrix. To investigate the effect of maximum aggregate size on the mixture properties of fresh concrete, gravel sizes of 16 mm and 12 mm are selected according to the local accessibility. EN-NS experimental procedures [21, 22] are used for evaluation of mixtures properties.

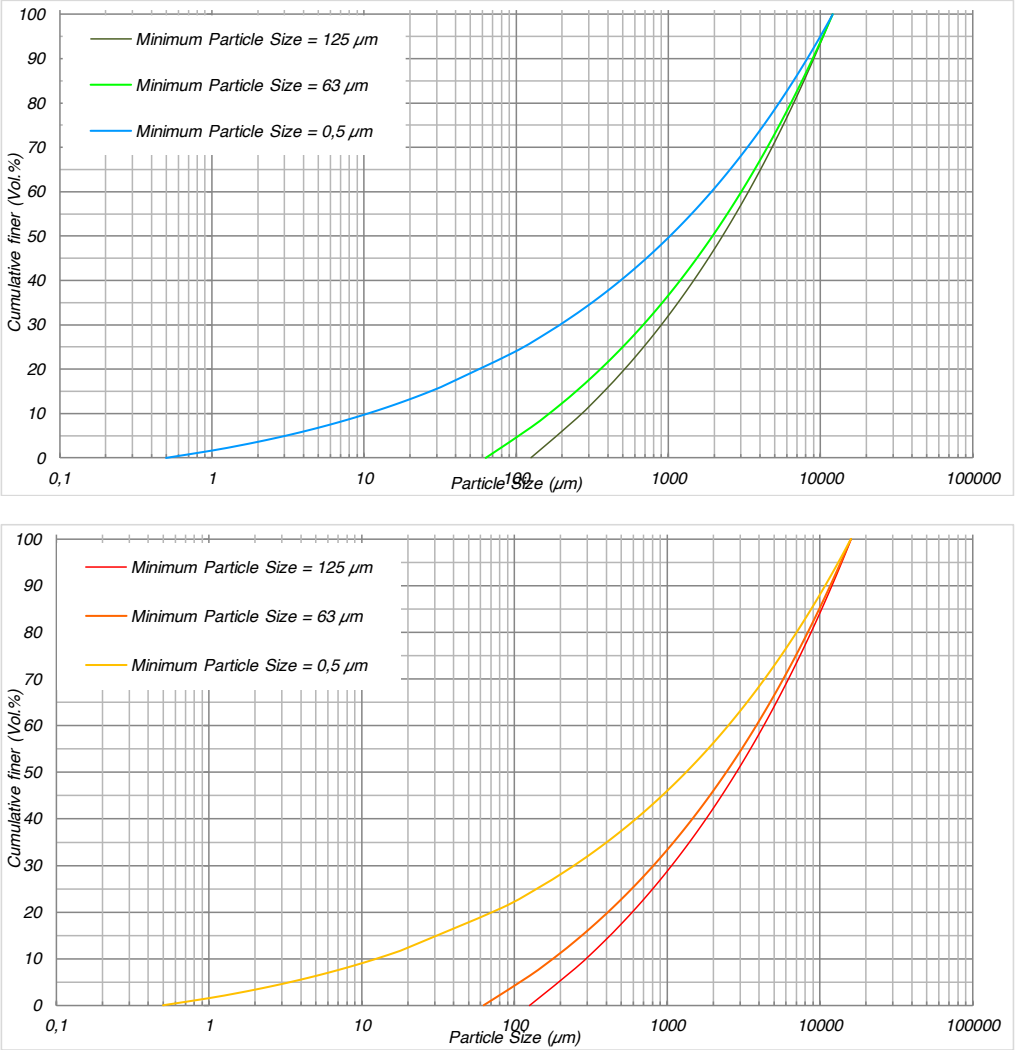

Figure 3 - Particle size distribution (PSD) based on modified Andreasen & Andersen for the maximum aggregate size of 12 mm (a) and 16 mm (b).

2. MATERIALS AND METHODS

2.1 Materials

As is mentioned in the introduction, a new macro fibre made of basalt fiber reinforced polymer (BFRP) with the commercial name of MiniBar is used for producing the fibre concrete. Based on producer's technical data, to improve the bonding mechanism, MiniBar is designed with a straight shape with helix and rough surface. MiniBars have an average diameter of 0.66 mm, length of 43 mm [9] and $\frac{l_f}{d_f} = 65.15$, see Figure 4.

Figure 4 - Geometry of MiniBars; the length of the fibres is around 43 mm, [1].

Norwegian "Anleggsement" FA is used for this study, which satisfies the requirements of Portland EN 197-1-CEM II / A-V 42.5 N, additionally it is especially designed for Norwegian durability class of M45, MF45 or stricter by Norcem [15].The Anleggsement FA contains 17% of fly ash and to increase its resistance against alkali-silica reaction, the alkali content is 0.6% of the clinker portion [15]. Commercial micro silica produced by FESIL is used as a pozzolanic material. According to NS-EN 206-1, maximum volume percentage of silica is limited to 11% of cement content [8]. To fulfil the requirements for flow-ability, stability and frost resistance; Poly carboxylate ether based superplasticizer, viscosity modifying agent and air entraining agent, provided by MAPEI used in the concrete mixture [16, 17, 18]. As for the aggregates including gravel, sand and filler; crushed granite stone from similar local source is used. To study the effect of aggregate size, 12 mm and 16 mm gravels are used as the maximum aggregate size in different mixtures. To characterise the particle distribution properties of aggregates, EN-NS 933-1:2012 standard for sieving test is employed. Figure 5 shows the size distribution of solid particles that are used in composition of tested concrete. Cement and silica were characterised by laser diffraction method for the wet suspension [16]. To assess a higher precision in measurement of particle size distribution, sieving is repeated again after rinsing the aggregates. Table 1 shows the comparison between fine particle content of aggregates before and after rinsing.

Table 1 - Cumulative distribution of particles finer than 125 µm before and after rinsing.

Particle Size	Gravel 8-16 mm	Rinsed Gravel 8-16 mm	Gravel 8-12 mm	Rinsed Gravel 8-12 mm
Smaller than 125 µm (%)	1.67	2.71	0.54	0.74
Smaller than 63 µm (%)	1.06	1.79	0.30	0.52

Particle Size	Sand 0-8 mm	Rinsed Sand 0-8 mm	Filler 0-4 mm	Rinsed Filler 0-4 mm
Smaller than 125 µm (%)	8.25	8.52	19.95	21.26
Smaller than 63 µm (%)	2.58	2.84	9.89	12.28

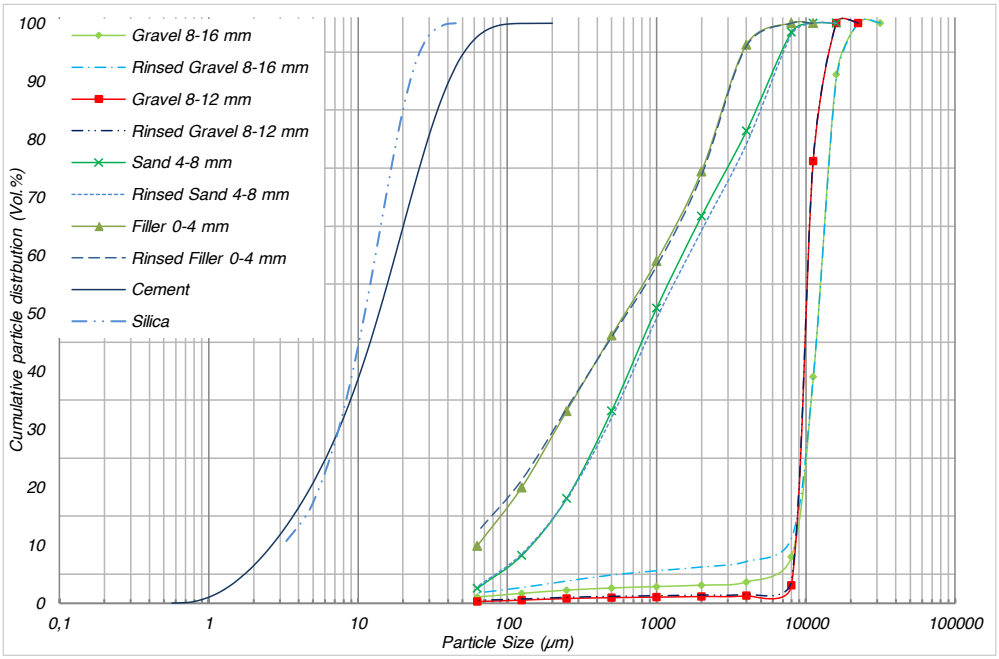

Figure 5 - PSDs of the involved ingredients including; cement, silica, gravel, sand and filler.

As it can be seen in Table 1, sieve test results show a higher fine particle content for rinsed aggregates; it shows that the surface of larger aggregates is covered by a portion of fine particles which are not actively incorporated in the composition of matrix. Therefore in calculation related to the mix design, the results of sieve test before rinsing shall be used. The detailed information of concrete ingredients including the densities is summarised in Table 2.

Table 2 - Material densities, commercial names and producers for the concrete ingredients.

Materials	Commercial Name	Producer	Density (kg/m^3)	
Macro Basalt Fibre	MiniBar 3.1Gen.	Reforcetech As	1900	[9]
Cement	Anleggsement FA	Norcem As	2990	[15]
Silica	Micro Silica	FESIL As	2300-2400	[16]
Superplasticizer	Dynamon SX-N	MAPEI As	1060 ± 20	[17]
Viscosity modifier	Viscofluid SCC/10	MAPEI As	1020 ± 20	[18]
Air entraining agent	Mapeair25 (1:5)	MAPEI As	1000 ± 20	[19]
Filler (0-4mm)	_____	Ulstein Betong AS	2660	
Sand (0-8mm)	_____	Standal Knuseverk AS	2710	
Gravel (8-12mm)	_____	Standal Knuseverk AS	2760	
Gravel (8-16mm)	_____	Standal Knuseverk AS	2770	

2.2 Experimental methods

Mix design of BF-SCC and BF-CSC

Absolute volume method is employed for proportioning of ingredients for both types of concrete. To satisfy the durability requirements for marine applications, 0.40 is used as the maximum $\left(\frac{Water}{Binder}\right)$ ratio based on the criteria summarized in Figure 1. The modified A&A particle packing model with q factor of 0.25 is used as the target for determination of the aggregate particle size distribution. As it is mentioned earlier, fibres are not incorporated in optimization process of particle size distribution by using equivalent particle size methods. Because $\left(\frac{Water}{Binder}\right)$ ratio is the main criterion for determination of binders, cement or silica particle sizes are not considered as the minimum particle size, therefor based on the precision of sieve test method $D_{\min}$ assumed to be 63 µm. Superplasticizer (SP), viscosity modifying agent (VMA) and air entraining agent (AEA) are used as the additives. The procedure of mixture design is summarized in Figure 6.

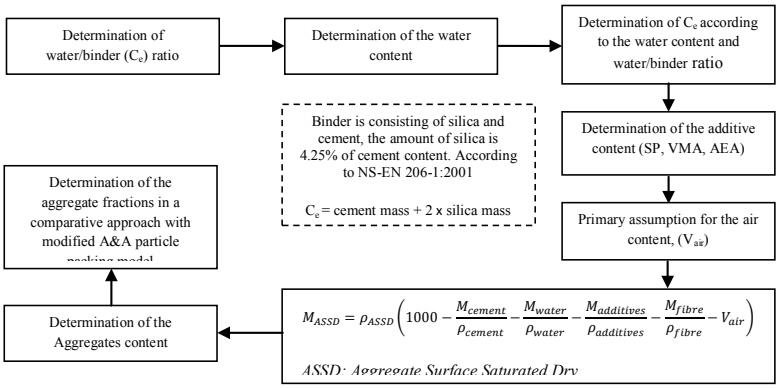

Figure 6 - Employed design procedure for BF-SCC.

Table 3 and 4 show the developed BF-SCC and BF-CSC mixtures based on the modified A&A model, respectively. In this experimental study, in total, two types of reference self-compacting concrete, for the maximum aggregate size of 16 mm and one reference mixture for the maximum aggregate size of 12 mm were used.

Table 3 - Composition of the designed basalt fibre self-compacting concretes (SCC).

Concrete Ingredients	BF-SCC A1 (kg/m^3)	BF-SCC A2 (kg/m^3)	BF-SCC A3 (kg/m^3)	BF-SCC B1 (kg/m^3)	BF-SCC B2 (kg/m^3)
Fibre VF (%)	0	0.25	0.50	0	0.75
MiniBar	0	4.75	9.50	0	14.25
Cement	421.66	421.66	421.66	421.66	421.66
Silica	17.92	17.92	17.92	17.92	17.92
C_e	457.50	457.50	457.50	457.50	457.50
Superplasticizer	10.79	10.79	10.79	11.87	11.87
Viscosity modifier	8.83	8.83	8.82	8.83	8.81
Air entraining agent	1.90	1.90	1.90	1.90	1.90
Filler (0-4 mm)	173.72	173.03	172.35	173.44	171.39
Sand (0-8 mm)	1078.82	1074.58	1070.35	1077.09	1064.39
Gravel (8-12 mm)	0	0	0	0	0
Gravel (8-16 mm)	462.06	460.25	458.43	461.32	455.88
(Water/C_e)	0.40	0.40	0.40	0.40	0.40
(Liquid content/C_e)	0.447	0.447	0.447	0.449	0.449
Water	183	183	183	183	183

Table 3 - Continued

Concrete Ingredients	BF-SCC B3 (kg/m^3)	BF-SCC B4 (kg/m^3)	BF-SCC C1 (kg/m^3)	BF-SCC C2 (kg/m^3)	BF-SCC C3 (kg/m^3)
Fibre VF (%)	1	1.15	0	0.50	1
MiniBar	19	21.85	0	9.50	19
Cement	421.66	421.66	421.66	421.66	421.66
Silica	17.92	17.92	17.92	17.92	17.92
C_e	457.50	457.50	457.50	457.50	457.50
Superplasticizer	11.87	11.87	10.79	10.79	10.79
Viscosity modifier	8.80	8.80	8.91	8.89	8.88
Air entraining agent	1.90	1.90	1.90	1.90	1.90
Filler (0-4 mm)	170.71	170.30	187.71	186.14	184.59
Sand (0-8 mm)	1060.16	1057.62	1095.30	1086.11	1077.09
Gravel (8-12 mm)	0	0	460.37	456.51	452.71
Gravel (8-16 mm)	454.07	452.98	0	0	0
(Water/C_e)	0.40	0.40	0.40	0.40	0.40
(Liquid content /C_e)	0.449	0.449	0.447	0.447	0.447
Water	183	183	183	183	183

For the conventional slump concrete, one mixture is developed as the reference composition. In all mixtures except BF-SCC, C series, diluted air entraining agent with proportion of 1:5 was used. For BF-SCC, A, B and C series the content of superplasticizer was considered to be 2.5%, 2.75% and 2.5% of binder's content, respectively. For BF-CSC series, the content of superplasticizer was 1.5%. Figure 7 shows the particle packing of concrete mixes for both SCC and CSC. Hence, the concrete mixtures are composed of different proportion of ingredients; the graphs of aggregate mixtures are very similar to each other and also close to the target curve.

Table 4 - Composition of the designed basalt fibre conventional slump concretes (CSC).

Concrete Ingredients	BF-CSC 1 (kg/m^3)	BF-CSC 2 (kg/m^3)	BF-CSC 3 (kg/m^3)	BF-CSC 4 (kg/m^3)	BF-CSC5 (kg/m^3)	BF-CSC6 (kg/m^3)
Fibre VF (%)	0	0.50	1	1.25	1.5	2
MiniBar	0	9.50	19	23.75	28.5	38
Cement	421.66	421.66	421.66	421.66	421.66	421.66
Silica	17.92	17.92	17.92	17.92	17.92	17.92
C_e	457.5	457.5	457.5	457.5	457.5	457.5
Superplasticizer	6.47	6.47	6.47	6.47	6.47	6.47
Viscosity modifier	0	0	0	0	0	0
Air entraining agent	1.90	1.90	1.90	1.90	1.90	1.90
Filler (0-4 mm)	181.08	179.67	178.27	177.58	176.88	175.48
Sand (0-8 mm)	1124.50	1115.82	1107.13	1102.80	1098.46	1089.78
Gravel (8-12 mm)	0	0	0	0	0	0
Gravel (8-16 mm)	481.63	477.91	474.19	472.33	470.48	466.76
(Water/C_e)	0.40	0.40	0.40	0.40	0.40	0.40
(Liquid content /C_e)	0.415	0.415	0.415	0.415	0.415	0.415
Water	183	183	183	183	183	183

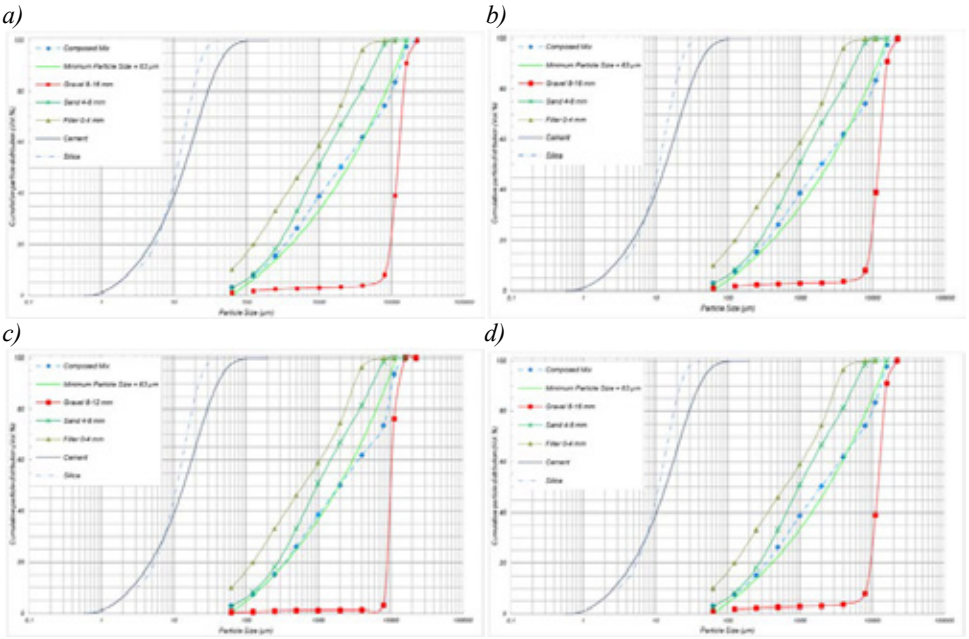

Figure 7 - PSDs of the ingredients, target curve (modified A&A curve for minimum particle size of 63 µm) and grading line of composed aggregates for the mixes BF-SCC A1 (a), BF-SCC B1 (b), BF-SCC C1 (c), BF-CSC 1 (d).

Employed mixing procedure

In this study, rather simple method is utilized to mix the BF-SCC and BF-CSC. Obtaining the full effect of superplasticizer in higher volume content, for increasing the flowability is a time

consuming process. Therefore, longer mixing time is required for the final production. Figure 8, shows the sequence of mixing process. Depending on the type of mixer, extra mixing time in higher fibre content could damage the fibres. Therefore fibres shall be added in the end of process, see Figure 9. The detailed information of the mixing procedure is shown in Table 5. All the experimental procedure including sample production is performed in the room temperature of approximately 20 °C.

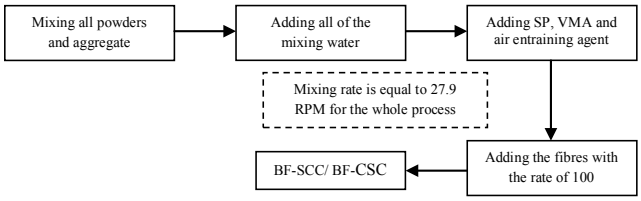

Figure 8 - Employed mixing procedure to produce BF-SCC and BF-CSC.

Figure 9 - In the left hand side, concrete with fiber content of 2.5% after 7 minutes of mixing is shown. Right hand side shows the broken fibres after extended mixing time.

Table 5 - Mixing procedure sequence.

Description of mixing procedure	Duration (minutes)
Dry mixing of all powders and aggregate fractions	1
Adding the water and mixing	1
Relaxing	1
Adding the superplasticizer (SP) and mixing	1
Relaxing	1
Mixing and adding the viscosity modifier agent (VMA) in the end of this step	1.5
Mixing (for SP content of less than three percent)	3.5-4.5
Mixing (for SP content of more than three percent)	5.5-6.5
Adding the air entraining agent and fibres (mixing will be continued 1 minute after adding the whole fibres)	
Σ =	11-14

Flowability and passing-ability of BF-SCC

Flowability defined as the ease of flow of fresh SCC in the formwork and the passing-ability is the capacity of fresh SCC to flow through tight openings such as spaces between steel reinforcing bars without losing the uniformity, segregation and blocking [20]. In this study slump-flow test is performed according to NS-EN12350-8:2010 [21] to access flow rate and flowability of SCC. Slump flow is calculated with Equation (3)

$$SF = \frac{(d_1 + d_2)}{2} \quad (3)$$

where, d_1 (mm) and d_2 (mm) are largest perpendicular diameters of flow spread.

Relative flow rate is measured by the time when concrete flow reaches to the diameter of 500 mm and is recognised as t_{500}.

Passing-ability of SCC is accessed by the J-ring test; in this study bar spacing is assumed to be (41±1) mm, the J-ring passing-ability is measured by the blocking step calculated using Equation (4) following NS-EN12350-12:2010 [22].

$$PJ = \frac{(\Delta h_{x1} + \Delta h_{x2} + \Delta h_{y1} + \Delta h_{y2})}{4} - \Delta h_{x0} \quad (4)$$

where, Δh are the measured heights (Δh_x and Δh_y are the measured heights of the J-ring and Δh_{x0} is the measured height in the middle of the ring)

Fibre dynamic segregation of BF-SCC
A fibre dynamic segregation can be defined as the gradient of the normalized fibre concentration versus normalized radial distance in a free flow condition [3]. In this study, a circle with the diameter of 300 mm in the centre of the flow is used as reference, and the fibre content is measured inside and outside of the reference area. For evaluation of fibre distribution the weight ratio in a constant volume is used as the normalized fibre concentration.

3. EXPERIMENTAL RESULTS AND DISCUSSION

3.1 BF-SCC performance

Flowability and passing-ability of BF-SCC
The reference BF-SCC mixtures are designed to have a minimum slump-flow of 750 mm. Performance of the fresh state concrete is evaluated by means of slump-flow and J-ring tests. The obtained results are summarized in Table 6. Figure 10 shows the slump-flow test of BF-SCC B1 and BF-SCC B4.

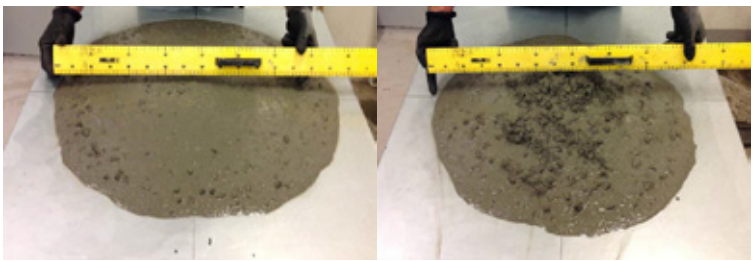

Figure 10 - In the left hand side, reference concrete without the fibre (BF-SCC B1) is shown. Right hand side shows the SCC with fibre content of 1.15% (BF-SCC B4).

The results of slump-flow and flow rate for the reference mixtures are slightly different. It shows a moderate sensitivity to the variation of SP and maximum aggregate size, but the difference is not that great.

Table 6 – Test results of reference SCCs and BF-SCCs.

Flow Characterization	BF-SCC A1	BF-SCC A2	BF-SCC A3	BF-SCC B1	BF-SCC B2
Fibre VF (%)	0	0.25	0.50	0	0.75
SF (mm)	780	755	710	775	735
T_{500} (s)	1.50	1.60	2.70	1.96	2.20
SFJ (mm)	770	680	595	730	575
PJ (mm)	6.75	27	38.50	6.25	49.25
TJ_{500} (s)	2.10	2.60	4.70	1.93	4.90

Table 6 - continued

Flow Characterization	BF-SCC B3	BF-SCC B4	BF-SCC C1	BF-SCC C2	BF-SCC C3
Fibre VF (%)	1	1.15	0	0.50	1
SF (mm)	710	690	790	780	680
T_{500} (s)	2.84	2.41	2.25	2.80	8.07
SFJ (mm)	545	560	750	610	550
PJ (mm)	68.50	77.75	7.75	43. 25	62. 50
TJ_{500} (s)	8.72	6.64	3.12	6	7.62

The results of slump-flow and flow rate for the reference mixtures are slightly different. It shows a moderate sensitivity to the variation of SP and maximum aggregate size, but the difference is not that great. The results illustrate that, using of modified A&A model to design the reference mixtures for both D_{max}= 12 mm & 16 mm is an efficient method.

Based on the fact that, the compositions of reference mixtures are different; to have comparable results, flowability ratio is defined equal to the proportion of slump-flow of fibre concrete and reference concrete. Also similar parameters are defined for passing-ability and flow rate.

Figure 11 shows the flowability ratio versus fibre volume fraction of BF-SCC A, B and C series. As it is mentioned earlier, the target for the fibre content assumed to be 2% of volume fraction, but to produce a BF-SCC by using the employed reference mixtures, it is not possible to use more than 1.15% of fibres for D_{max}= 16 mm and 1% for D_{max}= 12 mm.

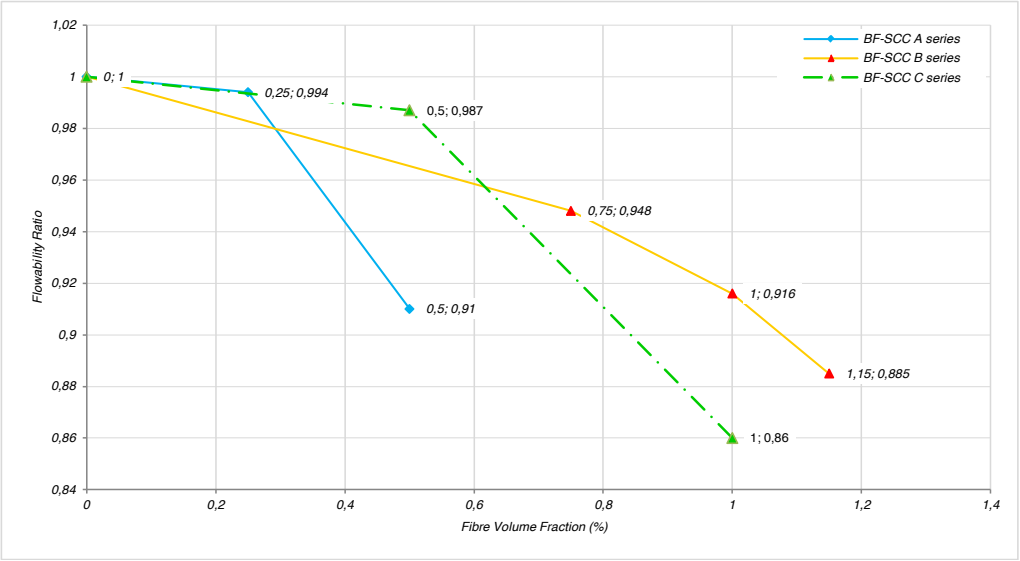

Figure 11 - Flowability ratio versus fibre volume content of BF-SCC A, B and C series.

As it may be predicted, flowability decreases by increasing the fibre content. It seems that each type of mixture has an inflection point on the diagram depending on its composition and maximum aggregate size. By increasing the fibre content more than the critical point, flowability drops drastically. Based on performed experiments, increase in the volumetric content of superplasticizer above a critical value would lead to bleeding and segregation of fresh concrete. Therefore, in fiber concrete, increasing of the superplasticizer above a critical value is not useful for solving the flowability issues pertaining to the fibres clustering effect.
Higher surface area, rearrangement of the granular structure and friction between the fibres and aggregates are the main effective parameters influencing workability of fibre concrete [12].

The concrete with D_{max} = 12 mm shows a lower flowability ratio in comparison with the mixture composed of D_{max} = 16 mm. One reason for this phenomenon is probably because of the higher number of contact spots between gravel particles and fibres. Therefore the mixture has a higher tendency for clustering. Based on this hypothesis, flowability may be introduced as a function of $\frac{l_{fibre}}{D_{max}}$ ratio. Also depending on the maximum aggregate size and fibre content for each concrete composition, it should be a critical fibre length to reach to an acceptable flowability. For D_{max} = 16 mm, the ratio is equal to 2.69 and for D_{max} = 12 mm the ratio is equal to 3.58, this shows that $\frac{l_{fibre}}{D_{max}}$ ratio has an inverse effect on the flowability. Proof of this hypothesis needs an extensive study, dedicated to the fiber size, its effect on the matrix viscosity and granular structure of concrete mix which is not in the scope of this article.

Based on similar matrix content for all concrete compositions, in this study Matrix-Particle (MP) model is more pronounced for the behaviour of reference mixes than, the basalt fibre concrete. Tests on several fibre lengths combined with different D_{max} are needed.

Figure 12, shows the clustering ratio versus fibre volume fraction of BF-SCC A, B and C series.

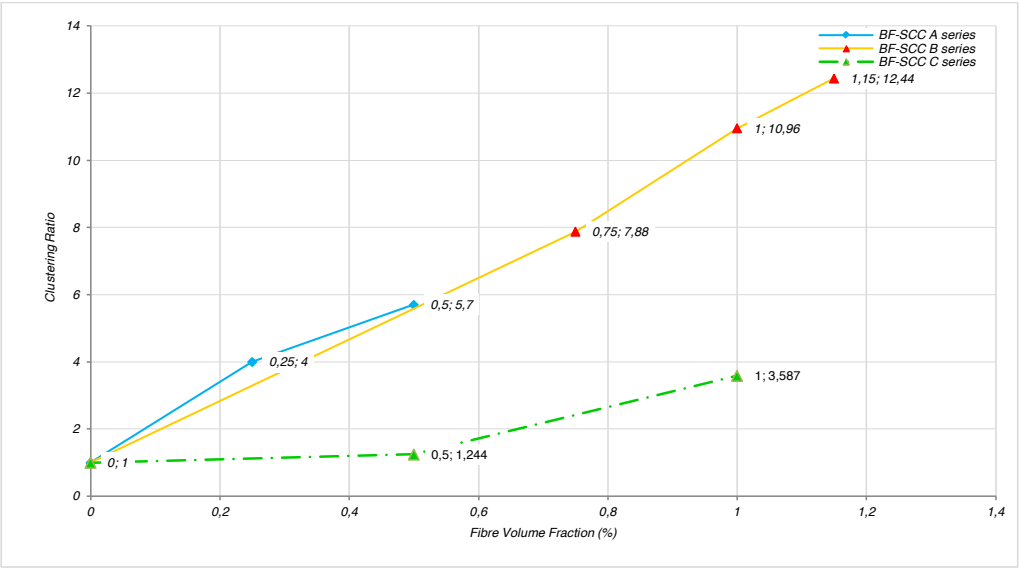

Figure 12 – Clustering ratio versus fibre volume content of BF-SCC A, B and C series.

Figure 12 represents a comparative clustering effect, where macro basalt fibre is used for the fibre concrete. Clustering ratio is defined as $\frac{PJ\ of\ fibre\ concrete}{PJ\ of\ referance\ concrete}$. It can be noticed that, by increasing the fibre content, clustering effect increases, therefore passing-ability ratio can be defined as $\frac{1}{clustering\ ratio}$.

According to Eurocode 2 [23], spacing of the bars shall be specified in a manner that, the concrete could have adequate passing-ability for the development of necessary bond. For conventional concrete it is defined as the maximum value between the bar diameter and (D_{max}+5mm) [23]. But this criterion is not applicable for fibre concrete; therefore based on the type of project, structural element and reinforcement material, the J-ring test shall be designed according to the minimum bar spacing.

Flow rate of BF-SCC

Figure 13, shows the ratio of t_{500} versus the fibre volume content for three series of tested compositions. The flow rate ratio can be defined as $\frac{1}{ratio\ of\ t_{500}}$ which is an indication for the viscosity of concrete mixture. In general, all the diagrams show a reduction in flow rate ratio. The diagrams of A and C series show the inflection points similar to the flowability diagrams that could be assumed as the critical fibre content.

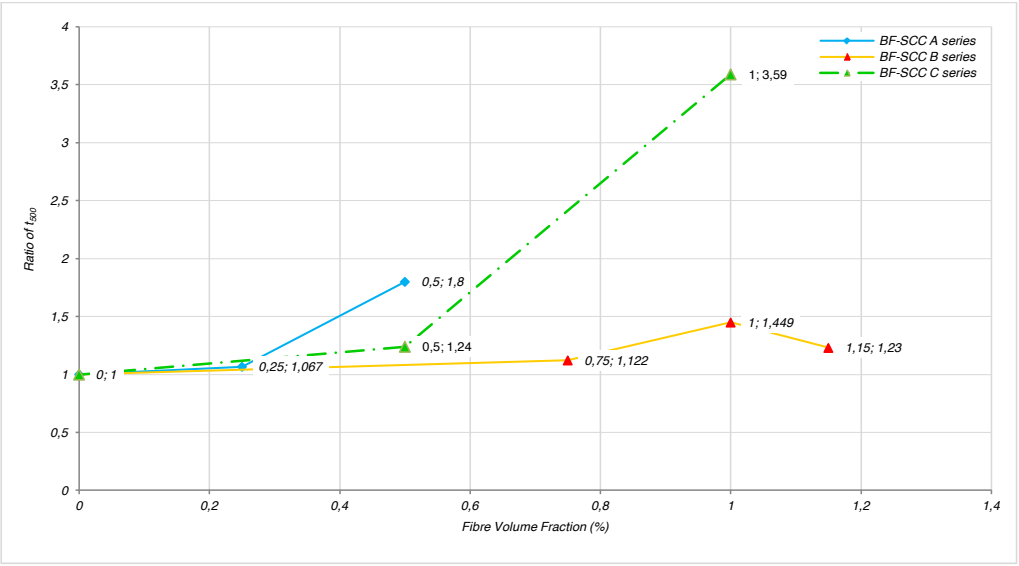

Figure 13 – Ratio of t_{500} versus fibre volume content of BF-SCC A, B and C series.

Fibre dynamic segregation

Available methods for evaluation of fibre static segregation including: segregation cylinder, ultrasonic method and computed tomography (CT) scan [24] are based on the density differences between concrete and fibres. The density of steel fibres is more than 3 times of concrete density whilst the density of basalt fibres is close to the density of concrete, therefore these methods are more useful for steel fibres.

Due to presented facts and the time limitation in this study, just dynamic segregation of BF-SCC C3 for two levels of superplasticizer was evaluated. The normalized fibre concentrations for 2.5% and 2.75% of SP were equal to 0.369 and 0.70, respectively. The number of results is limited but the results suggested that, for the same fibre content of 1%, by increasing the superplasticizer to a certain level (maximum 2.75 % for the introduced composition), fibre dynamic segregation decreases.

3.2 BF-CSC performance

Relative slump of BF-CSC

The results of slump test are summarized in Table 7. As logically expected, slump reduces by increasing the fibre content. Figure 14, illustrates the slump ratio of conventional concrete for the range of 0 to 2 percent of macro basalt fibres. The slump shows a higher gradient between 1.5% and 2% of fibres. Therefore 1.5% of fibres may be assumed as the critical fibre content for the investigated CSC composition.

Table 7 - Test results of reference CSC and BF-CSC.

Flow Characterization	BF-CSC 1	BF-CSC 2	BF-CSC 3	BF-CSC 4	BF-CSC 5	BF-CSC 6
Fibre VF (%)	0	0.50	1	1.25	1.5	2
Slump (mm)	265	261	229	215	211	148

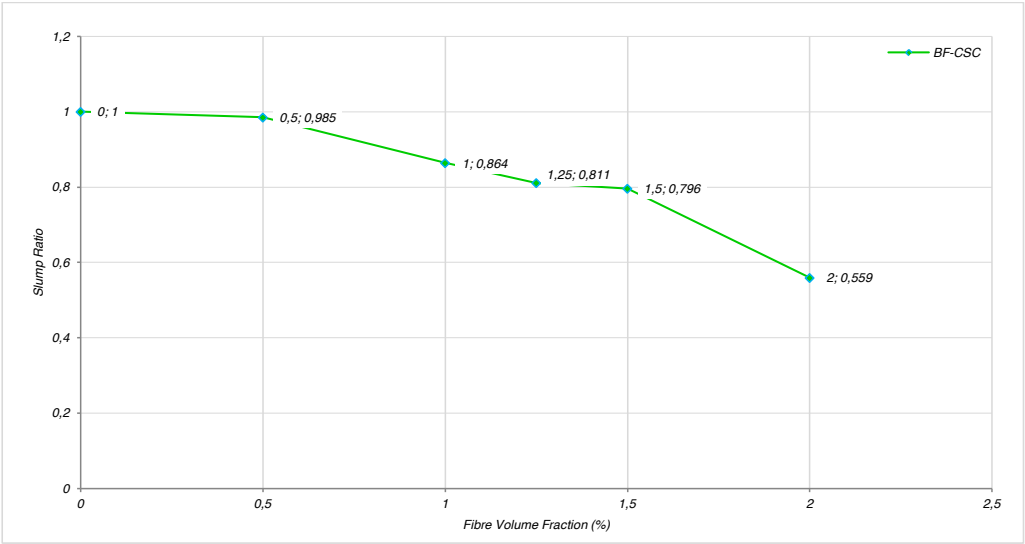

Figure 14 – Slump ratio versus fibre volume content of BF-CSCs.

4. CONCLUSIONS

This paper describes the mix design and mixing procedure of macro basalt fibre self-compacting concrete and conventional slump concrete. The mix design is based on absolute volume method where modified A&A model was utilised as a target for optimum particle size distribution. The following conclusions are obtainable from the presented results:

- By using the absolute volume method, in combination with the modified A&A particle packing model, flowability of more than 750 mm for the reference mixtures is obtainable.
- It is possible to produce stable and flowable BF-SCC composed of $D_{\max}$= 16 mm for the maximum fibre content of 1.15%.
- Due to the flowability testing results for both $D_{\max}$= 12 mm & 16 mm, flowability seems to have an inverse relation with $\frac{l_{\text{fibre}}}{D_{\max}}$ ratio.
- Based on the J-ring testing results, passing-ability ratio reduces by increasing the fibre content. Also it is concluded that, to have a representative result, J-ring test shall be modified according to the requirements of individual projects.
- Fibre dynamic segregation, decreases by increasing the superplasticizer content to a certain level.
- Slump testing results show a linear reduction due to increase of fibre content, but fibre volume fractions of 1.5% behave as a critical value where slump shows a higher reduction beyond this point.

The above conclusions are valid for the investigated concrete compositions.

ACKNOWLEDGEMENT

The first author greatly appreciates the inputs from his PhD supervisor Dr Anniken Karlsen during the writing process. He is also grateful to the companies ReforceTech, UlsteinBetong and Mapei for providing valuable materials and information.

REFERENCES

1. Mohammadi Mohaghegh, A., Silfwerbrand, J., Årskog, V. "An Initial Investigation of the Possibility to Use Basalt Fibres for More Durable Concrete Structures in Norwegian Fish Farming", proceedings XXII Nordic Concrete Research Symposium, Reykjavik, Iceland, 2014, pp. 219-222.
2. Sahmaran, M., Yurtseven, A., Ozgur Yaman, I., "Workability of Hybrid Fiber Reinforced Self-Compacting Concrete", Building and Environment, Vol. 40, Issue 12 (2005), pp. 1672-1677.
3. Ferrara, L., Bamonte, P., Caverzan, A., Musa, A., Sanal, I., "A Comprehensive Methodology to Test the Performance of Steel Fibre Reinforced Self-Compacting Concrete (SFR-SCC)", Construction and Building Materials, Vol. 37 (2012), pp. 406–424.
4. Ferrara, L., Park, Y.D., Shah, S.P., "A Method for Mix-Design of Fiber-Reinforced Self-Compacting Concrete", Cement and Concrete Research, Vol. 37 (2007), pp. 957-971.
5. Zhu, W., Bartos, P.J.M, "Permeation Properties of Self-Compacting Concrete", Cement and Concrete Research, Vol. 33 (2003), pp. 921-926.
6. Kaasgaard, M., Pade, C., Jönsson, U., Munch-Petersen, C., "Comparison of Durability Parameters of Self-Compacting Concrete and Conventional Slump Concrete Designed for Marine Environment" Nordic Concrete Research, no. 47, 2013/1, pp. 13-24.
7. Offshore standard, "Offshore Concrete Structures", DNV-OS-C502, Det Norske Veritas, September 2012.
8. Norwegian standard, "Concrete Part 1: Specification, Performance, Production and Conformity", NS-EN 206-1:2001, Oslo, Norway, 2001
9. Patnaik, A., "Gen3.1 MiniBar Reinforced Concrete (MRC)" ReforceTech Basalt Fiber Reinforcement Technology, NO-1383 Asker, Norway (2013).
10. Norwegian Concrete Association, "Guidelines for Production and Use of Self-Compacting Concrete", Publication no. 29, Oslo, Norway, 2002.
11. Smeplass, S., Mørstsell, E., "The Applicability of the Particle Matrix Model to Self Compacting Concrete (SCC)", Nordic Concrete Research no. 26, 2001/1.
12. Yu, R., Spiesz, P., Brouwers, H.J.H., "Mix Design and Properties Assessment of Ultra-High Performance Fibre Reinforced Concrete (UHPFRC)", Cement and Concrete Research, Vol. 56, (2014), pp. 29–39.
13. Fennis, S.A.A.M, Walraven, J.C, "Using Particle Packing Technology for Sustainable Concrete Mixture Design", HERON Vol. 57 (2012) No. 2, pp. 73–101.
14. Radix, H.J., Brouwers, H.J.H., "Self-Compacting Concrete: The Role of The Particle Size Distribution", proceedings First International Symposium on Design, Performance and Use of Self-Consolidating Concrete (SCC), Changsha, Hunan, China, 2005, pp. 109-118.

15. Anlegsement FA technical data [Online] Available at: http://www.norcem.no/no/node/4941 [Accessed 10 Dec. 2014].
16. Test Report of Particle Size Analysis by Laser Diffraction for FESIL As, 2012, Contact Information: silica@fesil.no.
17. Dynamon SX-N technical data [Online] Available at: http://www.mapei.com/public/COM/products/Dynamon_SX-N_gb.pdf [Accessed 10 Dec. 2014].
18. Viscofluid SCC/10 technical data [Online] Available at: http://www.mapei.com/public/COM/products/767_viscofluidscc-10_gb.pdf [Accessed 10 Dec.2014].
19. Mapeair 25 technical data [Online] Available at: http://www.mapei.com/public/COM/products/mapeair_25_gb.pdf [Accessed 10 Dec. 2014].
20. Norwegian standard, "Concrete Part 9: Additional Rules for Self-Compacting Concrete (SCC)", NS-EN 206-9:2010, Oslo, Norway, 2010.
21. Norwegian standard, "Testing Fresh Concrete Part 8: Self-Compacting Concrete Slump-Flow", NS-EN12350-8:2010, Oslo, Norway, 2010.
22. Norwegian standard, "Testing Fresh Concrete Part 12: Self-Compacting Concrete J-ring Test", NS-EN12350-12:2010, Oslo, Norway, 2010.
23. Norwegian standard, "Eurocode 2: Design of Concrete Structures, Part 1-1: General Rules and Rules for Buildings", EN 1992-1-1: 2004+NA: 2008, Oslo, Norway, 2008.
24. Grigaliunas, P., Kringelis, T., "SCC Flow Induced Steel Fiber Distribution and Orientation. Non-Destructive Inductive Method" Available at: http://www.ndt.net/events/ECNDT2014/app/content/Paper/626_Grigaliunas.pdf [Accessed 30 Jan. 2015].

Parameters Influencing the Initial Setting Time of Alkali-Activated Ground Granulated Blast furnace Slag Materials

Helén Jansson, Ass. Prof.
Chalmers Univ. of Techn.
Div. of Building Technology
SE 412 96 Gothenburg, Sweden
Email: helen.jansson@chalmers.se

Luping Tang, Prof.
Chalmers Univ. of Techn.
Div. of Building Technology
SE 412 96 Gothenburg, Sweden
Email: tang-luping@chalmers.se

ABSTRACT
Various parameters influencing the initial setting time of alkali-activated slag materials have been investigated using the Vicat method. The alkali solutions used for the activation were liquid sodium silicate (water glass) of different moduli n (SiO_2/Na_2O ratio) and pH. The results indicate that the initial setting time is mainly influenced by two parameters; 1) the specific surface area of the slag and 2) the modulus of the solution. The results also suggest that the problem with controlling the initial setting time of alkali-activated slag can be solved by controlling the characteristics of the solvent used for the activation.

Keywords : alkali-activation, initial setting time, water glass modulus, sodium silicate solution, pH, specific surface area

1. INTRODUCTION

The increasing requirements for reduction of greenhouse gas emissions have led to the search for low CO_2 footprint cements that can be used as a complement or alternative to ordinary Portland cement (OPC). One such promising material is the industrial by-product ground granulated blast furnace slag (GGBS), which is known to have cementitious properties under alkali-activation [1]. When compared to OPC this type of materials also has the advantage of a different and finer pore structure that [1-3], for instance, result in lower water permeability as well as lower ion and molecular diffusivity. As a result, the material shows higher resistance to various aggressive media compared to OPC [1, 4]. The smaller pore size distribution and the addition of alkaline ions into the matrix also result in a depression of the water freezing temperature and, thus, an increase in the resistance against freeze-thaw damages [4, 5]. The higher strength, smaller pore size, lower permeability and higher resistance against chemical attacks etc., make them also to be possible alternatives for storage of radioactive waste and immobilization of toxic metals [6-9]. In addition, this type of cementitious materials shows even better fire resistance than OPC [1]. A recent review of this type of materials is given in [10].

However, a serious problem and also one of the limiting factors for extensive use of green alternatives to OPC is the difficulty in controlling the initial setting time [1, 11]. Despite extensive research on this type of materials, the initial reaction and hydration, which lead to the initial setting time, is not fully understood [1, 12-14] but it is generally accepted that parameters like the chemical composition of the cementitious material [1], the water content [15, 16], the viscosity of the initial mixture [17], the mixing time [18, 19] and the specific surface area (fineness) of the material [20] are of importance for the early reaction and the initial setting time. In addition, the initial setting time is highly dependent on the type of alkali used for the activation and, therefore, investigations are often focused on this parameter.

From the literature it is obvious that the most commonly used activators belong to the groups alkali-hydroxides and alkali-silicates, even if acid salts and aluminum containing compounds also can be used [1] for the alkali-activation of cementitious materials like GGBS. From studies on the influence of different types of alkali-hydroxides, see for instance [1, 17, 21-27], there are indications that some of them are more effective activators than others [21]. Whereas some accelerate the hydration process [25], other types of alkali-hydroxides have the opposite effect [17]. However, when the cementitious material contains a large amount of calcium oxide (CaO), as in the case of GGBS, the alkali-silicates are in general more effective activators than the alkali-hydroxides [1, 28] (and references therein).

The most commonly used type of alkali silicate activators is based on sodium silicates ($Na_2O{\cdot}nSiO_2$) of various moduli n. From investigations on the effect of sodium silicate solutions [15, 16, 24, 27], it has been suggested that the pH and the alkali modulus n are of less significance than the amount of activator, and that the content of SiO_2 is of higher importance than the content of Na_2O [16]. In addition, it has been suggested that the type of sodium silicate is of importance since it was shown that the setting time is much faster when dry (powder) sodium silicates is used for the activation than if liquid sodium silicate (commonly called water glass) is used [29].

From studies found in the literature it is thus obvious that many different factors are of importance for the early reaction and the initial setting of alkali-activated cementitious material. In this study we have used sodium silicate solutions (water glass) for the alkali activation of GGBS and examined some of the parameters that are suggested to have an influence on the initial setting time. The results show that the initial setting time of GGBS can be designed and controlled by controlling the characteristics of the activating solution.

2. MATERIAL AND METHODS

2.1 GGBS materials

Two Swedish GGBS materials, Merit 5000 (***M***) and Hyttsand (***H***) from Merox AB, and one German product (***G***), from Tomas Concrete Group, have been used for this study. As shown in Table 1, the two Swedish products (***M*** and ***H***) have exactly the same chemical composition but they have different specific surface areas, whereas the German product (***G***) is different in both chemical composition and specific surface area compared to the ***M*** and ***H*** materials. It can be noted that the basicity coefficient Kb = $(CaO+MgO)/(SiO_2+Al_2O_3)$ [16] is about the same (around 1) for all three GGBS products whereas the hydration modulus HM = $(CaO+MgO+Al_2O_3)/SiO_2$ [16] differs somewhat (1.79 for ***M*** and ***H***, and 1.89 for ***G***). However,

for all the GGBS materials the value of HM is larger than 1.4, which is the minimum value to ensure sound hydration properties [16].

Table 1 – Chemical compositions (in wt%) and physical properties of the GGBS materials used in this study (as given by the suppliers)

Chemical composition and physical properties	***M*** Merit 5000	***H*** Hyttsand	***G*** German
CaO	31	31	40
SiO_2	34	34	35
Al_2O_3	13	13	12
Fe_2O_3	0.4	0.4	
SO_3	0.25	0.25	≤ 0.2
Alkalinity (Na_2Oeq)	0.9	0.9	1.2
MgO	17	17	7
TO_2	2.4	2.4	≤ 1.2
Mn_2O_3	0.8	0.8	≤ 0.6
Cl^-			≤ 0.05
S^{2-}	1.3	1.3	
Specific surface area, SSA (cm^2/g)	5000	3500	4200
Glass content (%)	99	99	≥ 90

2.2 Alkali solutions

For the alkali-activation, sodium silicate solutions (commonly called water glass) of various moduli were used. The solutions were prepared by adding dissolved sodium hydroxide (NaOH, Fisher Scientific) to a commercial available water glass from Sibleco Nordic. The latter contains 27.6 wt% of SiO_2 and has the molar modulus n = 3.35. In order to allow for thermal equilibrium, each specific alkali-solution (i.e. sodium silicate and sodium hydroxide) was prepared more than one day prior to the use in the sample preparations.

2.3 Sample proportions

For all samples, the amounts of the commercial water glass and GGBS material were 20 g and 50 g, respectively, and the water-to-GGBS (dry material) ratio was kept constant at w/s = 0.5. Thus, only the water glass modulus was varied, which in turn influences the pH of the prepared solution, as shown in Table 2. In this table it is furthermore shown how the Na_2O/CaO and Na_2O/GGBS ratios and pH vary for the different ***M***-samples (i.e. GGBS material, sodium silicate solution and sodium hydroxide). The samples are hereafter denoted by the added NaOH solution concentration (ranging from 5 to 35 wt%) together with the specific water glass modulus n of the activating solution given in a parenthesis.

2.5 pH measurement of the alkali-activated samples

In order to measure the pH values of the alkali-activated GGBS samples, the following steps were taken. First, the GGBS material was mixed with the prepared water glass solution of a specific modulus. Secondly, a specific volume of the sample was taken into a vial and thereafter diluted. Third, the slurry was subsequently centrifuged for quick sedimentation. Finally, the measurements were done on the solution on top of the sediment and then recalculated to take the dilution into account.

It should be noted that in some cases the measured pH values of the samples were > 14 and they are not included in Table 2. The reason for this is that a sodium ion error generally occurs at higher pH values, i.e. where the hydrogen ion concentration is very low compared to the sodium ion concentration, which results in a lower value of the pH than the actual one [30].

Table 2 – Sample compositions and relevant initial parameters (** pH > 14*)

Sample	NaOH (wt% in water)	pH (water glass)	pH (in mixture)	SiO_2/Na_2O (molar modulus *n*)	Na_2O:CaO (mole %)	Na_2O:Slag (wt %)
Merit 5000						
M5	5	11.82	12.56	2.59	11.3	4.2
M7	7	12.11	12.78	2.36	12.3	4.6
M8	8	12.24	12.88	2.25	12.8	4.8
M9	9	12.42	13.02	2.16	13.3	5.0
M10	10	12.6	13.13	2.07	13.8	5.2
M12	12	13.02	13.36	1.90	14.9	5.6
M15	15	13.31	13.61	1.69	16.4	6.3
M20	20	13.59	13.86	1.40	19.2	7.5
M25	25	13.81	----*	1.17	22.1	8.8
M30	30	13.90	----*	0.99	25.2	10.3
M35	35	13.98	----*	0.84	28.4	12.0
TCG / German						
G5	5	11.82		2.59	9.0	4.2
G10	10	12.6		2.07	11.1	5.2
G15	15	13.31		1.69	13.2	6.3
G25	25	13.81		1.17	18	8.8

2.4 Vicat test method

The initial setting time, i.e. the time when the material loses its plasticity, was measured by a standard Vicat equipment (Toni Technik) with a calibrated weight of 300 g and a cylindrical needle with a flat tip area of 1 mm^2. Each sample composition was measured in certain time intervals, somewhat dependent on the concentration, and in triplicate to ensure repeatability and to obtain an average value of the initial setting time.

2.6 Ion chromatography

A Dionex ion chromatography (IC) system (Dionex ICS series) was used to quantify the amount of dissolved calcium ions for some of the sample compositions. For these measurements we used the same solution extraction methodology as for the pH determination (as previously described).

3. RESULTS

3.1 Initial setting time as a function of water glass modulus

Fig. 1 shows the setting time profiles for some of the measured ***M***-samples. It can be observed that the initial setting time displays a minimum for the sample ***M10*** (n = 2.07) and that it is longer for both the ***M7*** and ***M20*** samples (n = 2.36 and 1.40, respectively). It should be noted that these latter samples contain either lower or higher concentration of sodium (activated with water glass of higher or lower moduli, respectively) compared to the sample ***M10*** (n = 2.07). The sample ***M20*** (n = 1.40) shows, furthermore, a faster initial setting time than ***M7*** (n = 2.36). From this figure it can also be observed that the sample made of Hyttsand (***H***) did not show any initial setting after two hours. In fact, independent on the moduli of the water glass used for the activation, the initial setting was so slow that sedimentation of the GGBS particles occurred, and no initial setting was obtained even after 24 hours. This material is therefore considered as

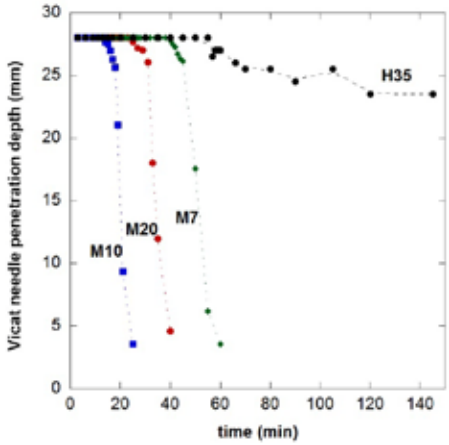

*Figure 1 – Typical setting time profiles (an average based on three different measurements) for three of the **M**-samples and one of the **H**-samples.*

inactive in the time interval of interest for this study.

In Fig. 2 the initial setting times obtained for the entire series of ***M***-samples, i.e. ***M5*** (n = 2.59) to ***M35*** (n = 0.84) are shown by solid circles. As indicated already in Fig. 1, the initial setting time is fastest for the sample ***M10*** (n = 2.07) and becomes longer at both higher and lower sodium content (lower and higher water glass moduli). From the Fig. 2 it can also be observed that the initial setting time seems to show two different moduli dependences. For samples activated with water glass of moduli higher than n = 2.07 (***M10***), a rapid decay with increasing sodium content (decreasing modulus) is shown whereas at higher concentrations (lower moduli)

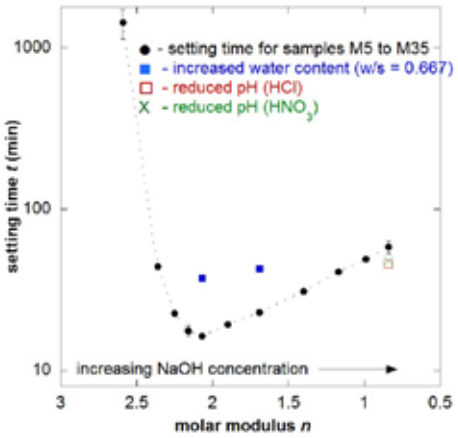

*Figure 2 – The initial setting times (in minutes) for the series of **M**-samples as a function of modulus. n of the water glass used for the alkali-activation.*

the initial setting times are more smoothly increased. The reason for a minimum in the setting time curve is not obvious and one possible explanation, which will be discussed in section 4 below, is that the water glass used for the alkali-activation has different effect on the GGBS material in the different concentration (moduli) regions.

3.2 Initial setting time as a function of particle size

By use of the GGBS material ***G*** instead of the material ***M***, the specific surface area is reduced from 5000 cm^2/g to 4200 cm^2/g (Table 1). In Fig. 3 the obtained initial setting times for the samples ***G10*** (n = 2.07), ***G15*** (n = 1.69), and ***G25*** (n = 1.17) and the corresponding ***M***-samples are shown. These results clearly indicate that the initial setting time is dependent on the specific surface area since it is increased for the ***G***-material, which contains larger particles.

However, for the ***G*** material not only the specific surface area but also the chemical composition is different compared with the ***M*** material. As shown in Table 1, the main differences are the MgO, CaO and the glass contents. Especially the Mg content might be of importance since it previously was shown to have an influence on the initial rate of reaction [31, 32]. In addition, the content of Mg, and then particularly the ratio Mg/Si, influences the structure development in the early stage of the hydration [33]. It is thus not obvious if the increased initial setting time of the ***G***-samples is caused by the larger specific surface area or the difference in chemical composition. However, since a lower MgO content should result in a faster initial reaction [32]

the longer initial setting time of the ***G***-samples indicates that the specific surface area is more important than the chemical composition.

In order to further investigate the specific surface area dependence on the initial setting time, the weight fractions of the two chemically identical GGBS materials ***M*** and ***H*** was (see Table 1) systematically varied. For these measurements the water glass of modulus $n = 1.69$ was used as the activator. The results, as a function of the specific surface area after replacement of ***H*** (wt%), are shown in Fig. 4 (solid circles). From this figure it is clear that the specific surface area has a distinct influence on the initial setting time since the smaller the specific surface area, the longer initial setting time is obtained.

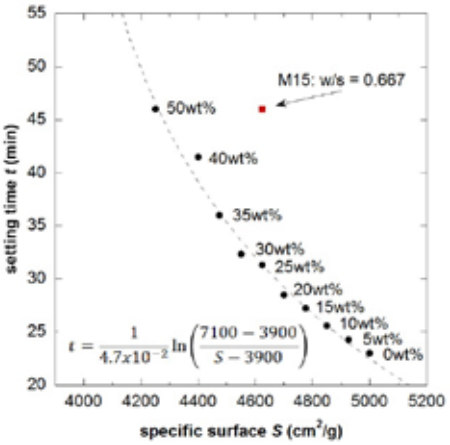

*Figure 4 – The initial setting times as a function of the specific surface area (obtained by replacing **M** with different weight fractions of **H** as given in the figure). The dotted line displays the curve fitting by equation 1 (also given in the figure). T = 20°C.*

4. Discussion

4.1 pH dependence

Even if the hydration mechanism is poorly understood [1], it is generally believed that the hydration process of GGBS materials occurs in several steps and starts with the wetting and (partly) dissolution of slag particles. At this stage of the process there is a destruction of slag bonds, such as Ca-O, Mg-O, Si-O-Si, Al-O-Al and Al-O-Si, and the dissolved ions migrate out of the slag material into the liquid phase surrounding the particles [33]. Thereafter a Si-Al layer is formed on the surface of the slag particles and subsequently the C-S-H gel is developed [34]. During this so-called dissolution phase, the bond breaking and the following diffusion of ions should be highly dependent on their solubility (and consequently on the pH [35]). A higher solubility would thus result in a higher content of dissolved and diffusing ions.

For alkali-activated GGBS materials the solubility of different ions, as a function of pH, was previously studied by investigating the pore solution as a function of hydration time. It was found that the solubility of Si, Ca, Al and Mg is strongly dependent on the pH [36] at all times during the hydration process. In Ref [36] it was furthermore shown that for pH values higher

than 11.5 the concentrations of Si and Al are increasing whereas the concentrations of Ca and Mg are decreasing. Since both the silica content [37] and pH [36] affect the formation of C-S-H, it was suggested that the solubility of silica, and then consequently the pH, is the most important factor for alkali-activation of GGBS [36].

The pH seems thus to be a possible candidate for determining the initial stage and setting time of alkali-activated GGBS materials. If so, keeping water, sodium and silica contents, (and thereby the water glass modulus *n*) of the alkali-activating solution unchanged, but reducing pH, should have a noticeable influence on the initial setting time. Therefore, two pH adjusted water glass solutions were prepared and used for the activation. For this experiment the water glass used for the activation of the ***M35*** (n = 0.84, pH 13.98) sample was pH adjusted, by hydrochloric acid (HCl) or nitric acid (HNO_3), to about the same value as the pH of the solution used for activating the ***M15*** sample (n = 1.69, pH 13.3). Thus, the value of the modulus was kept at n = 0.84 but the pH was adjusted to 13.3. If the pH is the main determining parameter, the initial setting time of these samples should be the same as for the sample activated by the solution of the higher modulus (n=1.69). However, as can be observed in Fig 2, where the initial setting times for the HCl and HNO_3 adjusted samples are shown by an open square and a cross, respectively, this seems not to be the case. Even if the initial setting times are somewhat reduced for samples activated by the pH adjusted solutions, they are still far from that of the ***M15*** sample. Thus, even if the pH of the alkali-activating solution has a large influence on the solubility of ions it seems not to be the main responsible parameter, at least not the only decisive factor, for the initial setting time. It should be noted that the addition of chloride ions Cl^- (from the addition of HCl) might induce structural changes of the water glass [38]. However, since similar initial setting times are obtained for both samples, independent on the type of acid used for the pH adjustment, this seems to be a minor problem. It should also be noted that for ordinary Portland cement (OPC), both chloride and nitrate ions may accelerate the hydration process [33, 34] but as shown from this study, for alkali-activated GGBS materials this acceleration effect appears not to be significant compared to the effect of the water glass modulus.

Another explanation for the different behaviors of the initial setting time for samples activated with water glass of various moduli could be that the change of modulus, by the addition of NaOH, not only affects the pH of the solution (and the dissolution phase), but also the microstructure of the solution itself. The structure of water glass is known to be strongly dependent on, for instance, the pH and the silica content [39]. Increased pH results in smaller particles sizes with decreased number of Si-O-Si bridges, with an increased viscosity as a consequence. Thus, for water glass of higher pH there are indications that larger silica particles/aggregates break up into smaller units [39], which most likely influences how fast slag ions can interact with the silicate units, i.e. the silicate anions.

4.2 Water glass modulus (n) dependence

The addition of NaOH to water glass does not only change the pH but also the modulus *n*, and the structure and viscosity of water glass solutions. In a previous investigation [38], it was shown that the viscosity of water glass is extremely dependent on the modulus. Of interest for this study is that the viscosity increases as the solution is either more siliceous or more alkaline, i.e. at both lower and higher moduli. Thus, at a certain value of the modulus, a viscosity minimum of the water glass was found. Interestingly, the value obtained for the minimum was n = 1.8 [38], which is close to the value where the pH shows an inflection point, as shown in Fig.

5. Since this is also the concentration where the fastest initial setting time of our series of ***M***-samples, i.e. ***M10*** (n = 2.07) is obtained (see Figure 2), one might speculate that the initial setting time to a large extent is dependent on the viscosity of the solution used for the activation [40].

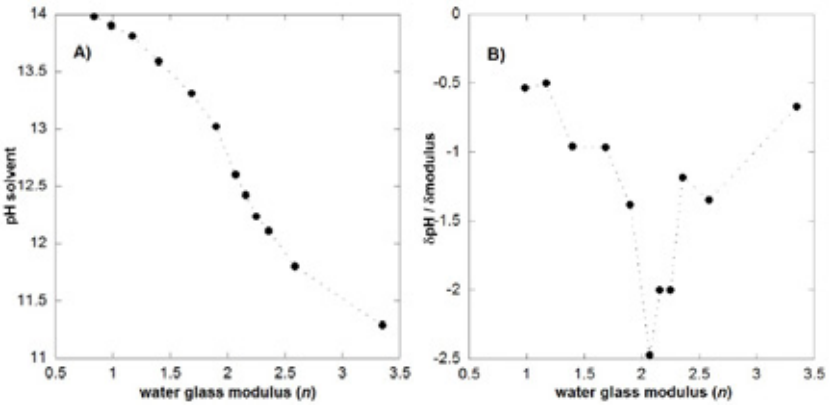

Figure 5 – A) pH values of the solutions used for the sample preparations and the pH value of the as received solution (n = 3.35). B) The inflection point in pH is found at n = 2.07, as shown by the derivative curve.

In Fig. 6 the concentration of dissolved calcium ions for some of the investigated samples, as determined by ion chromatography (IC), is shown. It can be observed that the largest fraction of these ions is found in the same sample composition as the one for which the fastest initial setting time is obtained, i.e. the sample ***M10*** (n = 2.07). Thus, in the sample ***M10***, the highest amount of calcium ions are available for the structure development of the hydration product. Since the solubility of alkali-hydroxides decreases with increased pH [35], this behavior should mainly be dependent on how easy (and fast) dissolved ions are transported out from the solid particle surface into the surrounding liquid. Accordingly, the amount of dissolved calcium ions in the solution should be highly dependent on the viscosity of the solution, which in turn, should have an influence on the initial setting time. This suggestion would then be in agreement with previous studies that have shown that the viscosity of the activating solution has a large influence on the initial setting time and hydration process of alkali-activated GGBS [17, 29, 41]. More specific, the early reaction of alkali-activated mineral materials is diffusion controlled [29, 41], and therefore also dependent on the viscosity of the initial mixture [17].

A similar modulus dependence of the initial setting time was previously observed [42] for GGBS activated by water glass of three different moduli (n = 1.6, 2.0 and 2.4). In agreement with the results from this study, the fastest initial setting time was also in that study obtained for the sample activated by water glass of modulus n = 2.0 whereas both lower (n = 1.6) and higher (n = 2.4) moduli resulted in longer initial setting times. In that study [42] isothermal calorimetric scans were combined with results obtained by the Vical method and it was shown that both the initial and final setting times, as well as the heat evolution during the hydration, were influenced by the modulus of the activator. Since alkali-activation is known to be highly dependent on both

the chemical composition of the binder material and the activator concentration, the results from Ref [42], in combination with the present findings, imply that the setting time of GGBS must be extremely dependent on the water glass solution used for the activation. Actually, a similar conclusion was previously drawn from a study in which it was shown that the initial stage of the gelation process of alkali-activated materials is determined by the structure of the water glass used for the activation [43]. However, since the structure of water glass is dependent on the pH of the solutions [39], more detailed measurement on the molecular arrangement in such liquids are needed to elucidate if it is the structure or the pH of the liquid that is the most important parameter for the initial setting time of alkali-activated materials.

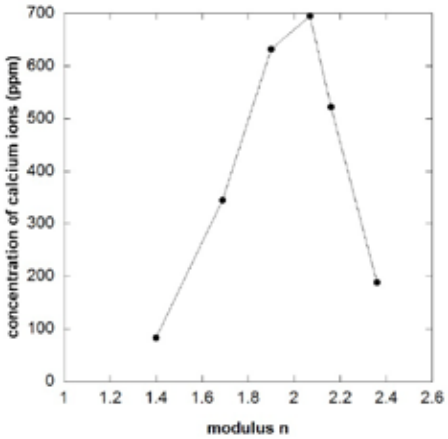

Figure 6 – The concentration of dissolved calcium ions during the first stage in the hydration process, i.e. in the dissolution phase.

4.3 Particle size dependence

Fig. 3 gives an indication on that the initial setting time is dependent on the specific surface area. Although the calcium content in the ***G***-samples is higher than in the ***M***-samples (see Table 1), the smaller specific surface area of the ***G***-material most likely limits the availability, and thereby also the dissolution, of calcium ions from the solid material, which is necessary for building up the initial network of hydration products. As a consequence, a smaller specific surface results in a longer initial setting time.

From the results shown in Fig. 3 it can also be observed that the difference in initial setting times between the ***M*** and ***G***-samples decreases with decreasing moduli of the activating solution. For samples activated with water glass of moduli n = 2.07, 1.69 and 1.17, the initial setting time differs by a factor of 2.6, 1.8 and 1.4, respectively. For alkali-activated cementitious materials it has previously been shown that a larger specific surface needs more hydration water [5] and a possible explanation for the reduced difference might then be that the finer slag particles (i.e. the larger specific surface area) in the ***M***-samples can absorb more water on the surfaces. The larger amount of absorbed water should, in turn, result in that the fraction of free water, in the solution, is decreased for these samples. Since characteristics, such as structure and viscosity, of water glass are known to be dependent on the water content [38], the fraction of

water in the solution should also have an influence on the initial stage of the alkali-activation. Thus, with decreasing water glass modulus, the viscosity of the ***M***-samples most likely increases faster compared to that of the ***G***-samples. Since the initial stage of the hydration process, and the subsequent development of hydration products, is dependent on the diffusion of ions, an increased viscosity would result in a slower diffusion. This should, in turn, result in a longer initial setting time. As a consequence, the faster increase in the initial setting time of the ***M***-samples should reduce its difference from that of the ***G***-samples.

By keeping the solution at a constant modulus and successively increasing the particle size by replacing parts of the ***M***-material with the ***H***-material, it is obvious that the increased particle size results in an increasing initial setting time, as shown in Fig. 4. This behavior is expected since the initial setting time should be related to the initial flow, that previously has been shown to be dependent on the fineness of the material [20]. In that previous study it was shown that an increase in fineness of the slag particles leads to a decreased initial flow, which most likely has an effect on the rate of chemical reactions [44] during the initial stage of the hydration process.

The initial setting time is found at the point at which the material loses its plasticity during the initial stage of the hydration. This time, here denoted t, is related to the development of a specific quantity of hydration products, which in turn is dependent on the reaction rate when the volume is constant [44]. Since the initial setting time also is dependent on the rate of dissolution of ions from the GGBS material, and how fast calcium ions can react with anions (or groups of anions) from the activator [33], the initial setting time and the solubility of GGBS ions should be interrelated. Consequently, it is reasonable to assume that the amount of dissolved calcium ions from the dissolution of GGBS particles, and thereby the concentration of calcium ions in the mixing solution, is a function of the specific surface S of the slag.

Considering a chemical reaction that takes into account both a lower and a higher limit for an initial setting time, we can derive the following relationship between t and S:

$$t = \frac{1}{k}\ln\left(\frac{A-B}{S-B}\right) \tag{1}$$

where k is the kinetic coefficient of the chemical reaction and A and B are the constants describing the higher and lower limit of the specific surface area, respectively . By curve fitting the present results (see Fig. 4), it is found that $k = 4.7 \times 10^{-2}$ min^{-1}, $A = 7100$ m^2/g and $B = 3900$ m^2/g. This indicates that, for this specific chemical composition of the GGBS material, no initial setting time occurs for specific surface areas below 3900 m^2/g whereas for specific surface areas above approximately 7100 m^2/g, the initial setting time will occur almost instantaneous. It should be noted that the particle size, and thereby the specific surface area, is changed during the dissolution process. This effect is not taken into account in this relatively simple relationship.

4.4 Water content dependence

During the hydration process, GGBS particles are gradually dissolved, hydration products nucleate on the particle surfaces and particles are bound together in clusters. Subsequently, a network is formed throughout the material and the material changes from a viscous liquid, in which particles are dissolved, to an interconnected solid phase. In analogy with the hydration process of ordinary Portland cement [45], this point can be considered as a solid percolation

threshold at which the initial setting occurs. For alkali-activated cementitious materials it has previously been shown that a larger specific surface is more reactive and needs more hydration water [13]. This can most likely be explained by the water-to-binder ratio having an influence on the amount of hydration product that is needed for the formation of the percolating solid network in a similar way as previously has been described for cement [45]. In Ref [45] it was furthermore shown that for cement of higher water-to-binder ratios, larger amounts of the hydration product is needed for formulation of the percolating solid network directly related to the initial setting time.

By the replacement of the ***M***-material with larger particles, as in the ***H*** material, the effective water content is changed. For instance, the effective water concentration of the sample with 25 wt% replacement of ***M*** with ***H*** can be approximated by 0.5/0.75 = 0.667, where 0.5 is the water-to-binder ratio. Figs. 2 and 4 (closed squares) show that the increased initial water content has a relatively large effect on the initial setting time. In addition, it can be observed that the initial setting time cannot completely be explained by the increase in effective water content. Thus, the ***H*** fraction dependent increase of the initial setting time is not entirely due to the increased effective water content. Rather it has to be explained by the decrease in total specific surface.

5. CONCLUSIONS

The results from this study show that the initial setting time of GGBS, alkali-activated by water glass of various moduli, is dependent on the particle size of the GGBS material and the specific modulus of the water glass, which are both parameters that have an influence on the viscosity of the activated mixture.

- The pH may not be a decisive parameter for the initial setting time but just a consequence of the addition of sodium hydroxide, which, in turn, determines the modulus of the water glass and the dissolution of ions from the slag. The amounts of ions are important for the structure and strength development.
- The modulus of water glass has a strong influence on the hydration rate, i.e. the rate for building up the gelation network. This is probably due to its effect on the viscosity of the water glass, which is also dependent on the portion of free water in the mixture.
- The particle size determines the concentration of dissolved calcium ions necessary for the development of the hydration product, and the fraction of free water in the solution. The latter also affects the viscosity of the initial mixture.

Acknowledgement
Financial support from the Swedish research council FORMAS (project No 201-49) and the Climate KIC project Building Technologies Acceleration is gratefully acknowledged.

REFERENCES

1. Shi C, Krivenko PV, Roy D. Alkali-activated cement and concretes 2006: Taylor and Frances Group, London and New York.
2. Lecomte I, Henrist C, Liegeois M, Maseri F, Rulmont A, Cloots R. (micro)-structural comparison between geopolymers, alkali-activated slag cement and portland cement. J. Eur. Ceram. Soc. 2006;26(16):3789-3797.

3. Chen W, Brouwers HJH. The hydration of slag, part 1: Reaction models for alkali-activated slag. J. Mater. Sci. 2007;42(2):428-443.
4. Bai Y, Collier NC, Milestone NB, Yang CH. The potential for using slags activated with near neutral salts as immobilisation matrices for nuclear wastes containing reactive metals. J. Nucl. Mater. 2011;413(3):183-192.
5. Fu YW, Cai LC, Wu YG. Freeze-thaw cycle test and damage mechanics models of alkali-activated slag concrete. Constr. Build. Materi. 2011;25(7):3144-3148.
6. Cho JW, Ioku K, Goto S. Effect of Pb^{II} and Cr^{VI} ions on the hydration of slag alkaline cement and the immobilization of these heavy metal ions. Adv. Cem. Res. 1999;11(3):111-118.
7. Deja J. Immobilization of Cr^{6+}, Cd^{2+}, Zn^{2+} and Pb^{2+} in alkali-activated slag binders. Cem. Concr. Res. 2002;32(12):1971-1979.
8. Qian G, Sun DD, Tay JH. Characterization of mercury- and zinc-doped alkali-activated slag matrix - part I. Mercury. Cem. Concr. Res. 2003;33(8):1251-1256.
9. Qian GR, Sun DD, Tay JH. Characterization of mercury- and zinc-doped alkali-activated slag matrix - part II. Zinc. Cem. Concr. Res. 2003;33(8):1257-1262.
10. Rakhimova NR., Rakhimov RZ. A review on alkali-activated slag cements incorporated with supplementary materials. J. Sustain. Cem-based Mater. 2014;3(1):61-74.
11. Peter Domone, Illston J, eds. Construction materials - their nature and behaviour. 4th ed. 2010, Spon Press: London and New York.
12. Pacheco-Torgal F, Castro-Gomes J, Jalali S. Alkali-activated binders: A review - part 1. Historical background, terminology, reaction mechanisms and hydration products. Constr. Build. Mater. 2008;22(7):1305-1314.
13. Pacheco-Torgal F, Castro-Gomes J, Jalali S. Alkali-activated binders: A review. Part 2. About materials and binders manufacture. Constr. Build. Mater. 2008;22(7):1315-1322.
14. Roy D. Alkali-activated cements - opportunities and challenges. Cem. Concr. Res. 1999;29(2):249-254.
15. Yang K-H, Mun J-H, Sim J-I, Song J-K. Effect of water content on the properties of lightweight alkali-activated slag concrete. J. Mater. Civ. Eng. 2011;23(6):886-894.
16. Chang JJ. A study on the setting characteristics of sodium silicate-activated slag pastes. Cem. Concr. Res. 2003;33(7):1005-1011.
17. Cheng TW, Chiu JP. Fire-resistant geopolymer produced by granulated blast furnace slag. Miner. Eng. 2003;16(3):205-210.
18. Palacios M, Banfill PFG, Puertas F. Rheology and setting of alkali-activated slag pastes and mortars: Effect of organ admixture. ACI Mater. J. 2008;105(2):140-148.
19. Palacios M, Puertas F. Effectiveness of mixing time on hardened properties of waterglass-activated slag pastes and mortars. ACI Mater. J. 2011;108(1):73-78.
20. Yang K-H, Song J-K. Workability loss and compressive strength development of cementless mortars activated by combination of sodium silicate and sodium hydroxide. J. Mater. Civ. Eng. 2009;21(3):119-127.
21. Altan E, Erdogan ST. Alkali activation of a slag at ambient and elevated temperatures. Cem. Concr. Compos. 2012;34(2):131-139.
22. Fernandez-Jimenez A, Puertas F. The alkali-silica reaction in alkali-activated granulated slag mortars with reactive aggregate. Cem. Concr. Res. 2002;32(7):1019-1024.
23. Collins F, Sanjayan JG. Early age strength and workability of slag pastes activated by NaOH and Na_2CO_3. Cem. Concr. Res. 1998;28(5):655-664.
24. Shi CJ, Day RL. Some factors affecting early hydration of alkali-slag cements. Cem. Concr. Res. 1996;26(3):439-447.
25. Naceri A, Bouglada MS, Grosseau P. Mineral activator and physical characteristics of slag cement at anhydrous and hydrated states. World Acad. Sci. Eng. Tech. 2009;56:137-139.
26. Yang K-H, Sim J-I, Nam S-H. Enhancement of reactivity of calcium hydroxide-activated slag mortars by the addition of barium hydroxide. Constr. Build. Mater. 2010;24(3):241-251.
27. Burciaga-Diaz O., Magallanes-Rivera RX., Escalante-Garcia JI. Alkali-activated slag-metakaolin pastes: Strength, structural, and microstructural characterization. J. Sustain. Cem-based Mater. 2013;2(2):111-127.

28. Shi C, He F. On the state and roles of anion or anion group of activators during activation of slag. Proceeding of the 1st International conference on advances in chemically-activated materials, CAM'2010. 2010. China.
29. Ravikumar D, Neithalath N. Reaction kinetics in sodium silicate powder and liquid activated slag binders evaluated using isothermal calorimetry. Thermochim. Acta. 2012;546:32-43.
30. Personal communication with a product specialist at WWR International AB.
31. Ben Haha M, Lothenbach B, Le Saout G, Winnefeld F. Influence of slag chemistry on the hydration of alkali-activated blast-furnace slag - part I: Effect of MgO. Cem. Concr. Res. 2011;41(9):955-963.
32. Bernal SA, Nicolas RS, Myers RJ, de Gutierrez RM, Puertas F, van Deventer JSJ, Provis JL. Mgo content of slag controls phase evolution and structural changes induced by accelerated carbonation in alkali-activated binders. Cem. Concr. Res. 2014;57:33-43.
33. Brough AR, Atkinson A. Sodium silicate-based, alkali-activated slag mortars part i. Strength, hydration and microstructure. Cem. Concr. Res. 2002;32(6):865-879.
34. Krizan D, Zivanovic B. Effects of dosage and modulus of water glass on early hydration of alkali-slag cements. Cem. Concr. Res. 2002;32(8):1181-1188.
35. Zumdahl SS. Chemical principles 4th ed 2002.
36. Song SJ, Jennings HM. Pore solution chemistry of alkali-activated ground granulated blast-furnace slag. Cem. Concr. Res. 1999;29(2):159-170.
37. Greenberg SA, Chang TN. Investigation of colloidal hydrated calcium silicates .2. Solubility relationships in calcium oxide-silica-water system at 25 degrees. J. Phys. Chem. 1965;69(1):182-188.
38. Yang X, Zhu W, Yang Q. The viscosity properties of sodium silicate solutions. J. Solution Chem. 2008;37(1):73-83.
39. Nordstrom J, Nilsson E, Jarvol P, Nayeri M, Palmqvist A, Bergenholtz J, Matic A. Concentration- and Ph-dependence of highly alkaline sodium silicate solutions. J. Colloid Interface Sci. 2011;356(1):37-45.
40. Jansson H, Tang L. The initial setting time of ground granulated blastfurnace slag ggbs and its relation to the modulus of the alkali-activating solution. Proceeding of the XXII Nordic concrete research symposium. 2014. Reykjavik, Iceland
41. FernandezJimenez A, Puertas F. Alkali-activated slag cements: Kinetic studies. Cem. Concr. Res. 1997;27(3):359-368.
42. Bernal SA, Provis JL, Rose V, Mejia de Gutierrez R. Evolution of binder structure in sodium silicate-activated slag-metakaolin blends. Cem. Concr. Compos. 2011;33(1):46-54.
43. Criado M, Fernandez-Jimenez A, Palomo A, Sobrados I, Sanz J. Effect of the SiO_2/Na_2O ratio on the alkali activation of fly ash. Part II: ^{29}Si MAS-NMR survey. Micropor. Mesopor. Mater. 2008;109(1-3):525-534.
44. Beltram P. Rates of chemical reactions: Their measurement and mathematical expressions, in Fundamentals of chemistry 2009.
45 Zhang J, Weissinger EA, Peethamparan S, Scherer GW. Early hydration and setting of oil well cement. Cem. Concr. Res. 2010;40(7):1023-1033.

Pb^{2+} Adsorption by Calcium Silicate Hydrate Synthesized from Steel Slag

Shuping Wang
M.Eng., Ph.D.
Division of Building Technology, Chalmers University of Technology, SE- 412 96, Gothenburg
College of Material Science and Engineering, Chongqing University, CN-400045, Chongqing
E-Mail: shuping@chalmers.se

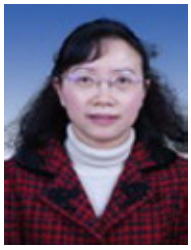

Xiaoqin Peng
Ph.D., Prof.
College of Material Science and Engineering, Chongqing University, CN-400045, Chongqing
E-Mail: pxq01@cqu.edu.cn

Mei Li
M. Eng.
College of Material Science and Engineering, Chongqing University, CN-400045, Chongqing
E-Mail: 674842676@qq.com

Luping Tang
Ph.D., Prof.
Division of Building Technology, Chalmers University of Technology, SE- 412 96, Gothenburg
E-Mail: tang.luping@chalmers.se

ABSTRACT

This study aims to investigate the adsorption properties of Pb^{2+} by calcium silicate hydrate synthesized from steel slag. The influence of various factors on the adsorption properties was investigated. The static desorption test was conducted to investigate the leaching of Pb^{2+}. The kinetic model and isotherm model of adsorption are then discussed. Results show that Pb^{2+} adsorption capacity of C-S-H depends on Ca/Si ratios. Kinetic adsorption data is in consistence with Lagergren pseudo-second-order model, and steady-state data fits to Langmuir isothermal model. Leaching result demonstrates that Pb^{2+} ions are stably adsorbed by C-S-H structures.

Key words: Pb^{2+} adsorption, calcium silicate hydrates, steel slag, adsorption model.

1. INTRODUCTION

Recently, solidification/stabilization technology (S/S) of cement-based material is widely studied on treating the heavy metal pollution and water treatment [1-5]. It is attributed to calcium silicate hydrate (C-S-H, C=CaO, S=SiO_2, H=H_2O), the main hydration product of cement paste. The main structures of C-S-H (Ca/Si molar ratio from 0.6 to 2) are disordered forms of 1.4 nm tobermorite and jennite, with a large specific surface area, high porosity and active sites such as hydroxyl groups [6,7]. Calcium silicate hydrates exhibit a large number of structural sites available for cation and anion binding [8]. Therefore, C-S-H structure plays an essential role in adsorption of heavy metals. The mechanism includes ion-exchange, adsorption and chemical trapping. Heavy metals such as Nd(III), Zn(II), Cd(II), Cr(IV) , U(IV) and Sr(II) adsorbed by C-S-H have been studied by many researchers [9-14]. The results show that the heavy metals are incorporated into the Ca-O sheets, absorbed in the interlayer of C-S-H, or ion-exchange with Ca^{2+} as the curing age increases.

Apart from cement hydration, C-S-H can also be obtained from waste slags, such as steel slag, which has a large amount of emission but low utilisation especially in China [15]. Wang et al. synthesized 11.3 Å tobermorite structures from steel slag by hydrothermal treatment [16]. Kuwahara and co-workers [17] reported that C-S-H prepared from the waste slag had good adsorption properties for removal of Cu^{2+}, phosphate ions and model protein diluted in water. Therefore, synthesized C-S-H is considered as a candidate for water purification on the heavy metals.

Lead (Pb), harmful to the health of human beings, is one of the main contaminations around the world; hence, how to treat it has become widely discussed. Xonotlite secondary particles were used to treat lead-bearing wastewater by Han, et al. [18], which indicated high Pb^{2+} removal. Investigations of Lee [19], Pierrard, Rimbault, and Aplincourt [20] suggested that Pb^{2+} fixed by C-S-H was affected by pH value of its pore solution. The main formation of Pb was $Pb_4SO_4(CO_3)_2(OH)_2$ and $3PbCO_3 \cdot 2Pb(OH)_2 \cdot H_2O$ at short time curing. The lead was adsorbed on the silica-rich surface to form C-Pb-S-H after long time cured together with acid attack. Pb^{2+} adsorbed by 1.1 nm tobermorite was also studied by Coleman, Trice, and Nicholson [21], indicating that the sorption conforms to the pseudo-second-order model and the uptake was up to 467 mg g^{-1} after 168-hour curing. However, the adsorption properties and mechanisms of lead on C-S-H are still poorly understood. In particular, there is seldom investigation on lead uptake in mild acidic medium.

This study explores the possibility of Pb^{2+} adsorption on calcium silicate hydrates synthesized from steel slag in mild acidic solutions. The influence of various factors, e.g. the properties and amount of C-S-H powder, adsorption time, Pb^{2+} concentrations, and pH values of the solution, on the adsorption properties are investigated. Furthermore, the kinetic and isotherm behaviours of adsorption by C-S-H are discussed.

2. EXPERIMENTAL

2.1 Materials

The main chemical compositions of steel slag (Shougang Group, Beijing) used in this study are listed in Table 1. It was obvious that the steel slag consisted of CaO, SiO_2, MgO, Al_2O_3, and Fe_2O_3, with Ca/Si molar ratio of 2.17. The specific surface area measured by Blaine Air

Permeability was 474 m^2 kg^{-1}. The main mineral phases in this steel slag were C_3S and C_2S according to XRD analysis. There is no doubt that the slag was available for synthesizing calcium silicate hydrate.

Table 1 – Main chemical composition of steel slag

Components	CaO	SiO_2	Fe_2O_3	Al_2O_3	MgO	P_2O_5
Content (%)	42.80	21.14	5.74	5.86	9.58	0.58

2.2 C-S-H synthesis

Calcium silicate hydrate powder was synthesized in an autoclave (Weihai Chemical Machinery Co. Ltd). Steel slag was mixed with lime (87.9% CaO) and quartz (99.09% SiO_2) at the Ca/Si molar ratio between 0.8 and 1.5. The mixture was cured at temperatures ranging from 150℃ to 185℃, for 7 hours, with the water to solid ratio (w/s, in mass) of 6, filtered and oven- dried at 80 ℃. The details of hydrothermal synthesis are in Table 2.

Table 2 – the hydrothermal synthesis of calcium silicate hydrates

index	Raw materials (%)			Ca/Si	w/s	Curing temperature (℃)	Curing time (h)
	Steel slag	quartz	lime				
A	70	20.00	10.00	1.2	6	150	7
B	70	20.00	10.00	1.2	6	185	7
C	70	14.19	15.81	1.5	6	150	7
D	80.28	19.72	0	1.5	6	185	7
E	70	27.96	2.04	0.8	6	185	7

2.3 Adsorption of Pb^{2+} by C-S-H

Pb^{2+} solutions were prepared by dissolving lead acetate (research grade, Jinshan Chemical Reagent Co., Ltd., Chengdu) in distilled water. 100mL solution was added in the beaker with a proper amount of C-S-H powder, adjusting the pH value of the solution to 2 to 7, stirring (100 rpm). These tests were all carried out at the room temperature. The concentration of Pb^{2+} after adsorption was measured, and influences of the powder amount, adsorption time, pH of solution, initial Pb^{2+} concentrations on C-S-H capacity were discussed. The removal ratio(R) and adsorption capacity (q) of Pb^{2+} by C-S-H were calculated as followed formulas:

$$R(\%) = {100\% \times (C_0 - C)}/{C_0} \quad (1)$$

$$q = {(C_0 - C) \times V}/{m_p} \quad (2)$$

Where C_0 is the initial concentration of Pb^{2+} (in mg L^{-1}); C indicates Pb^{2+} concentration after adsorption (in mg L^{-1}); V represents volume of solution (in L); m_p is the mass of hydrated calcium silicate powder (in g); and q is the amount of Pb^{2+} adsorbed by per unit C-S-H (in mg g^{-1})

2.4 Desorption test

To investigate the leaching of lead after having been adsorbed by C-S-H, static desorption measurement was carried out at room temperature. 1.5 gram powder with Pb^{2+} after equilibrium adsorbed was added into 100 ml distilled water or acetic acid solution (pH value of 5), respectively. After stirring (100 rpm) for 75 minutes, the solution was filtered and Pb2+ concentration of the solution was measured. The desorption ratio (ε) is calculated as following formula:

$$\varepsilon(\%) = \frac{C_1 V_1}{(C_0 - C)V} \times 100\% \tag{3}$$

C_0, C and V are described in the above section, where C_1 and V_1 represent the Pb^{2+} concentration and volume of the solution after desorption, respectively.

2.5 Product characterisation

XRD was applied to identify the crystalline phases of the synthesized C-S-H powders. The samples were detected by a Rigaku D/max-1200 X-ray powder diffraction apparatus (Cu Kα radiation), at a step size of 0.02° with scanning rate of 2° min^{-1}, and a scan range from 5° to 70° 2θ. SEM (scanning electron microscope Morphology, TESCAN VEGA II) with a voltage of 20KV and magnitude of 4~100,000 X was also employed for detecting the morphology of the hydrothermal products. FTIR spectroscopy (Nicolet5DXC) equipped with a KBr beam splitter was used for functional group analysis, with scanning wavenumber from 4000 to 400 cm^{-1}.

Pb^{2+} concentrations were measured via spectrometric atomic absorption apparatus (Hitachi Z-8000), at a wavelength of 283 nm, according to the standard of GB/T 9723-2007 (General rule for flame atomic absorption spectrometric analysis). The measurement was calibrated by measuring the absorbance at Pb concentrations of 0, 1, 2, 4, 6, 8, and 12 mg L^{-1}. Background was removed during analysis.

2.6 Adsorption models

Kinetic models

The Lagergren pseudo-first-order rate model and pseudo-second-order rate expression are used to study the adsorption kinetic model of Pb^{2+} by calcium silicate hydrates. These models describe adsorption of a solute by a solid surface, and adsorption processes in which the reaction rate is proportional to square [21-23].

The pseudo-first-order rate model can be expressed as following:

$$q^e = \frac{V(C_0 - C_e)}{m_p} \tag{4}$$

$$\log(q^e - q_t) = \log q^e - \frac{k_1}{2.303} t \tag{5}$$

Where q^e(in mg·g^{-1}) is the extent of sorption at equilibrium according to equation (2), C_e (in mg·L^{-1}) is the steady-state concentration of the metal ion in solution, q_t (in mg·g^{-1}) is the extent of adsorption at time t, and k_1(in min^{-1}) is the apparent pseudo-first-order rate constant of adsorption.

The expression of pseudo-second-order rate is:

$$\frac{t}{q_t} = \frac{1}{k_2 (q^e)^2} + \frac{1}{q^e} t \tag{6}$$

Where k_2 is the apparent pseudo-second-order rate constant of adsorption (in g mg^{-1} min^{-1}). If there is a linear plot of t/q_t against t, pseudo-second-order rate equation is satisfied.

Isothermal models

Adsorption isothermal equation reflects the relation between adsorptive capacity and the concentration of solution under a fixed temperature. There are mainly two models. One is Langmuir isotherm model reflecting the monolayer adsorption onto solid surfaces, and the other is Freundlich isothermal model which is also widely applied in liquid-solid adsorption system.

The linear form of the Langmuir isothermal model, used to illustrate uptake of metal ions from solution by a solid substance, can be described as follows [22, 23]:

$$\frac{C_e}{q^e} = \frac{1}{q_m b} + \frac{C_e}{q_m} \tag{7}$$

In equation (7) q_m is the maximum adsorptive capacity (in mg·g^{-1}) and b is the Langmuir constant (in L·mg^{-1}). Other parameters are described as above. q_m, and b is estimated from the intercept and the slop of the plot of C_e/n_s against C_e.

Freundlich isothermal model is described as:

$$\log q^e = \log K + \frac{1}{n} (\log C_e) \tag{8}$$

Where K is Freundlich constant and $1/n$ is constant as well. This model is based on the assumption that the enthalpy of sorption becomes less negative [22].

3. ADSORPTION MODELS

3.1 Microstructures of synthesized C-S-H

XRD analysis

The XRD patterns of the synthetic samples are shown in Figure 1. Poorly crystalline C-S-H formed in all the samples due to the only appearance of diffraction peaks with the d-spacing of 0.302 nm (2θ 29º), 0.182 nm (2θ 18º) and 0.280 nm (2θ 32º) [7]. However, the final hydration phases were influenced by the hydrothermal curing process, such as the addition of lime, and the different Ca/Si molar ratios. Powder A and B consisted of C-S-H, and semi- tobermorite (d-spacing of 3.08 Å, 2.98 Å and 1.84Å) [16]. It is also found that SiO_2 was still present in Powder

A because of the appearance of intensive diffraction peak at 3.34 Å. As the Ca/Si ratio increased to 1.5 in Powder C, the dominant phase was poorly crystallized C-S-H. Besides, a zeolite- like gel was also generated due to the appearance of the peak at 3.17 Å. This phase is beneficial to the heavy metal incorporation. The main phase of Powder E was disordered C-S-H. In additional quartz was not completely consumed.

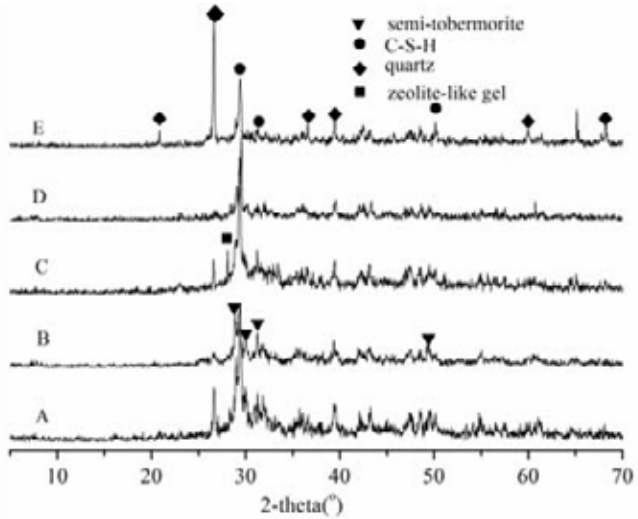

Figure 1 – XRD patterns of C-S-H samples made from steel slag by weight at the water/solid ratio of 6 and curing for 7 hours. The details for hydrothermal synthesis are shown in Table 2.

SEM analysis

The morphology of the synthetic C-S-H samples was investigated with SEM microscope (Figure 2). The powder particles showed non-crystallized structures, and were an aggregation of micro-scale morphology, which was 1 μm. It can be seen that the curing method, especially the Ca/Si molar ratio, affects the final morphology of the product . In sample A, which was prepared at 150 ℃ for 7 hours at the Ca/Si ratio of 1.2, foil or sheet-like structure appeared. When the Ca/Si ratio increased to 1.5, in sample C, C-S-H made up of fibril shaped grains with a loose reticular structure. It presented a porous surface, which is a so called as zeolite-like structure. In powder D, however, it exhibited a more compacted morphology with a lack of pronounced pores on the surface, which was attributed to the lack of lime addition.

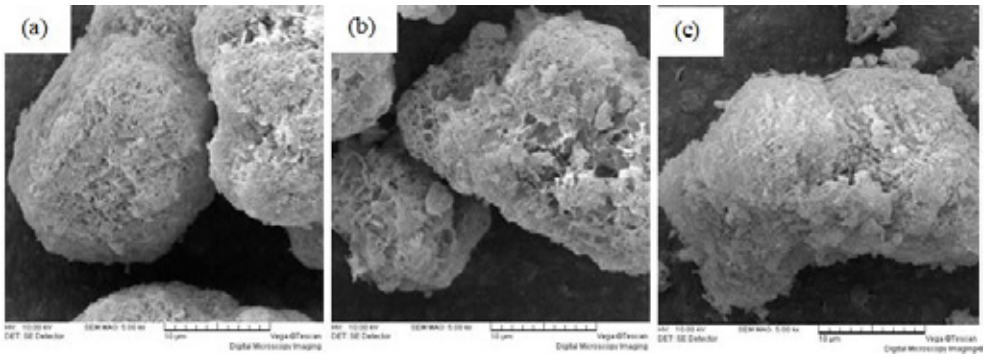

Figure 2 – SEM Photographs of the synthetic C-S-H:
(a) powder A synthesized from the mixture of 70wt% steel slag, 20wt% quartz and 10wt% lime with 1.2 Ca/Si molar ratio at 150 ℃ for 7 hours;
(b) Powder C synthesized from the mixture of 70wt% steel slag, 14.19wt% and 15.81wt% lime, with the Ca/Si molar ratio of 1.5 at 150 ℃ for 7h; and
(c) Powder D is corresponded to the product from 80.28wt% steel slag and 19.72wt% quartz without lime addition, the Ca/Si molar ratio of 1.5 at 185 ℃ for 7 hours

3.2 Pb^{2+} adsorption properties on C-S-H

The adsorption of Pb^{2+} by different C-S-H powders

C-S-H powders produced from different hydrothermal curing conditions were used to adsorb the Pb^{2+} with the concentration of 200 mg L^{-1}, and the results are shown in Figure 3. The adsorption properties were influenced by the synthesis process, generally on the Ca/Si molar ratio and the content of the lime. The sample C which was synthesized at 150 ℃ for 7 hours with the molar ratio of 1.5 presented the highest removal efficiency (about 99.67 %), and the adsorption capacity of Pb^{2+} was up to 19.53 mg g^{-1}. However, there were no satisfying results of Pb^{2+} adsorption by other types of powder, as the removal and adsorption capacity were lower than 90% and 18 mg g^{-1} respectively. The higher incorporation of Pb^{2+} in Powder C than other samples is attributed to its porous surface of the particles. In this case, Powder C was used for thermodynamic analysis on the subsequent adsorption study.

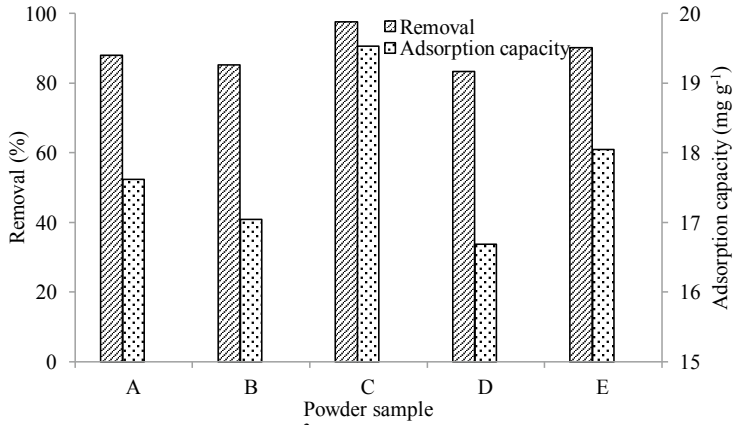

Figure 3 – Adsorption of Pb^{2+} by different kinds of C-S-H powders, synthesis of powder is in Table 2

Effect of C-S-H amount on Pb^{2+} adsorption

Different amount of calcium silicate hydrate powder were mixed with 100 mL Pb^{2+} solution (200 mg L^{-1}), adjusting the initial pH value of the mixture to 5. Adsorption time of 1 hour was applied. The result of adsorption is shown in Figure 4.

It can be seen that the removal efficiency increased rapidly from 31% to 96%, corresponding to the mass of C-S-H powder from 5 g L^{-1} to 15 g L^{-1}, followed by the stable adsorption efficiency. When 20 g L^{-1} of C-S-H powder was used, the removal of Pb^{2+} was up to 99%, with the residual concentration of Pb^{2+} solution 0.96 mg L^{-1}. Additionally, the adsorption capacity of Pb^{2+} by C-S-H was first increased and then declined as the amount of the powder increased. The maximum of adsorption capacity was 14.46 mg g^{-1} with the amount of 10 g L^{-1} powder, demonstrating that excessive amount of powder cannot be completely utilized. Therefore, in the following adsorption experiments, 15 g L^{-1} C-S-H powder is used.

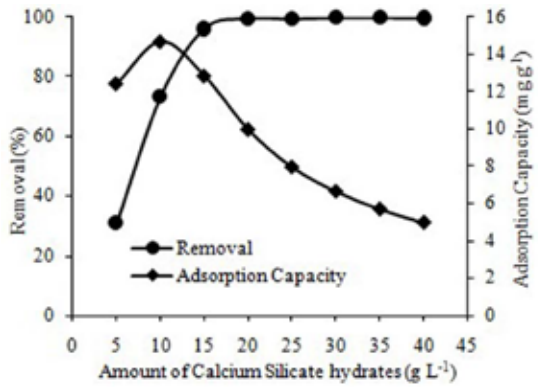

Figure 4 – Pb^{2+} removal at different amount of C-S-H powder

Effect of pH on Pb^{2+} adsorption

1.5 g calcium silicate hydration powder was mixed with 100 mL Pb^{2+} solution (Pb^{2+} concentration 200 mg L^{-1}). The initial pH values of the solution ranged from 2 to 7, with stirring

time of 1 hour (Figure 5). The removal efficiency and adsorption capacity of Pb^{2+} by C-S-H is influenced obviously by pH. At pH value of 2, the removal efficiency and adsorption capacity were only 11% and 1.52 mg g^{-1}, respectively. With pH increasing to 5, both the removal and adsorption capacity soared up to 96% and 12.73 mg g^{-1}, respectively. The data gradually increased when the pH value varied between 5 and 7. It is apparent that Pb^{2+} can be effectively adsorbed on C-S-H via weak acidic solution, since there are negative charges on the surface of C-S-H particles when pH of the solution is close to 7 [24]. On the other hand, the structure of C-S-H was damaged by strong acid solution, resulting in the poor adsorption.

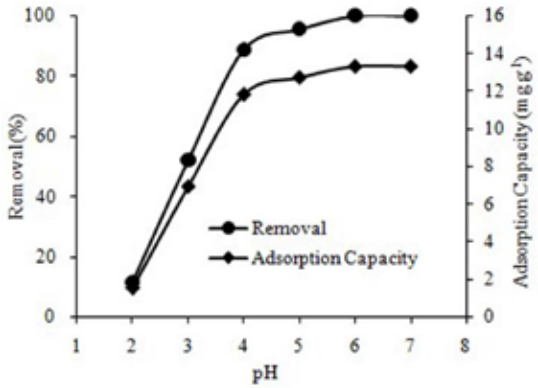

Figure 5 – Pb^{2+} adsorption in the solution of different pH values

Influence of stirring time on Pb^{2+} adsorption

Stirring time is another key factor on Pb^{2+} adsorption and reflects its equilibrium status. In this section, the adsorption properties of the duration from 30 minutes to 180 minutes were investigated (Figure 6). The curves indicated that the powder had an excellent adsorption property on Pb^{2+} even for only 30-minute reaction. The removal efficiency and the adsorption capacity were approximate 96% and 12.78 mg g^{-1}, respectively. Afterward, the removal efficiency increased to 99.4% and adsorption capacity of 13.25 mg g^{-1} at 75 minutes' adsorption. With stirring time extended, the values gradually improved, and residual Pb^{2+} concentration of the solution declined to 0.44 mg L^{-1} at 180 min, far below the emission standard of 1.0 mg L^{-1} (GB 8978-1988). According to Figure 6, the balance of adsorption was achieved after 75-minute adsorption.

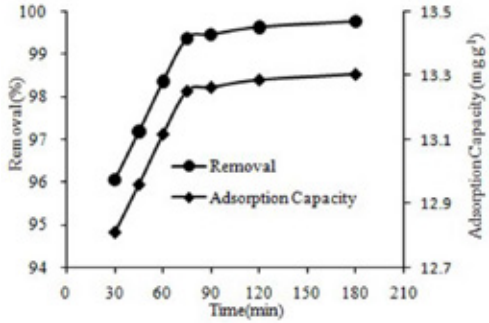

Figure 6 – Pb^{2+} adsorption properties at different stirring time

Influence of initial concentration of Pb^{2+} on adsorption

Herein, the results about adsorption of Pb^{2+} concentrations between 50 mg L^{-1} and 400 mg L^{-1} were discussed (Figure 7). With the increase of Pb^{2+} concentration from 50 mg L^{-1} to 400 mg L^{-1}, the adsorption capacity and Pb^{2+} concentration rapidly went up to 24.46 mg g^{-1} from 3.35 mg g^{-1}, which was attributed to the increase of contact sites between the calcium silicate hydrate powder and Pb^{2+}. On the contrary, the curve of removal appeared different tendency. It was stable at around 99% as the concentration ranged from 50 mg $L^{-1}$to 200 mg L^{-1}, and the maxium value was 99.4% at the Pb^{2+} concentration of 200 mg L^{-1}. The removal efficiency declined to 91.7% corresponding to the Pb^{2+} concentration of 400 mg L^{-1}.

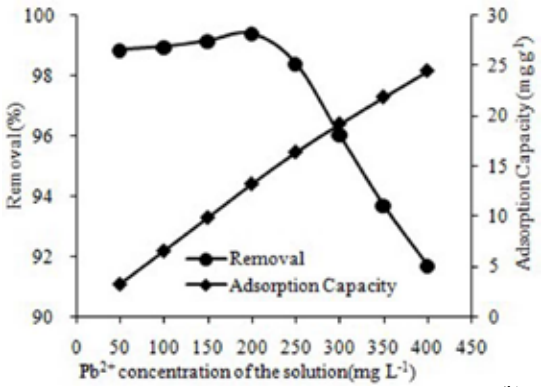

Figure 7 – adsorption properties with various Pb^{2+} concentration

3.3 Desorption of Pb^{2+} on C-S-H

Desorption tests were carried out both under distilled water and acidic solution, corresponding to the pH of 7.0 and 5.0. Results showed that the Pb^{2+} concentration was 0.16 mg L^{-1} after leaching experiment, indicating that the desorption ratio in water was as low as 0.08% according to equation (3). When acidic solution with pH of 5.0 was adopted, the leaching concentration of Pb^{2+} increased to 0.64 mL g^{-1}. It means that the desorption rate was 0.3%. The results demonstrate that Pb^{2+} can strongly adsorbed by C-S-H powder and leaching ratio in neutral solution is quite low, which might attribute to the combination between Pb^{2+} and functional groups.

4. ADSORPTION MODELS

4.1 Kinetic models

As mentioned previously, adsorption kinetic is analyzed by applying Lagergren pseudo-first-order model (equation (5)), and pseudo-second-order model (equation (6)). According to the data in Figure 6, the parameters of the two kinetic models are obtained (Figure 8, Table 3). The results show that higher correlation of the pseudo-second-order kinetic model (R^2 value of 1) than pseudo-first-order kinetic model (R^2 value of 0.96), demonstrating that the former affords a more appropriate description of the sorption process. Thus, the equilibrium adsorption q^e and constant rate k_2 are 13.09 mg g^{-1} and 7.82×10^{-2} g mg^{-1} min^{-1}, respectively. The kinetic results of

adsorption of metal cations by C-S-H powder is likely to reveal that the reaction is controlled by a number of transport and interaction process.

Table 3 – Statistical and kinetic datas of Pb^{2+} sorption on C-S-H

Lagergren (pseudo-first-order)			Lagergren(pseudo-second-order)		
q^e /(mg g^{-1})	$k_1 \times 10^{-2}$ /(min^{-1})	R^2	q^e /(mg g^{-1})	$k_2 \times 10^{-2}$ /(g mg^{-1} min^{-1})	R^2
13.30	6.86	0.96	13.09	7.82	1

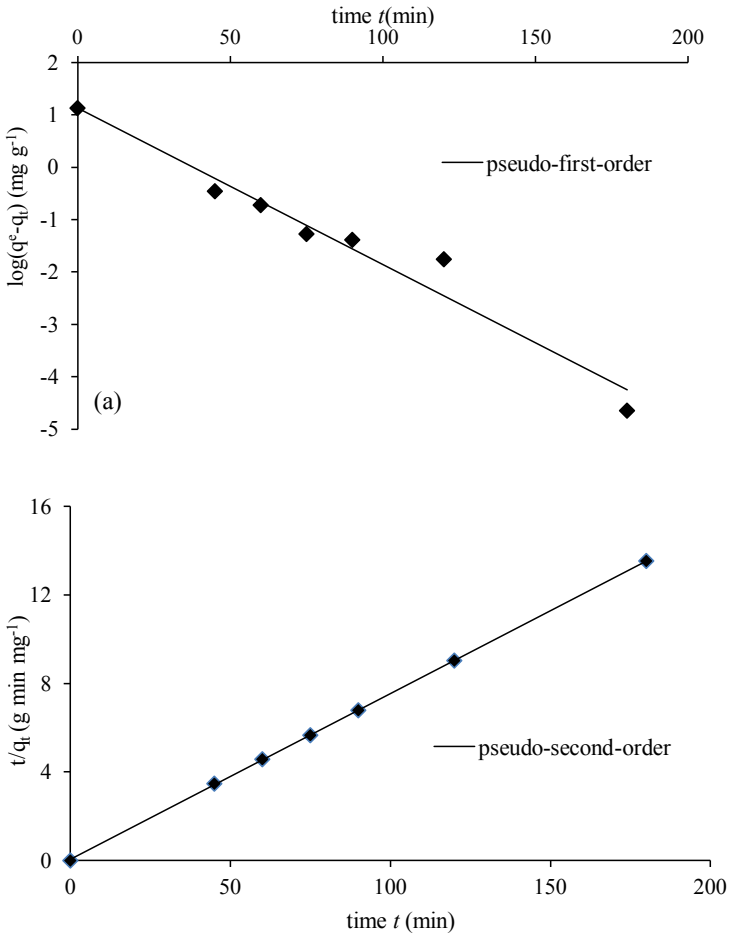

Figure 8 – kinetic model fitted to experimental data for the uptake of Pb^{2+} (a) pseudo-first-order model, and (b) pseudo-second-order model

Thus, adsorption rate is an important indicator to reflect the interaction between adsorbent and adsorbate. Generally, the adsorption processes include three stages [25], which are external-particle diffusion stage, intra-particle diffusion stage and adsorption-reaction stage. Weber-Morris equation (equation (9)) was used to describe the diffusion and transfer procedure of Pb^{2+} on C-S-H particle surface[26, 27]:

$$n_t^s = k_{id} t^{\frac{1}{2}} + b \quad (9)$$

Where b represents intercept, and k_{id} is intra-particle diffusion constant (in mg g^{-1} $min^{-1/2}$). In accordance with Figure 6, the adsorption rate tends to be constant after 75 minutes. By fitting the experiment data depending on the equation above, the correlation coefficiency R^2 is 0.92, an indication of linear relationship. As a result, it can be considered that before 75 minutes the adsorptive process is controlled by external-particle diffusion stage, followed by intra-particle procedure [28]. The value of k_{id} is 0.016 mg g^{-1} $min^{-1/2}$, and b of 13.10.

4.2 Isothermal models

In order to discribe the adsorption properties on the the surface of the powder, adsorption isothermal is studied. The adsorption isothermal curve obtained from Figure 7 is shown in Figure 9, which means the adsorption capacity of C-S-H on different Pb^{2+} equilibrium concentration. It can be inferred form equation (7) and (8) that the data are well correlated with the Langmuir isothermal model with R^2 of 0.99. While the Freundlich model is less appropriate for its R^2 of only 0.77 (Table 4). Thus, the adsorption conforms to monolayer adsorption and there are many active sites on the surface of C-S-H particles.

Table 4 – Langmuir and Freundlich isothermal parameters for the absorption of Pb^{2+} on C-S-H

Langmuir			Freundlich		
q_m /(mg·g^{-1})	b /(L·mg^{-1})	R^2	K /(mg·g^{-1})	n	R^2
25.71	0.37	0.99	7.38	2.59	0.77

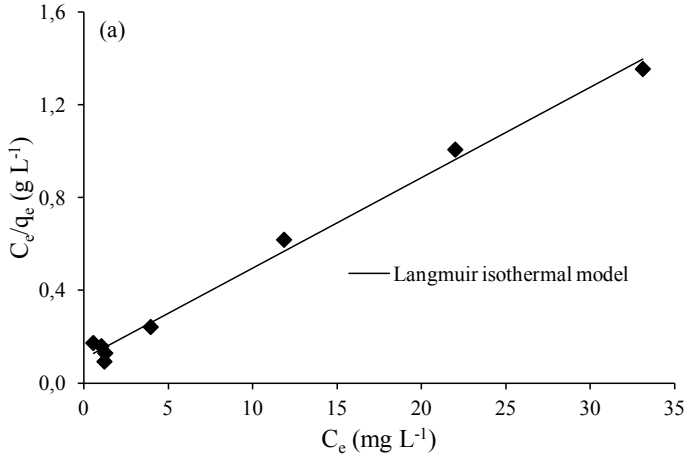

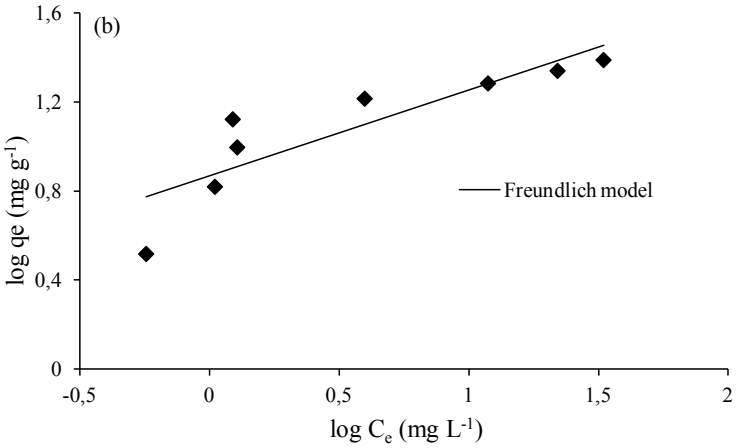

Figure 9 – Isothermal model fitted to experimental data for the uptake of Pb^{2+} (a) Langmuir isothermal model, and (b) Freundlich isothermal model

4.3 Microstructure analysis

FTIR was applied to study the structure variation of C-S-H powder before and after adsorption (Figure 10). In both samples, CO_3^{2-} asymmetric stretching bands due to contamination with CO_2 during samples preparation and drying were detected at 1432 cm^{-1} and 873cm^{-1}. The bending vibration band of molecular H_2O appeared at 1632 cm^{-1}, while the stretching vibration of O-H groups or hydroxyls appeared in the 3433-3440 cm^{-1} region. The most intensive vibration of silicate appeared as a band at the range of 900-1100 cm^{-1} which was attributed to stretching vibration of $[SiO_4]^{4-}$ tetrahedral. The vibration band in C-S-H was at 982 cm^{-1}, however, it shifted to 1075cm^{-1} after adsorbing Pb^{2+}, demonstrating that the polymerisation of silicate chain varied. In addition, the bands corresponding to δ-Si-OH stretching vibration appeared at 1280 cm^{-1} and 756 cm^{-1} in C-S-H, but disappeared after adsorbing Pb^{2+}, suggesting that coordination reaction between Hydroxyl functional group and Pb^{2+} took place as following way:

$$(Si\text{-}OH)+2H_2O+Pb^{2+}=Si\text{-}Pb(OH)_3+2H^+$$

This reaction agrees with the adsorption of Cu^{2+} by asbestos tailings in [29]. It indicates that the presence of active sites in C-S-H structures can cooperate with Pb^{2+} in a relative stable state, which is demonstrated by the desorption results.

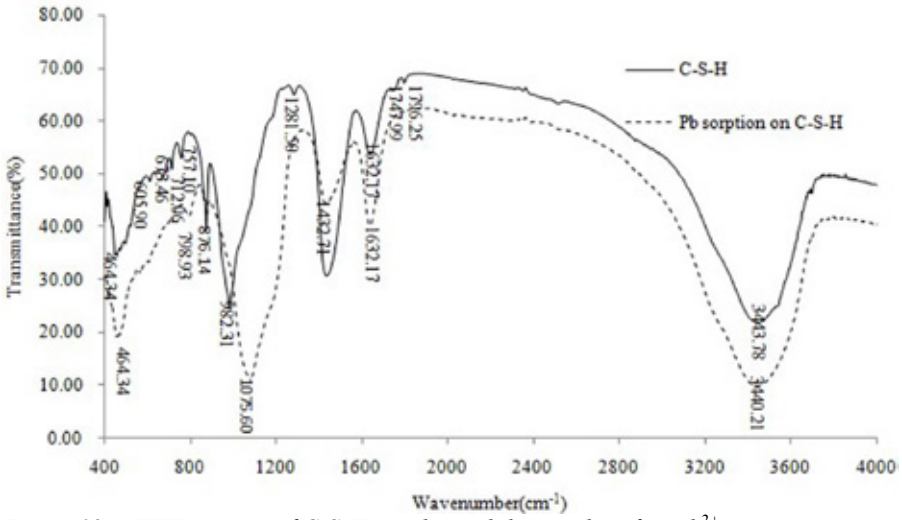

Figure 10 – FTIR spectra of C-S-H powder and the powder after Pb^{2+} sorption

5. CONCLUSION

This study shows that the calcium silicate hydrate synthesized from steel slag is a potential Pb^{2+} adsorbent. The adsorption depends on the Ca/Si molar ratio and lime addition which further affect on the surface properties of powder particles. The most efficient adsorption of the C-S-H has a Ca/Si ratio of 1.5. Pb^{2+} can be effectively removed by this C-S-H powder at the pH value of the solution between 5 and 7. The equilibrium adsorption occurs at 75 minutes when 15 g L^{-1} C-S-H is mixed with 200 mg L^{-1} Pb^{2+} solution. The removal of Pb^{2+} and adsorption capacity is 99.4% and 13.25 mg g^{-1}, respectively. The concentration of Pb^{2+} in the solution after adsorption for more than 120 minutes is lower than 0.5 mg L^{-1}. The low leaching ratio from desorption result indicates that Pb^{2+} can be stably combined by C-S-H.

Kinetic sorption data were in agreement with the Lagergren pseudo-second-order with the equilibrium adsorption of 13.09 mg g^{-1}. In terms of the sorption isotherm, it can be described by the Langmuir adsorption isotherm, the equilibrium adsorption capacity of which is 20.41 mg g^{-1}. The adsorption is controlled by external-particle diffusion stage before equilibrium state, followed by intra-particle diffusion procedure.

ACKNOWLEGEMENT

This work was financed by NSFC (National Natural Science Foundation of China, 50972171) and Graduates Innovation and the Equipmental Administration Faculty of Chongqing University. The Authors also appreciate the support of Chinese Scholarship Council.

REFERENCES

1. Chiang, R.-K. "Calcium-based sorbents for flue gas desulfurization". Case Western Reserve University; 1995.
2. Lai, Y.-L., Thirumavalavan, M.,Lee, J.-F., "Effective adsorption of heavy metal ions (Cu^{2+}, Pb^{2+}, Zn^{2+}) from aqueous solution by immobilization of adsorbents on Ca-alginate beads". *Toxicological & Environmental Chemistry*.Vol. 92,No. 4, 2010, pp. 697-705.
3. Shrivastava, O.P.,Shrivastava, R., "Sr^{2+} uptake and leachability study on cured aluminum-substituted tobermorite–OPC admixtures". *Cement and Concrete Research*.Vol. 31,No. 9, 2001, pp. 1251-1255.
4. Song, Y.L., Wang, Y.P., Song, P.P., et al., "Nonequilibrium thermodynamics study of nuclide migration behavior in the cement based radioactive waste forms". *Journal of Henan University (Natural Science)*.Vol. 36,No. 3, 2006, pp. 21-24.(In Chinese).
5. Zhang, Y.M., Li, X.D.,Sun, W., "Leaching of Copper Wastes Stabilized by Cementitious Material". *Journal of Chinese Ceramic Society* Vol. 30,No. 4, 2002, pp. 536-539.
6. Mehta, P.K.,Monteiro, P.J.K. "Concrete microstructure, properties and materials ". third ed. New York: McGraw-Hill; 2006.
7. Taylor, H.F.W. "Cement Chemistry". London: Thomas Telford; 1997.
8. Chen, J.J. "The nanostructure of calcium silicate hydrate". Northwestern University; 2003.
9. Lan, J.K., Hu, Q.J.,Wang, Y.X., "Adsorption of chromate by calcium silicate hydrate". *Journal of Guilin University of Technology*.Vol. 26,No. 2, 2006, pp. 263-267. (In Chinese).
10. Mandaliev, P., Dähn, R., Tits, J., et al., "EXAFS study of Nd(III) uptake by amorphous calcium silicate hydrates (C–S–H)". *Journal of Colloid and Interface Science*.Vol. 342,No. 1, 2010, pp. 1-7.
11. Pomiès, M.-P., Lequeux, N.,Boch, P., "Speciation of cadmium in cement: Part I. Cd2+ uptake by C-S-H". *Cement and Concrete Research*.Vol. 31,No. 4, 2001, pp. 563-569.
12. Shrivastava, O.P.,Verma, T., "Sr2+ Sorption and leach rate studies on synthetic calcium silicate hydroxy hydrate". *Advanced Cement Based Materials*.Vol. 2,No. 3, 1995, pp. 119-124.
13. Stumm, A., Garbev, K., Beuchle, G., et al., "Incorporation of zinc into calcium silicate hydrates, Part I: formation of C-S-H(I) with C/S=2/3 and its isochemical counterpart gyrolite". *Cement and Concrete Research*.Vol. 35,No. (9), 2005, pp. 1665-1675.
14. Macé, N., Wieland, E., Dähn, R., et al., "EXAFS investigation on U(VI) immobilization in hardened cement paste: influence of experimental conditions on speciation". *Radiochimica Acta*.Vol. 101,No. 6, 2013, pp. 379-389.
15. Li, C.H., "Study on the development and prospect of recycling technology of steel slag in China". *Wisco Technology*.Vol. 38,No. 4, 2010, pp. 51-54. (In Chinese).
16. Wang, S., Peng, X., Tang, L., et al., "Influence of inorganic admixtures on the 11 Å-tobermorite formation prepared from steel slags: XRD and FTIR analysis". *Construction and Building Materials*.Vol. 60, 2014, pp. 42-47.
17. Kuwahara, Y., Tamagawa, S., Fujitani, T., et al., "A novel conversion process for waste slag: synthesis of calcium silicate hydrate from blast furnace slag and its application as a versatile adsorbent for water purification". *Journal of Materials Chemistry A*.Vol. 1,No. 24, 2013, pp. 7199-7210.
18. Han, J.H., Ni, W.,Yu, Y.Z., "Research on treatment of lead-bearing wastewater by xonotlite secondary particles". *Techniques and Equipment for Environmental Pollution Control*.Vol. 7,No. 1, 2006, pp. 22-25.
19. Lee, D., "Formation of leadhillite and calcium lead silicate hydrate (C–Pb–S–H) in the solidification/stabilization of lead contaminants". *Chemosphere*.Vol. 66,No. 9, 2007, pp. 1727-1733.

20. Pierrard, J.-C., Rimbault, J.,Aplincourt, M., "Experimental study and modelling of lead solubility as a function of pH in mixtures of ground waters and cement waters". *Water Research*.Vol. 36,No. 4, 2002, pp. 879-890.
21. Coleman, N.J., Trice, C.J.,Nicholson, J.W., "11 Å tobermorite from cement bypass dust and waste container glass: A feasibility study". *International Journal of Mineral Processing*.Vol. 93,No. 1, 2009, pp. 73-78.
22. Coleman, N.J., Brassington, D.S., Raza, A., et al., "Sorption of Co^{2+} and Sr^{2+} by waste-derived 11 Å tobermorite". *Waste Management*.Vol. 26,No. 3, 2006, pp. 260-267.
23. Liu, S.Y., Ma, S.J., Ye, Z.X., et al., "Absorption kinetics of Pb^{2+} on steel slag". *Environmental Protection of Chemical Industry*.Vol. 27,No. 3, 2007, pp. 214-217.
24. Mandaliev, P., Wieland, E., Dähn, R., et al., "Mechanisms of Nd(III) uptake by 11Å tobermorite and xonotlite". *Applied Geochemistry*.Vol. 25,No. 6, 2010, pp. 763-777.
25. Zhao, X.G., Liu, Z.N.,Wang, G.R., "Preparation of coal fly ash based forming adsorbent and its adsorptive properties for methylene blue". *Journal of Chinese Ceramic Society*.Vol. 37,No. 10, 2009, pp. 1683-1688.
26. Bulut, Y.,Aydın, H., "A kinetics and thermodynamics study of methylene blue adsorption on wheat shells". *Desalination*.Vol. 194,No. 1–3, 2006, pp. 259-267.
27. Wang, S., Xie, L.,Zhou, Q., "Adsorption properties and kinetics of chromium from aqueous solution by steel slag". *China Water & Wastewater*.Vol. 25,No. 3, 2009, pp. 54-57.
28. Zhang, Q.F., Hu, X.F., Jia, X.N., et al., "Study of diffusion equation for describing the adsorbing process of Cr (IV) by peanut shell". *Chemistry and Bioengineering* Vol. 28,No. 2, 2011, pp. 83-85.
29. Zheng, S.L., Zheng, L.M.,Tan, Z.H., "Adsorption of copper ion onto acid leaching residue of asbestos tailings". *Journal of Chinese Ceramic Society*.Vol. 37,No. 10, 2009, pp. 1744-1749.

Research Council and Editorial Board for Nordic Concrete Research

Dr. Dirch H. Bager, Chairman of the Research Council & Editor of Nordic Concrete Research

Danish Concrete Association

Dr. Dirch H. Bager
Lavendelparken 5
DK - 9310 Vodskov
Tel: +45 9829 2412
Mobile: +45 2049 7324
E-mail: dirch.bager@bbnpost.dk

Finnish Concrete Association

Mr. Juha Valjus
Concrete Association of Finland
Unioninkatu 14 PL 381
FI - 00131 Helsinki
Tel: +358 41 533 6020
Mobile: +358
E-mail: juha.valjus@betoniyhdistys.fi

Icelandic Concrete Association

Dr. Jón E. Wallevik
Innovation Center Iceland
IS - 112 Keldnaholti
Tel: +354 522 9362
Mobile: +354
Fax: +354 522 9111
E-mail: jon.w@nmi.is

Prof. Dr. Olafur H. Wallevik
Innovation Center Iceland
IS - 112 Keldnaholti
Tel: +354 522 9000
Mobile: +354
E-mail: wallevik@ru.is

Norwegian Concrete Association

Dr. Terje F. Rønning
Heidelberg Cement NE / Cement
Product development & Implementation
P.O.Box 38
N - 3991 Brevik
Tel.: +47 3557 2347
Mobile: +47 9157 6046
E-mail: terje.ronning@norcem.no

Prof. Dr. Mette R. Geiker
Division of Concrete Structures
Department of Civil Engineering
N - 7034 Trondheim
Tel: +47 7359 4529
Mobile: +47
E-mail: mette.geiker@ntnu.no

Swedish Concrete Association

Adjunct. Prof.,Tekn.Dr, Mikael Hallgren
Tyréns AB
Peter Myndes Backe 16
SE - 118 86 Stockholm
Tel: +46 104 522 351
Mobile: +46 70 661 05 33
E-mail: Mikael.Hallgren@tyrens.se

Tekn. Dr. Peter Utgenannt
CBI Swedish Cement and Concrete Research Institute
P.O. Box 857
SE - 501 15 Borås
Tel: +46 105 166 870
Mobile:+46 706 452 008
E-mail: peter.utgenannt@cbi.se

2015-06-20

Active reviewers for Nordic Concrete Research as per June 2015

DENMARK	Dr.	Dirch H. Bager
	Dr.	Mette Glavind
	Prof., Dr.	Per Goltermann
	Mr.	Oscar Klinghoffer
	Prof., Dr.	John Forbes Olesen
	Mr	Claus Pade
	Prof., Dr.	Eigil V. Sørensen
	Prof., Dr.	Jens Peder Ulfkjær
FINLAND	Dr.	Klaus Juvas
	Dr.	Matti V. Leskala
	Prof., Dr.	Jussi Mattila
	Dr.	Tarja Merikallio
	Dr.	Jouni Punkki
	Mr.	Juha Valjus
ICELAND	Mr.	Einar Einarsson
	Mr.	Haukur J. Eiriksson
	Dr.	Gisli Gudmundsson
	Mr.	Karsten Iversen
	Mr.	Torfi G. Sigurdsson
	Mr.	Sveinbjörn Sveinbjörnsson
	Dr.	Jon E. Wallevik
	Prof., Dr.	Òlafur H. Wallevik
	Prof., Dr.	Børge J. Wigum
NORWAY	Dr.	Helge Brå
	Ms.	Danielle Bosnjak
	Prof. Dr.	Mette Rica Geiker
	Mr.	Anton Gjørven
	Mr.	Steinar Helland
	Dr.	Bernt Jacobsen
	Prof., Dr.	Terje Kanstad
	Dr.	Terje F. Rønning
	Mr.	Tor Kristian Sandaker
	Mr.	Sverre Smeplass
	Mr.	Hans Stemland
SWEDEN	Prof., Dr.	Anders Ansell
	Dr.	Thomas Blanksvärd
	Prof.	Lennart Elfgren
	Prof., Dr.	Mats Emborg
	Prof., Dr.	Kent Gylltoft
	Prof., Dr.	Mikael Hallgren
	Prof., Dr.	Jan-Erik Jonasson
	Prof., Dr.	Björn Lagerblad
	Prof., Dr.	Karin Lundgren
	Prof., Dr.	Tang Luping
	Prof., Dr.	Per-Erik Petersson
	Prof., Dr.	Johan Silfwerbrand
	Dr.	Peter Utgenannt